On the Thermal Stability of θ′ Precipitates in Al-Cu-Mn-Zr alloys

A Dissertation Presented for the

Doctor of Philosophy

Degree

The University of Tennessee, Knoxville

Patrick Taylor Shower

August 2019

Dedication

Dedicated to the pursuit of an RCP 4.5 emissions trajectory, and all the people and animals that make this a world worth protecting.

Acknowledgments

I want to thank some of the many people that have supported these efforts throughout my time in graduate school. Amit Shyam has been an amazing advisor, keeping me on course and always helping me find the way forward when things didn't go as planned. Jamie Morris has been a great committee member, but has also gone above and beyond that role. He has truly stepped up to provide mentorship, even from my earliest days in the program, before I had a committee or any coauthors and he had nothing to gain from it. Balasubramaniam Radhakrishnan and Dongwon Shin also have also given large amounts of their time to help me navigate my way from an experimental background to a largely computational dissertation. Without their guidance on what computational modeling tools can (and can't) do, I would have been completely lost. I'd like to thank Jonathan Poplawsky for training me on the Atom Probe and providing some of the most interesting figures in my dissertation. Similarly I'd like to thank the lead metallographer Tom Geer for enabling me to capture crisp, clear SEM images of the Al-Cu microstructure that form the backbone of my current understanding. Outside of work, my wife Ariel has managed to keep me sane, cool, and collected through thick and thin, and I could never thank her enough.

I am also grateful for the resources that made this work possible. The NDSEG fellowship program allowed me time and liberty to find this project. I owe a great deal to the creators of the Multiphysics Object Oriented Simulation Environment at Idaho National Lab, and all the users how have volunteered their time and patience to explain how to use it. And of course no amount of equations or code would have done me any good without the computational resources at the Oak Ridge Leadership Computing Facility and the National Energy Research Scientific Computing Center, along with the staff that helped me through endless troubleshooting.

Abstract

Al-Cu-Mn-Zr (*ACMZ*) alloys demonstrate vastly improved mechanical properties at temperatures between 250 °C and 350 °C compared to conventional θ′-strengthened Al alloys. The improved high temperature mechanical properties of Al-Cu-Mn-Zr are due to the thermal stability of strengthening θ′ precipitates against transformation to the detrimental θ phase. This is illustrated by a study of the high-temperature compression response of an Al-Cu-Mn-Zr alloy that retains θ′ precipitates at elevated temperatures and a conventional alloy that does not. It is shown that the divergence in microstructure leads to a divergence in deformation mechanisms.

The thermal stability of strengthening θ′ particles is due to their coarsening resistance. This is because the onset of θ′ to θ transformation is controlled by the morphology of θ′, as determined by a combination of thermodynamic analysis, experimental observations, and phase field modeling. The coarsening resistance of θ′ particles can be achieved through a reduction in the thermodynamic driving force for coarsening, or the introduction of a kinetic rate-limiting step in the coarsening process. This is shown by a parametric phase field study.

The most effective means of controlling the thermodynamics and kinetics of θ′ evolution is a combination of interfacial energy reduction and solute drag caused by the segregation of slow-diffusing alloying elements. Based on these mechanisms, phase field simulations are able to reproduce both the coarsening resistance and solute segregation profiles observed in Al-Cu-Mn-Zr-Si alloys, in which Mn and Zr are slow-diffusing elements with the potential to reduce interfacial energy.

Finally, the effectiveness of Mn and Zr in stabilizing θ′ precipitates is dependent on the Si content of Al-Cu-Mn-Zr alloys. An optimized Si content yields alloys with reduced hardness after aging but greater hardness after high temperature thermal exposure. It is concluded that the elevated temperature performance of Al-Cu-Mn-Zr alloys depends upon a synergistic combination of thermodynamic and kinetic characteristics that are influential both in the aging step and the alloys' response to extended thermal exposure.

Table of Contents

List of Figures

List of Tables

Chapter 1

Introduction

In this chapter, we provide context for the results presented in the later chapters. Section 1.1 describes the technical demand for high-temperature-capable cast aluminum alloys and the potential for recently reported Al-Cu-Mn-Zr alloys to address that demand. Section 1.2 provides a technical background on the metallurgy of the Al-Cu system as well as describing the approaches to developing high-temperature-capable aluminum alloys used in prior work. Section 1.3 outlines the research questions that motivate the current work and the methods used to address them.

1.1. Motivation

In applications where reduced weight translates to greater energy efficiency, aluminum alloys are a mainstay in structural design [1]. The most prevalent example is transportation. The evolution of automotive and airframe design has involved an ever-greater incorporation of more low-density, high-strength materials, a trend known as "light weighting" [2, 3]. The impetus of light weighting has driven the development of many different types of materials. Among these materials, aluminum alloys have the advantage of low cost, as shown in Figure 1 [4]. Therefore, aluminum alloys have become common in applications that require high specific strength at modest costs [1]. The primary disadvantage of aluminum alloys is that their service temperature is limited compared to other structural alloy systems, as shown in Figure 2 [4]. For components such as automotive engines, this limitation imposes boundaries on which parts can be made from aluminum alloys as well as the maximum operating temperature that can be used in design [5-7]. Cost-efficient cast aluminum alloys with improved high temperature properties will be needed in the design of more efficient internal combustion engines and for other advanced engine concepts [2].

One potent example of how conventional alloys limit the design of automotive engines is the cylinder head (example shown in Figure 3). The cylinder head is the most thermally critical

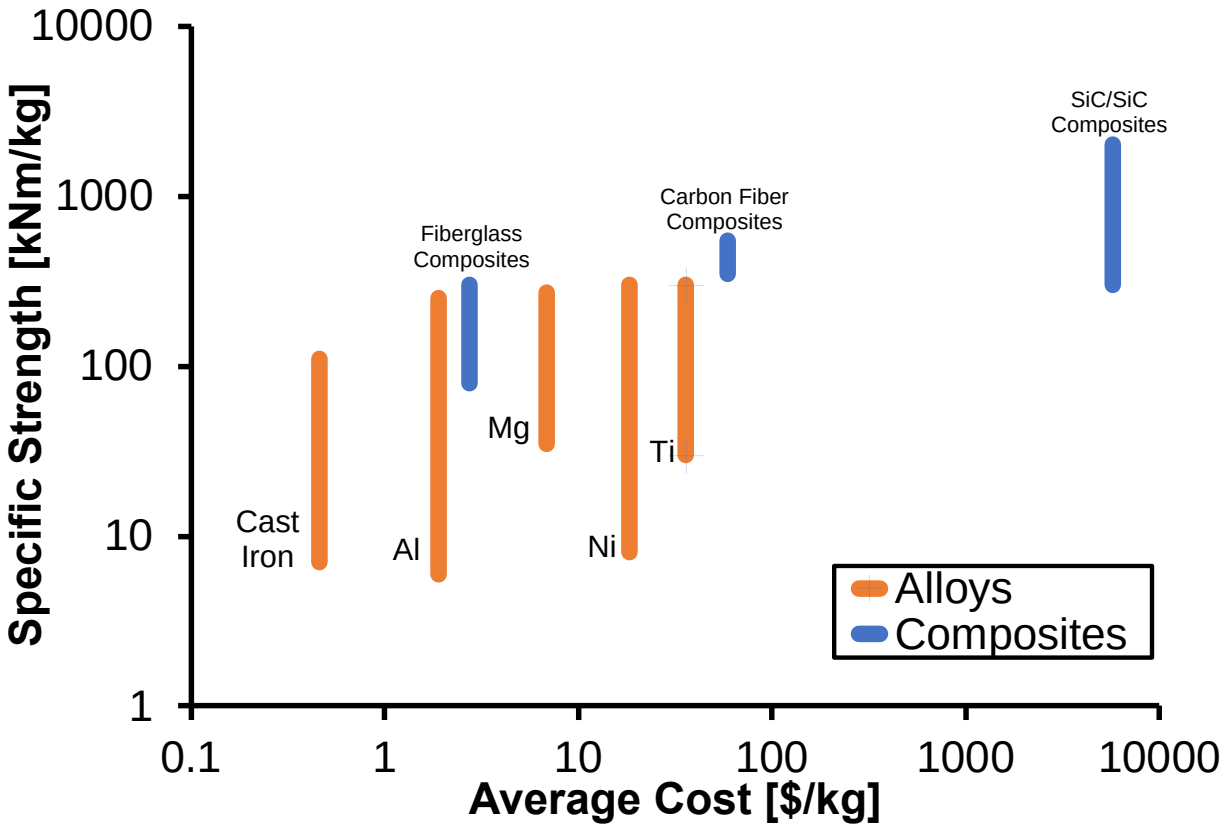

Figure 1. Specific strength of various structural materials vs. their average cost per kg [4]. Aluminum alloys provide a similar range of specific strengths at a modest cost, as compared to more expensive alloys and composite materials (note that the logarithmic scale of the axes). Cast iron is not considered a light weighting material, but is included as a reference for material affordability.

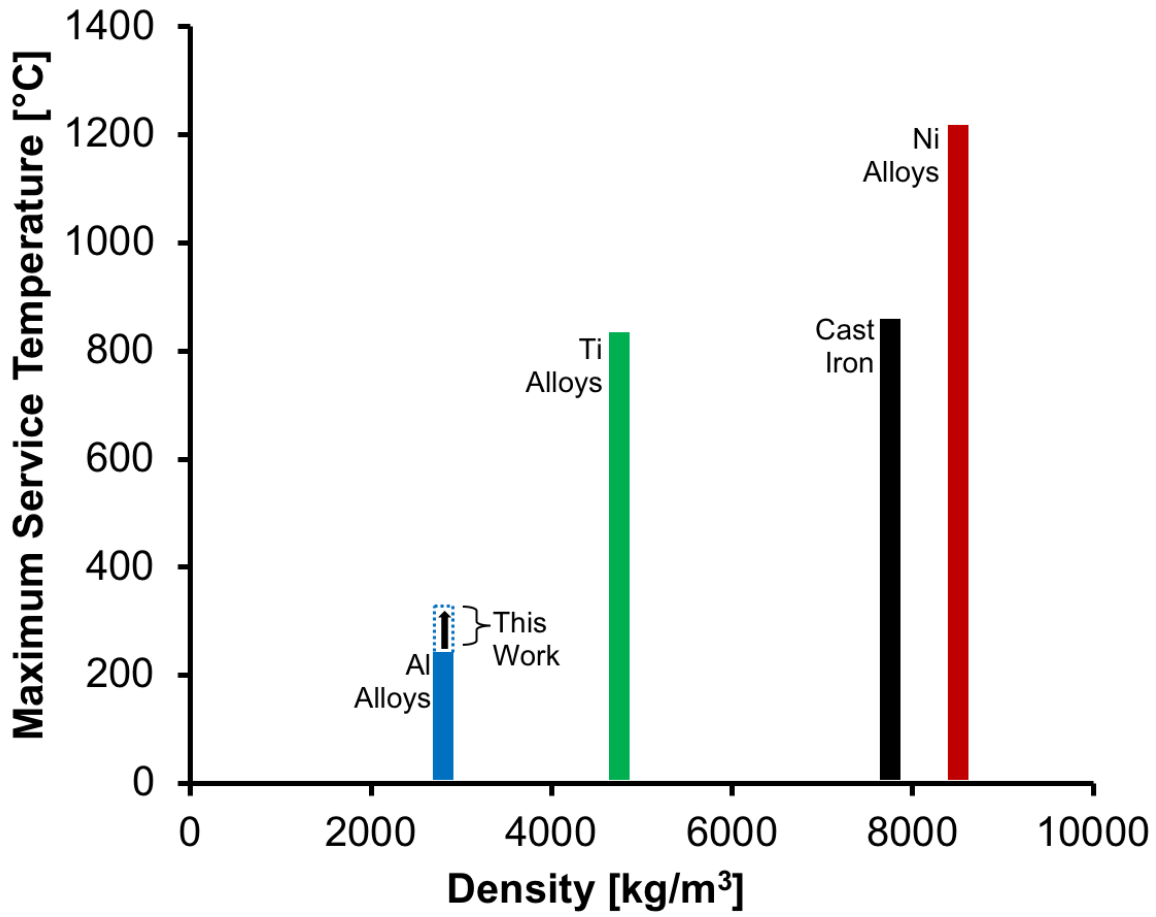

Figure 2. Density of the most commonly used structural alloys vs. their maximum service temperature [4]. Aluminum has the benefit of low density compared to other structural alloys, but its use is generally restricted to lower temperatures (note that the database used [4] referred to precipitation strengthened aluminum alloys that were suitable for the cylinder head application). In the project that this dissertation supports, aluminum alloys have been developed that effectively maintain their properties to higher temperatures than conventional alloys, as indicated on the plot.

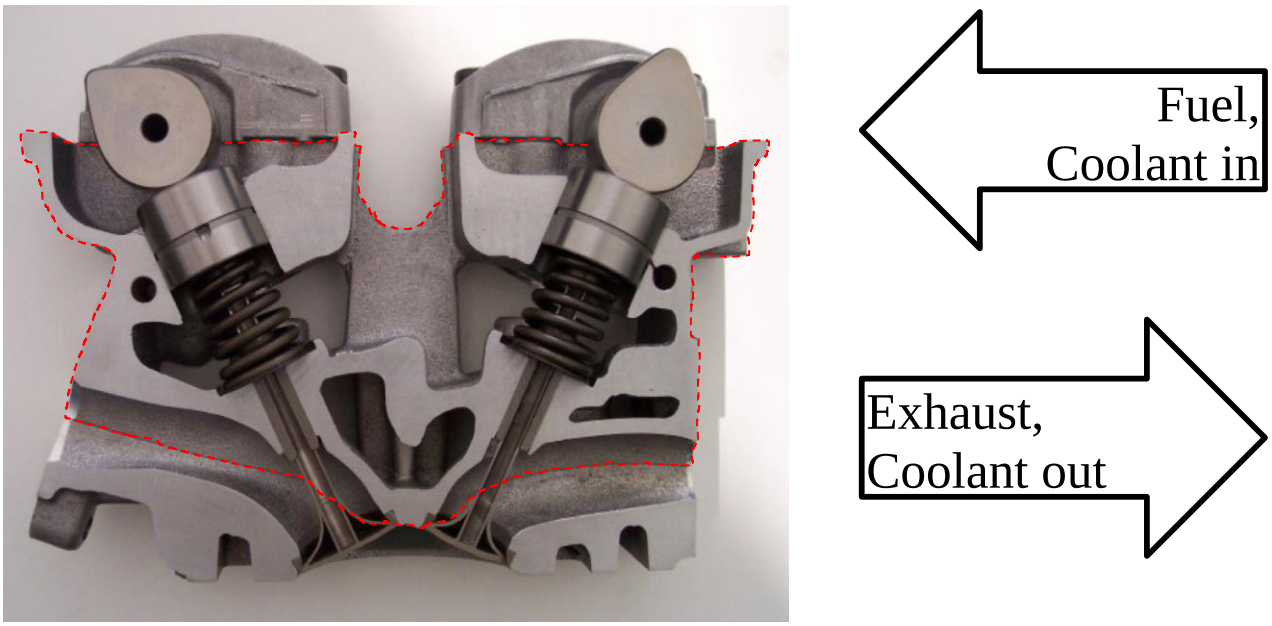

Figure 3. A representative cross section of a cylinder head (outlined in red) showing the complex geometries used to transport coolant, fuel, and hot exhaust gas through the engine. Photograph reproduced from [9].

component of light duty internal combustion engines; it accommodates around 40% of the total exothermic heat transfer during typical operation [5, 8].

The cylinder head is intricately shaped, fabricated *via* casting, with thin walls (in some areas 1 cm thick or less) [10, 11]. Engine heads experience severe temperature gradients during service [12]. As such, alloys used in the cylinder head application must have a favorable combination of castability and mechanical properties at elevated service temperature. Grey cast iron was originally used for this application [13]. From the 1960's through the 1990's, a transition to cast aluminum alloys was made for the majority of cylinder heads in light duty automotive engines [10]. Today, automotive cylinder heads are normally cast with 319 or 356 type aluminum alloys, which belong to the Al-Si-Cu and Al-Si family of alloys, respectively [2]. Because cast Al alloys have approximately one third the density of cast iron alloys, this material transition enabled significant weight savings in current generation engines [1, 2]. However, the transition also imposed a design constraint.

319 and 356 type alloys are characterized by significant softening resulting from destabilized microstructures at temperatures greater than 225 ^{o}C [14] (this detrimental microstructural evolution is described in Section 1.2). The thermal instability of these alloys limits the regimes of stress and temperature that the cylinder head can withstand during service, and represents a technological barrier to the design of advanced light duty internal combustion engines [15]. In order to overcome this barrier, cast aluminum alloys with improved high temperature performance are required. If such alloys were available, there would be an added potential to improve the performance of cylinder heads and increase the overall efficiency of the engine [5]. This technical opportunity is the motivation for ongoing alloy development efforts, including the work described in this dissertation.

For the past several years, the US Department of Energy has sponsored projects with the objective of developing precipitate-strengthened cast aluminum alloys for use in high temperature automotive engine applications [16]. The specific goals included developing alloys that had improved mechanical properties during and after exposure to high temperatures. The projects have been successful, producing alloys that effectively retained their as-aged microstructures and mechanical properties after exposure to temperatures of 350 °C (*i.e.* a potential ~125 °C increase in aluminum alloy service temperature) [14]. These high-temperature-capable alloys are based on the precipitate-strengthened Al-Cu system, with microalloying additions of Mn and Zr. It has been demonstrated that these Al-Cu-Mn-Zr alloys (or *ACMZ* alloys) also meet design requirements for castability and material costs for feasible use in cylinder head manufacturing. A full-scale cylinder head has been cast (Figure 4) and successfully completed engine testing replicating more than a lifetime of service.

The aim of this dissertation is to study and explain the composition-processing-structure-property relationships in these ACMZ alloys, particularly the thermal stability of the strengthening θ′ precipitates.

1.2. Technical Background

Before discussing the composition-processing-structure-properties relationships in Al-Cu-Mn-Zr alloys, it is worthwhile to consider the context in which they exist, as well as the fundamental metallurgical background on the Al-Cu system provided by prior work.

Many strategies have been employed in an effort to improve the high temperature mechanical properties of aluminum alloys. These include dispersion strengthening as used in hypereutectic Al-Si alloys [1, 17] and Al-ceramic composites [18-21], as well as precipitation strengthening with

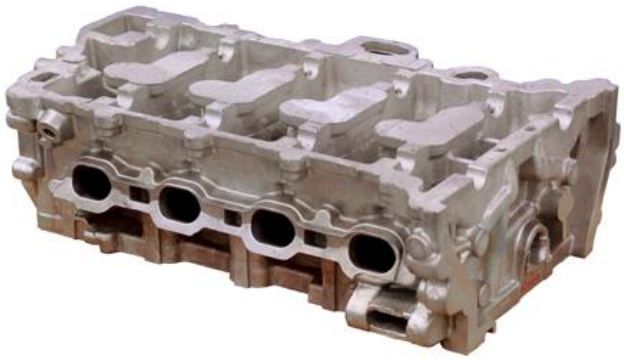

Figure 4. A full-scale cylinder head fabricated from an ACMZ alloy. Image source: Oak Ridge National Laboratory

coarsening-resistant phases, as in Al-Sc family of alloys [22-27]. Precipitation strengthening has the advantage of ductility retention and ease of fabrication [28], but the utility of the Al-Sc system is limited by the cost of Sc and its low solubility (and therefore precipitation strengthening potential) in Al [1]. The advancement leading to this dissertation is that a metastable precipitate phase in Al-Cu alloys, θ′ (tetragonal Al_2Cu), could be stabilized to temperatures of 350 °C *via* alloying additions of Mn and Zr [14]. The resulting Al-Cu-Mn-Zr alloys have excellent castability and do not incur the raw material costs associated with Al-Sc and are able to achieve greater precipitation strengthening due to the increased solubility of Cu relative to Sc [1]. Al-Cu alloys have been extensively studied, and the physical metallurgy of this system provides the fundamental basis for understanding Al-Cu-Mn-Zr alloys. In particular, the evolution of strengthening precipitates is central to the high temperature capability of these alloys. The nature of this evolution is described below.

The evolution of Al-Cu microstructures begins with solutionizing. The alloy is held at an elevated temperature (generally between 500 °C and 540 °C) for several hours [29], which dissolves any existing precipitates and allows the Cu to enter solid solution (see the phase diagram in Figure 5a). The alloy is then quenched into the two-phase field, resulting in a supersaturation of Cu atoms. Quenching is followed by the aging step, in which the supersaturated Cu come out of solid solution to form Cu-containing precipitates. During aging, the precipitates will generally undergo evolution between a series of metastable phases, GP I → θ″ → θ′ [30]. If aging is carried out above the solvus temperature for a given phase, the next phase in the sequence will precipitate directly, as indicated in Figures 5a and 5b. These metastable phases interact with dislocations to strengthen the alloy, as shown schematically in Figure 5c [32].

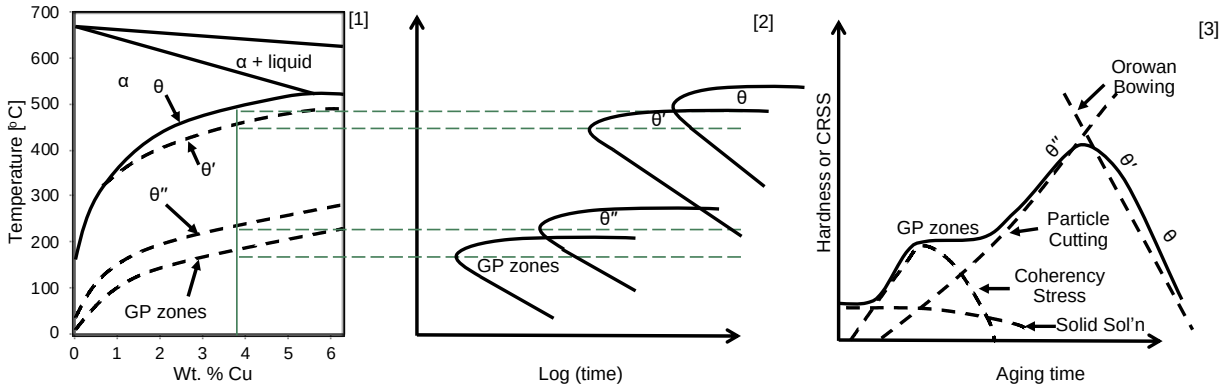

(a) (b) (c)

Figure 5. (a) Phase field diagram of the Al-Cu binary system, showing the approximate solvus temperatures of the various metastable strengthening phases [30]. (b) Schematic Time-Temperature-Transformation diagram showing which precipitates nucleate first depending on the aging temperature [31] (c) Schematic aging curve of Al-Cu alloys, indicating the strengthening effect of each precipitate phase [32]. Maximum strength is achieved when θ′ or θ″ is formed in the α-Al matrix. Overaging leads to the formation of the θ phase, which dramatically reduces alloy strength.

The mechanical properties of as-aged Al-Cu alloys depend heavily on the volume fraction, number density, and aspect ratio of the strengthening precipitates [33]. For many commercial cast Al-Cu and Al-Si-Cu alloys, the primary strengthening precipitates are nanoscale, disc-shaped particles of the metastable θ′ phase (body centered tetragonal Al_2Cu, a=4.04 Å and c=5.80 Å) [1]. The as-aged microstructures in these alloys are populated by θ′ precipitates with a high number density and average aspect ratio (diameter/thickness) in the range of 25-50 [30]. This microstructure provides strength to as-aged Al-Cu alloys used in structural applications, but it is sensitive to temperature.

If an alloy is exposed to elevated temperatures after aging (in service, for example), there is a risk of this microstructure becoming destabilized (or "overaging"). Above approximately 225 °C, the as-aged microstructure of Al-Cu deteriorates as θ′ particles coarsen [1, 6, 7, 34-36]. Larger particles grow at the expense of smaller particles, and individual particles also undergo shape evolution, reducing their aspect ratio [30, 37]. As a result, the number density and aspect ratio of precipitates in these alloys tend to decrease.

Eventually, this morphological evolution leads to a phase transformation as the detrimental, equilibrium θ phase (tetragonal Al_2Cu) nucleates in the coarsened microstructure (shown schematically in Figure 6) [30, 38, 39]. The formation of the θ phase further accelerates the coarsening process because it has high-energy, incoherent interfaces with the Al matrix [40, 41]. The θ phase coarsens at the expense of finer θ′ particles, and the mechanical properties of the alloy deteriorate substantially following this phase transformation [1, 6]. Figure 7 illustrates this relationship. The plot shows hardness measured at room temperature after as-aged alloys were exposed to a range of temperatures for 200 hours. Conventional Al-Cu(-Si) alloys lose much of their strength after exposure at 250 °C and above. The reduced mechanical properties limit the usefulness of many Al-Cu(-Si) alloys at elevated temperatures [2]. It is, therefore, desirable to

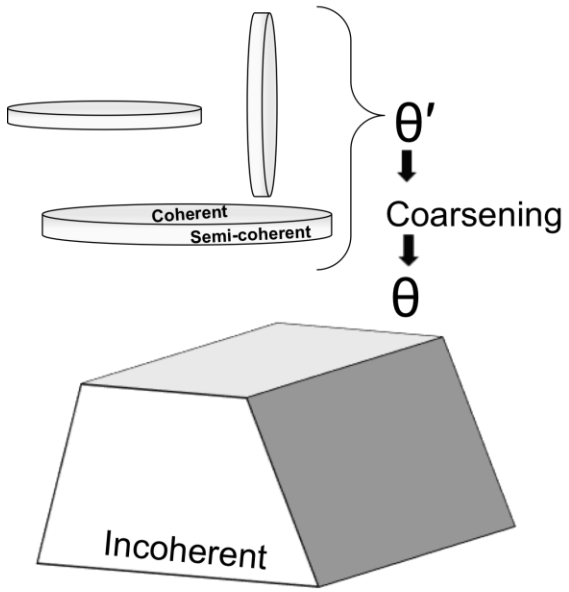

Figure 6. Schematic representation of the θ′ to θ phase transformation that takes place in Al-Cu alloys during overaging. θ′ precipitates are nano-scale and disk-shaped. During high temperature exposure, θ′ particles coarsen and transform into the coarse, blocky θ phase which is detrimental for mechanical properties.

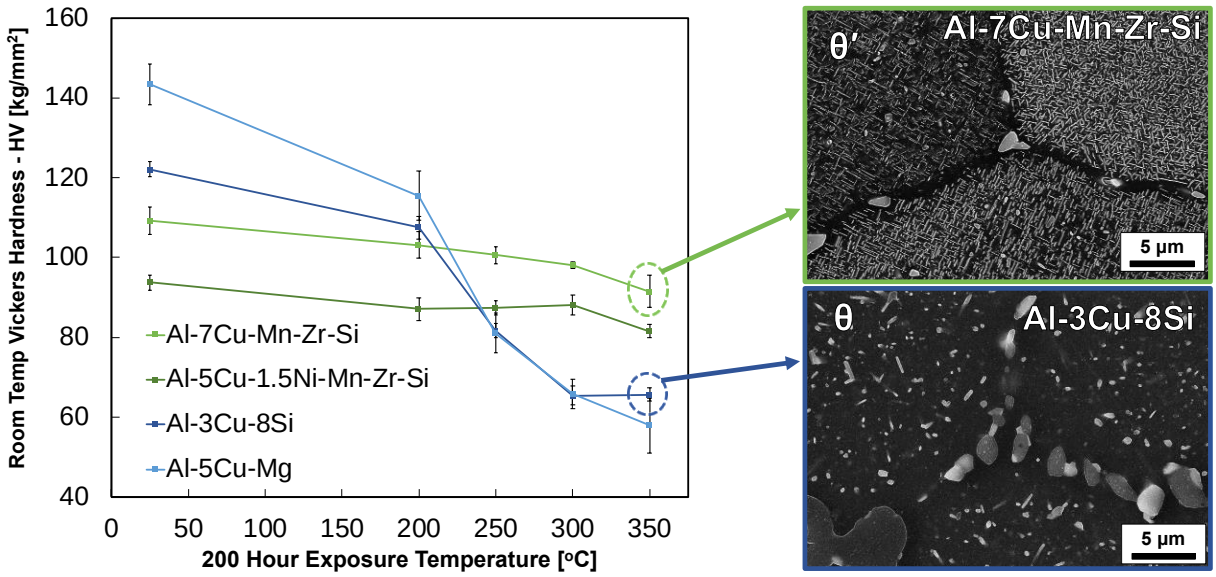

Figure 7. The hardness of conventional Al-Cu(-Si) alloys shown in blue decreases dramatically after exposure to temperatures above 225 °C, because the strengthening θ′ precipitates in their microstructure evolve in to θ. Conversely, Al-Cu-Mn-Zr-Si alloys shown in green retain their as-aged, θ′ populated microstructure after high temperature exposure and therefore exhibit minimal hardness loss.

develop alloys in which the onset of θ′ to θ transformation is delayed or prevented at elevated temperatures.

Such high temperature stabilization of θ′ has been recently reported. The addition of Mn and Zr to an Al-Cu alloy results in a microstructure in which the θ′ phase is morphologically stable to a temperature of at least 350 °C [14]. Mn and Zr segregate to the interfaces of θ′, apparently increasing its thermal stability [14]. The increased thermal stability of θ′ improves the alloy's creep resistance [34], elevated temperature yield strength [42], and room temperature hardness after prolonged thermal exposure, as shown in Figure 7 [14].

1.3. Research Objectives

This dissertation seeks to explain why Al-Cu-Mn-Zr alloys better retain their as-aged properties after high temperature exposure, as shown in Figure 7. This involves probing the composition-processing-microstructure-properties relationships that exist in these alloys. The critical aspects of these relationships are broken down into five central questions, each of which is addressed in a separate chapter.

- What causes the onset of θ′ to θ transformation?
- Is the stability of θ′ at elevated temperatures more sensitive to modified thermodynamics or modified kinetics?
- What role do Mn and Zr play in providing these alloys with microstructural stability?
- What role does the impurity level of Si play in providing these alloys with microstructural stability?
- How do varying amounts of θ′ and θ precipitates affect deformation in these alloys?

The methods used to address these questions include both experimental results and theoretical analysis. Experimental results provide descriptions of the alloy composition, processing, microstructure, and properties, while theoretical analysis is used to study the relationship between these data points. Figure 8 gives an overview of the methods used in this work, while each chapter provides specific detail on procedures. By combining these methods, it is possible to present an improved understanding of Al-Cu-Mn-Zr alloy behavior from alloy chemistry to elevated temperature mechanical properties.

This work involved the development of new methods, especially in terms of phase field modeling (described in Chapters 5, 6, and 7). In addition to the results that the phase field studies provide, this dissertation aims to communicate the utility of these new methods and explain how they may be applied in future work.

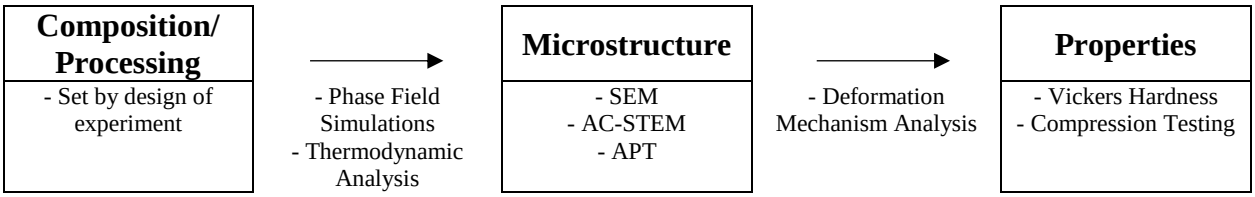

Figure 8. A summary of experimental and theoretical methods used in this work.

Chapter 2

The Effects of Microstructural Stability on the Compressive Response of two Cast Aluminum Alloys up to 300 ^{o}C

This chapter is revised based on a published journal article with Patrick Shower as lead author:

P. Shower, S. Roy, C.S. Hawkins, A. Shyam, The effects of microstructural stability on the compressive response of two cast aluminum alloys up to 300°C, Materials Science and Engineering: A 700 (2017) 519-529.

My primary contributions to this paper include (i) microstructural analysis (ii) identification of deformation and dynamic softening mechanisms (iii) literature review (iv) most of the writing.

Abstract

In this study, the high temperature compressive response of cast aluminum alloys 319 and RR350 are compared in light of their microstructures. The 319 alloy is widely used in thermally critical automotive applications and provides a baseline for comparison with the RR350 alloy, whose microstructural stability at high homologous temperatures was recently reported. Cylindrical compression samples from each alloy were tested at four temperatures up to 300 ^{o}C at a constant true strain rate varied over four orders of magnitude. Although both alloys are strengthened by metastable θ′ precipitates (nominally Al_2Cu) in the as-aged condition, their mechanical response diverges at temperatures greater than 250 ^{o}C as the strengthening precipitates coarsen and evolve in the 319 alloy while they retain their as-aged morphology in the RR350 alloy. Deformation mechanisms of each alloy are examined using microstructural analysis and empirical activation energy calculations. The stability of the θ′ phase in the RR350 alloy leads to effective precipitation hardening at homologous temperatures up to 0.6 and an extensive regime of grain boundary controlled deformation.

2.1. Introduction

Cost-efficient cast aluminum alloys with improved high temperature mechanical properties will be needed in the design of more efficient internal combustion engines and for other advanced engine concepts [2]. This is particularly true in the design of the cylinder head for automotive engines. The cylinder head is the most thermally critical component of light duty internal combustion engines; it transmits around 40% of the total exothermic heat transfer during typical operation [8]. Automotive cylinder heads are normally cast with 319 or 356 type alloys, which belong to the Al-Si-Cu and Al-Si family of alloys, respectively [2]. These alloys are characterized by significant softening resulting from destabilized microstructures at temperatures greater than 250 ^{o}C [2, 7].

In this study, the microstructure and compressive response of two cast aluminum alloys from the Al-Si-Cu (319) and Al-Cu-Ni (RR350) alloy systems are compared. 319 and RR350 are both cast, precipitation hardened alloys that are primarily strengthened by the metastable θ′ (tetragonal Al_2Cu) precipitate phase. The 319 alloy is characterized by an α-Al matrix populated with an array of nanoscale, disc shaped, crystallographically oriented θ′ particles after the typical –T7 overaging treatment [7]. When the 319 alloy is held at temperatures above 250 ^{o}C, these particles rapidly coarsen, followed by evolution into the equilibrium θ phase (body centered tetragonal Al_2Cu). The θ phase is incoherent with the α-Al matrix, resulting in accelerated particle coarsening and a blocky/globular morphology without crystallographic orientation. This thermally driven progression from nanoscale θ′ to coarsened θ′ to incoherent θ is accompanied by substantial reduction in tensile yield strength [6, 7, 35]. The upper limit of service temperature for the 319 alloy is, in practice, related to the phase stability of θ′ precipitates [2, 35, 36, 43, 44].

In comparison to the 319 alloy, the RR350 alloy is an Al-Cu-Ni alloy characterized by slightly larger θ′ particles (with a similar aspect ratio and a lesser number density after aging) that undergoes reduced thermal softening due to the exceptional stability of its strengthening precipitates up to a temperature of 350 ^{o}C [14]. Thus, the deformation response of the 319 and RR350 alloys is expected to diverge at elevated temperatures. The objective of this work was to identify the nature, degree, and microstructural basis of divergence in the elevated temperature compressive response of these two alloys. In order to meet this objective, compression testing was performed at a range of strain rates and temperatures. Compression testing was chosen for this study because it yields true stress – true strain behavior at strains beyond those possible in tensile testing [45]. Compression testing also offers information about the kinetics of recovery and recrystallization as well as total deformation energy [45-47]. Compression testing is often utilized in order to simulate processing parameters for the optimization of hot-forming. However, in the present study it is used for the purpose of systematically evaluating mechanical properties and deformation mechanisms as a function of strain rate and testing temperature. An extended hold (200 hours) at testing temperature prior to compression was incorporated into the experimental design to allow sufficient time for microstructural evolution to occur and the microstructure to reach a steady state. This is a standard practice used in the automotive industry to evaluate the thermal stability of an alloy's as-aged microstructure, and is often referred to as "preconditioning". Preconditioning provides a baseline for comparison between the microstructure and mechanical property of alloys at different temperatures. Characterization of post-compression microstructures included Electron Backscatter Diffraction (EBSD), which has been applied by other researchers to identify dynamic softening mechanisms [46, 48-51] and to quantify phenomena such as strain hardening and energy dissipation [45-49, 51].

There has been limited prior work to describe the link between the thermal evolution of strengthening precipitates in cast aluminum alloys and the deformation mechanisms that become active in these alloys at elevated temperatures. By comparing the compressive response of the 319 and RR350 alloys over a wide range of temperatures and strain rates, the present study develops a fundamental understanding of the effects of the thermal stability of strengthening precipitates on the elevated temperature deformation response of cast aluminum alloys.

2.2. Materials and Methods

2.2.1. *Materials*

Two aluminum alloys were studied, with compositions given in Table 1. Each composition was melted at 800^{o} C or above and gravity wedge die cast in a sand mold. The alloy compositions were verified via inductively coupled plasma optical emission spectrometry (ICP-OES) and inductively coupled plasma mass spectroscopy (ICP-MS) [14].

Keel blocks were taken from the same location in each casting, which produced uniform microstructures with an average grain size of ~ 46 μm in the RR350 alloy and an average secondary dendrite arm spacing (SDAS) of ~ 30 μm in the 319 alloy (measured via the mean linear intercept method **[52]**). For alloys with dendritic microstructures (such as 319) SDAS is analogous to grain size (in equiaxed microstructures) in determining the effect of Hall-Petch strengthening **[1]**. The keel blocks were solutionized, quenched in water at a minimum temperature of 80 ^{o}C, aged (see Table 2), and held for 200 hours at preconditioning temperatures (200 ^{o}C, 250 ^{o}C, 300 ^{o}C). The compression testing temperature complimented the preconditioning temperature, e.g., specimens preconditioned at 250 ^{o}C were also tested at 250 ^{o}C. From the keel blocks, cylindrical compression testing specimens 10 mm in diameter and 15 mm in height were machined. The height to diameter ratio was thus maintained at 1.5 in order to avoid friction effects from the compression platens and

Table 1. Composition of the 319 and RR350 alloys used in this study in terms of weight percent. Major differences include the presence of Si in the 319 alloy and the presence of Ni , Co, Sb and Zr in the RR350 alloy. A blank box indicates that the element was not detected.

Alloy	**Si**	**Cu**	**Mg**	**Zn**	**Fe**	**Ni**	**Mn**	**Co**	**Zr**	**Ti**	**Sb**	**Al**
319	8.29	3.17	0.34	0.31	0.68	0.03	0.39			0.17		86.62
RR350	0.03	5.02		0.01	0.09	1.50	0.20	0.25	0.17	0.21	0.15	92.37

Table 2. Heat treatment schedules for the 319 and RR350 alloys. The aging treatment for the 319 alloy is similar to that prescribed for –T7 overaging [1].

Alloy	**319**		**RR350**	
Solutionizing treatment	490 ^{o}C	5 hours	535 ^{o}C	12 hours
Aging treatment	240 ^{o}C	5 hours	210 ^{o}C	4 hours
Preconditioning	200 – 300 ^{o}C	200 hours	200 – 300 ^{o}C	200 hours

buckling during compression **[53]**. These specimens had compression surfaces perpendicular to the axis within 0.25° and parallel to each other within 6.4 μm.

2.2.2. *Compression Testing*

The compression tests were performed using an MTS 312.21 servo-hydraulic mechanical universal testing frame coupled with a resistance furnace. Three equally spaced thermocouples were used on the compression samples, held within 2 mm of the specimen surface *via* a foil wrap around the specimen.

Dry graphite lubricant was used, and no depressions were machined on the ends of the sample in contact with the platens. The samples were inserted at room temperature, held in place by a compressive force of approximately 10 lbs, heated to their previous preconditioning temperatures (200 ^{o}C, 250 ^{o}C, 300 ^{o}C) at a rate of approximately 0.5 ^{o}C per second and held at temperature for 20 minutes to allow thermal equilibration, as per ASTM standards E209 and E21 [54]. Specimen temperature was maintained for the duration of the compression test as shown in Appendix A. In addition, room temperature (25 ^{o}C) compression testing was performed on as-aged specimens.

At all testing temperatures, the cylindrical samples were compressed at a constant true strain rate of 10^{-4}, 10^{-3}, 10^{-1}, or 10^{0} per second to a true strain of -0.150 (engineering strain of -0.139). A single sample from each alloy was tested at each of these conditions. Strain was measured with an MTS 632.53E-14 high temperature extensometer, by contact between the extensometer probes and the outer diameter of the compression platens. Thermal expansion during sample heating was accounted for, such that strain value was zeroed at the beginning of the compression test. The constant true strain rate was maintained using an MTS 407 controller with custom LabVIEW software that continually monitored the strain reading from the extensometer and controlled the

true strain rate of the compression test in real time, based on the change in position between sampling points. For the fastest strain rates, the platen position was sampled and corrected based on 40,000 samples per second. After compression, the specimens were air cooled at approximately 1°C to 2 °C per second.

2.2.3. *Kinetic Analysis*

For the purpose of comparing the compressive response of the 319 and RR350 alloys, the flow stress (σ_F) is defined as σ_{true} measured at ε_{true} = -0.05. The use of this metric eliminates any ambiguity in determining yield stress of alloys whose elastic and plastic regimes are not clearly delineated. Flow stress was used in the kinetic analysis of true stress – true strain data as described below.

Strain rate sensitivity (m) is defined as the change in flow stress with respect to strain rate at a given temperature, as follows [55]:

$$m = \left|\frac{\partial(\ln(\sigma_F))}{\partial(\ln(\dot{\varepsilon}))}\right|_T \quad (1)$$

where $\dot{\varepsilon}$ is strain rate. This slope was found using linear regression.

The relationship between flow stress and strain rate at elevated temperature can be described by the kinetic rate equation [55, 56]:

$$\dot{\varepsilon} = A \cdot \sigma_F^n \cdot e^{-\left(\frac{Q}{R \cdot T}\right)} \quad (2)$$

where A is the frequency factor, Q is the apparent activation energy (the activation energy associated with the rate-controlling deformation process [57]), R is the ideal gas constant, T is absolute temperature, and n is the stress exponent (by definition, the inverse of m). From Eq. 2, Q can be calculated as shown in Eq. 3 below. In order to calculate the empirical value of Q, the slope $\frac{\partial(\ln(\sigma_F))}{\partial(T^{-1})}$ was determined for each strain rate using linear regression. In addition to the

temperature dependent value of n, this led to a unique calculation of activation energy for each testing condition. Given the activation energy, the temperature compensated strain rate parameter, also called the Zener-Holloman parameter (Z), can be calculated as shown in Eq. 4 [58].

$$Q = \left|\frac{\partial(\ln(\sigma_F))}{\partial(T^{-1})}\right|_{\dot{\varepsilon}} \cdot n \cdot R \quad (3)$$

$$Z = \dot{\varepsilon} \cdot e^{-\frac{Q}{R \cdot T}} \quad (4)$$

2.2.4. *Microstructural Characterization*

After compression testing, the cylindrical specimens were sectioned along the compression direction to expose the region of true uniaxial compression (in the center of the specimen) [59]. After polishing and etching with Keller's reagent (by volume: 95% H_2O, 2.5% HNO_3, 1.5% HCl, 1% HF) the region of true compression was examined with microscopy and energy dispersive spectroscopy (EDS) using a Hitachi S4800 Field Emission Gun - Scanning Electron Microscope (FEG-SEM) in secondary electron (SE) mode. Initial material specimens taken from the keel blocks after aging and after preconditioning at 300 ^oC for 200 hours were also examined using this FEG-SEM.

2.2.5. *EBSD*

EBSD scans were performed on the as-aged RR350 alloy as well as compression tested specimens of both alloys as given in Table 3. These conditions were chosen in order to span the testing conditions from most conducive for thermally activated phenomena (e.g. T = 300^{o}C, $\dot{\varepsilon}$ = 10^{-4} s-1) to least conducive (e.g. T = RT, $\dot{\varepsilon}$ = 1 s^{-1}). In the compressed specimens, the scans were taken in the region of true compression. A JEOL 6500 FEG-SEM was used to collect the data and TSL

Table 3. Parameters used for EBSD scans in this study.

Alloy	Condition	Step Size	Scan Area	Working Distance
319	25 ^{o}C, 1 s^{-1}	1 μm	750 μm x 750 μm	21 μm
	250 ^{o}C, 10^{-4} s^{-1}	1.9 μm	1000 μm x 1000 μm	20 μm
	300 ^{o}C, 10^{-4} s^{-1}	1.5 μm	750 μm x 750 μm	20 μm
RR350	25 ^{o}C, 1 s^{-1}	0.5 μm	400 μm x 300 μm	20 μm
	250 ^{o}C, 10^{-4} s^{-1}	1 μm	550 μm x 500 μm	18 μm
	300 ^{o}C, 10^{-4} s^{-1}	1 μm	550 μm x 500 μm	18 μm
	As-aged	0.5 μm	500 μm x 500 μm	20 μm

2.3. Results

2.3.1. *Compressive Response of the 319 and RR350 alloys*

All stress – strain curves for both alloys are shown in Figure 9, organized by temperature and strain rate.

The flow stress (σ_F) for both alloys under each testing condition is shown in Figure 10. At all strain rates, the 319 alloy has a higher flow stress than the RR350 alloy at 25^{o}C and 200 ^{o}C, but the RR350 alloy has a higher flow stress than the 319 alloy at temperatures of 250 ^{o}C and 300 ^{o}C.

The strain rate sensitivity for the two alloys was calculated at each testing temperature according to Eq. 1 and is listed in Table 4. At temperatures up to 200 ^{o}C, the strain rate sensitivity of the two alloys is similar. Above 200 ^{o}C, the strain rate sensitivity of the 319 alloy is greater than that of the RR350 alloy.

Apparent activation energy was calculated according to Eq. 3 for all tests conducted at 200 ^{o}C and above (Q cannot be computed at 25 ^{o}C, because the value of m is zero at this temperature for both alloys), and a contour map of apparent activation energy as a function of strain rate and temperature is shown in Figure 11.

For the data collected in this study, there is a linear relationship between the values of $\ln(\sigma_F)$ and $\ln(Z)$ (Eq. 4) for each alloy at each strain rate (minimum R^2 values of 0.950 for the 319 alloy and 0.971 for the RR350 alloy). Generally, a good linear fit for this data confirms that the kinetic rate equation (Eq. 2) is obeyed in a given temperature and strain rate range [36, 55]. It was important to validate the kinetic rate equation in this study, given that its derivation assumes a constant microstructure.

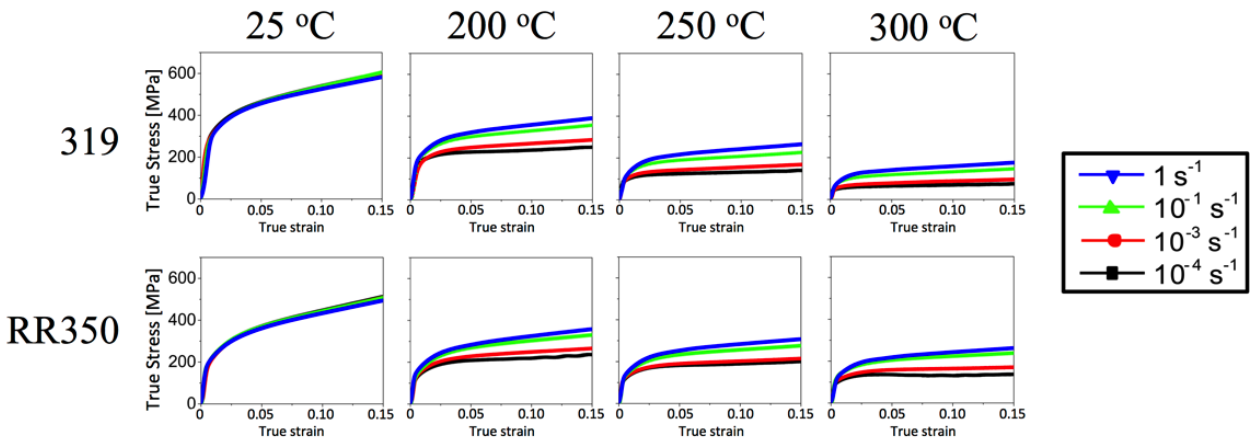

Figure 9. True stress – true strain curves for the 319 and RR350 alloys compressed at a range of strain rates and temperatures. Both alloys demonstrate monotonic strain hardening under the conditions tested, except for the RR350 alloy at 10^{-4} per second and 300 °C. Note that the alloys are not strain rate sensitive at 25 °C (in agreement with [36]) and that their strain rate sensitivity increases with temperature.

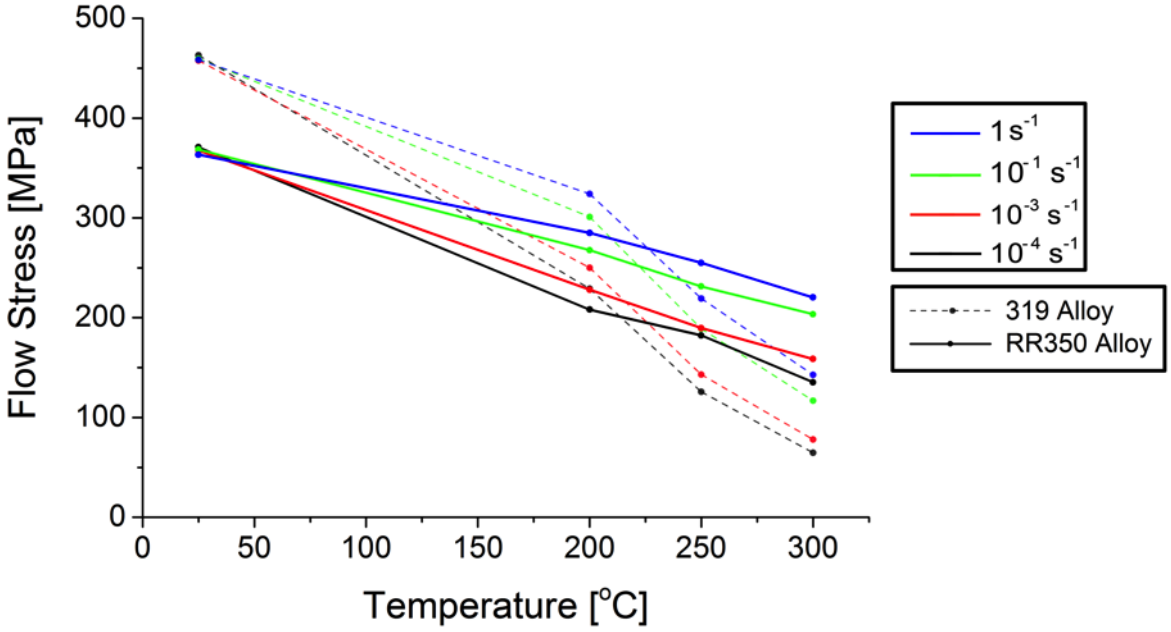

Figure 10. Trends in flow stress vs. testing temperature of the two alloys as a function of strain rate. The 319 alloy has a greater flow stress at 25 ºC and 200 ºC, but a lower flow stress at 250 ºC and 300 ºC, indicating reduced thermal softening for the RR350 alloy.

Table 4. Strain Rate Sensitivity (m) vs. Temperature for the 319 and RR350 alloys. The strain rate sensitivity of the 319 alloy increases more rapidly with increasing temperature.

Temperature (ºC)	**Value of m for 319**	**Value of m for RR350**
25	0.00 ± 0.001	0.00 ± 0.001
200	0.04 ± 0.001	0.03 ± 0.001
250	0.06 ± 0.001	0.04 ± 0.003
300	0.09 ± 0.001	0.05 ± 0.004

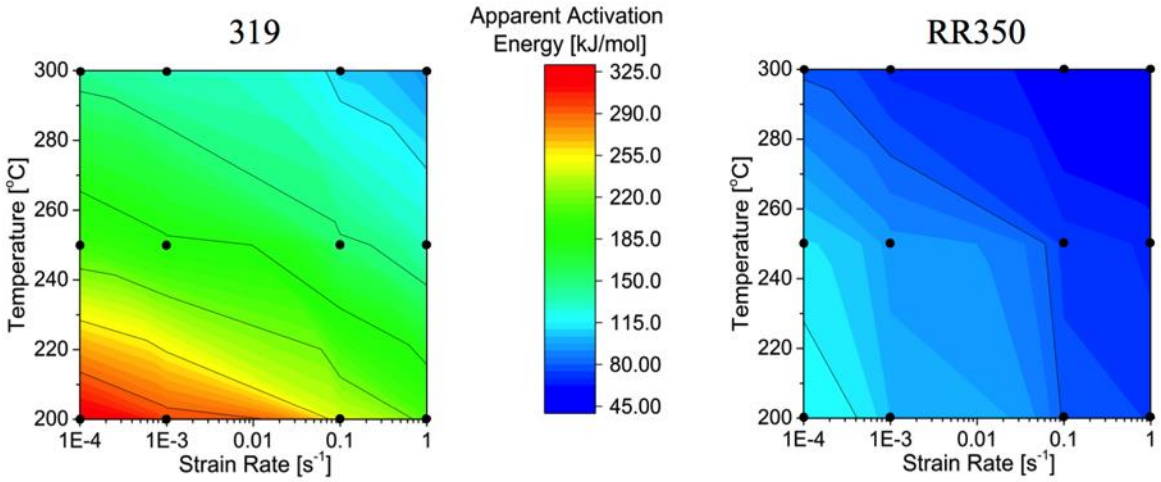

Figure 11. Apparent activation energy maps calculated for each alloy. The black dots represent the data points from which the map is interpolated using a modified Shepard's method [60]. Note that the activation energy for the RR350 alloy is more consistent across testing conditions, is less temperature dependent, and is lower in value at all conditions as compared to the activation energy for the 319 alloy.

2.3.2. *Microstructure of the 319 alloy*

As-aged and Preconditioned

The microstructure of the 319 alloy after aging and after preconditioning is described in recent work by Roy *et al.* [6, 7]). As expected, nanoscale θ′ particles populate the bulk of secondary dendrites in the 319 alloy after aging. After preconditioning at 200 ^{o}C and above, coarsened θ′ precipitates and θ particles were observed. θ particles became more prominent and precipitate size became less uniform as preconditioning temperature increased.

Post-Compression

The region of pure compression was examined in each specimen after compression testing. In all samples, fractured eutectic and intermetallic particles as well as voids were often observed where multiple secondary dendrites met in the observation plane. Examples of these observations are shown in Figure 12.

2.3.3. *Microstructure of the RR350 alloy*

As-aged

After aging, the RR350 alloy had a microstructure characterized by equiaxed grains and an intergranular space populated by coarse intermetallic particles containing various proportions of Ni, Fe, Co, Mn, and Cu (verified by EDS), as shown in Figure 13a. Within the bulk of the grains, the α-Al matrix was populated by microscale θ′ precipitates, as shown in Figure 13b.

Preconditioned

After preconditioning for 200 hours at 300 ^{o}C, the microstructure of the RR350 alloy (shown in Figure 14) appeared to be relatively unchanged from the as-aged condition under SEM observation. The θ′ particles remained crystallographically aligned and of uniform dimensions.

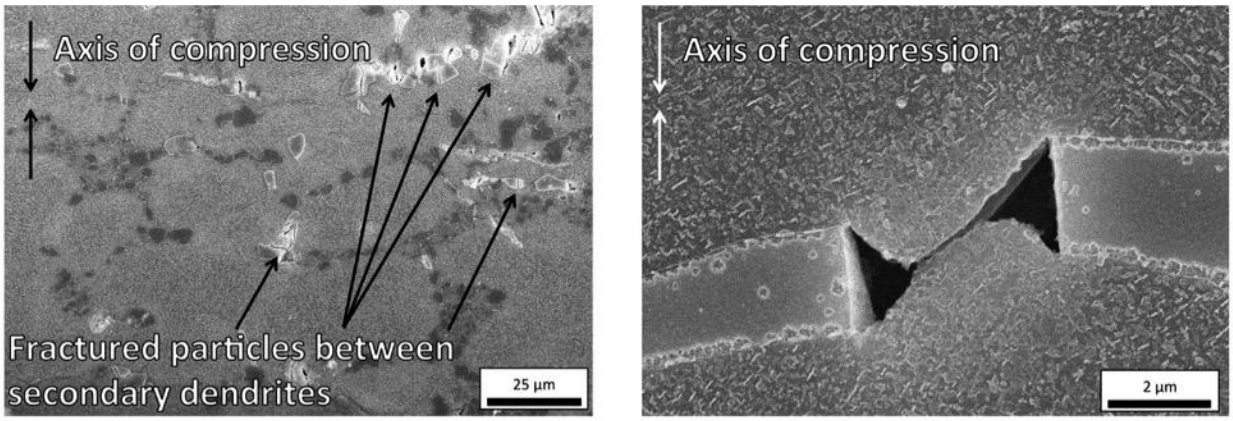

(a) Overview of post-deformation microstructure

(b) Fractured particle between secondary dendrites surrounded by θ and coarsened θ′ precipitates populating the α-Al matrix

Figure 12. SEM micrographs showing the microstructure of the 319 alloy after compression. (a) Sample compressed at 250 ^{o}C and 10^{-1} per second showing how eutectic and intermetallic particles between secondary dendrites tend to fracture parallel to the axis of compression. (b) Sample compressed at 200 ^{o}C and 10^{-4} per second showing a fractured particle between secondary dendrites populated by coarse precipitates. The intrusion of the α-Al matrix into the fracture suggests that the particle fractured early in the deformation process.

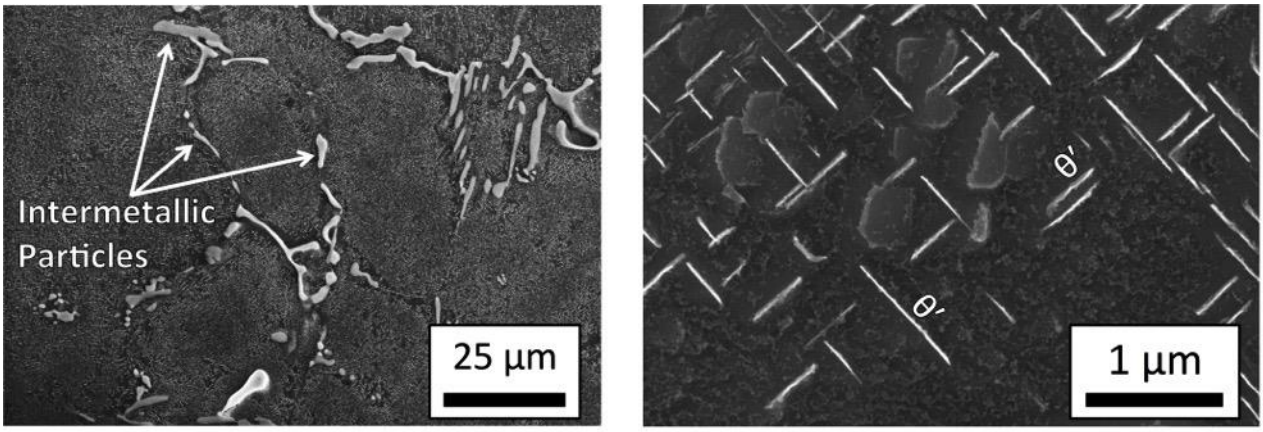

(a) Overview (b) θ′ precipitates

Figure 13. Microstructure of the as-aged RR350 alloy, characterized by an equiaxed grain structure and an average grain size of ~ 46 µm. (a) Shows that the grain boundaries are populated by coarse intermetallic particles. (b) Shows that the bulk of the grain is populated by microscale θ′ particles, plate shaped and crystographically aligned.

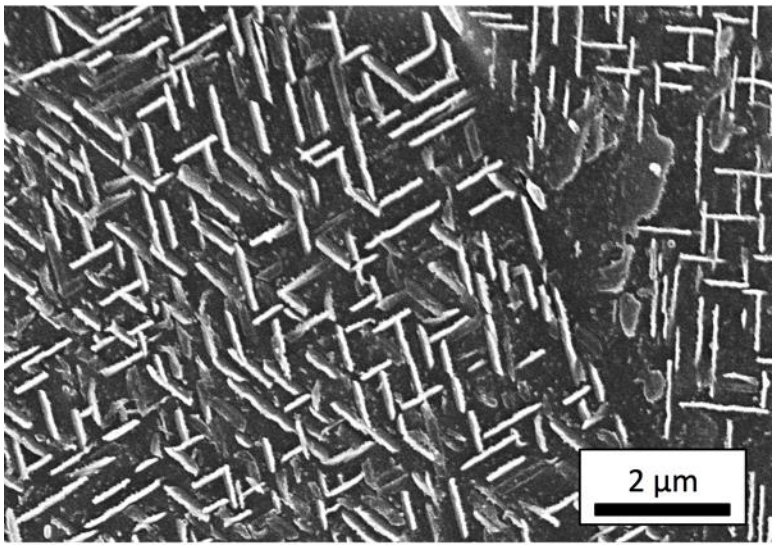

Figure 14. Microstructure of the RR350 alloy after preconditioning for 200 hours at 300 ^{o}C. No changes in the precipitate morphology or grain structure compared to the as-aged condition were apparent.

Post-compression

In every sample, θ′ appeared to be crystallographically aligned and uniform in morphology. In the region of true compression, it was consistently observed that θ′ particles whose length was oriented parallel to the axis of compression were bent or shorn in appearance. It was further noted that these shorn particles were aligned in such a way to suggest shear bands through the bulk of each grain, oriented at approximately +/- 45^{o} relative to the axis of compression (see Figure 15).

Voids and cracked intergranular particles were observed at triple points in all samples. Decohesion of grain boundaries was also observed, as seen in Figure 16.

2.3.4. *Dynamic Softening Mechanisms*

Orientation Imaging Maps (OIMs) of the two alloys are shown in Figure 17 for select post-compression samples, along with the distribution of boundary misorientations as a function of testing condition.

In the 319 alloy, little variation in boundary misorientation is observed between each of the experimental conditions (Figure 17b). Under each condition, partial dynamic recovery is observed, evidenced by loops of intermediate misorientation boundaries near dendrite boundaries (not to be confused with boundaries between secondary dendrites of similar orientation) [49, 51, 56]. The extent of dynamic recovery does not increase between conditions and no evidence of recrystallization is observed [51].

In the RR350 alloy, substantial variation in boundary misorientation is observed between experimental conditions (Figure 17c). After room temperature compression, extensive low misorientation boundaries are observed due to a high density of unaligned dislocations [49]. After preconditioning and compression at 250^{o} C and 10^{-4} per second, dynamic recovery is apparent [49, 51, 56]. At 300 ^{o}C and 10^{-4} per second, intermediate misorientation boundaries are consumed and

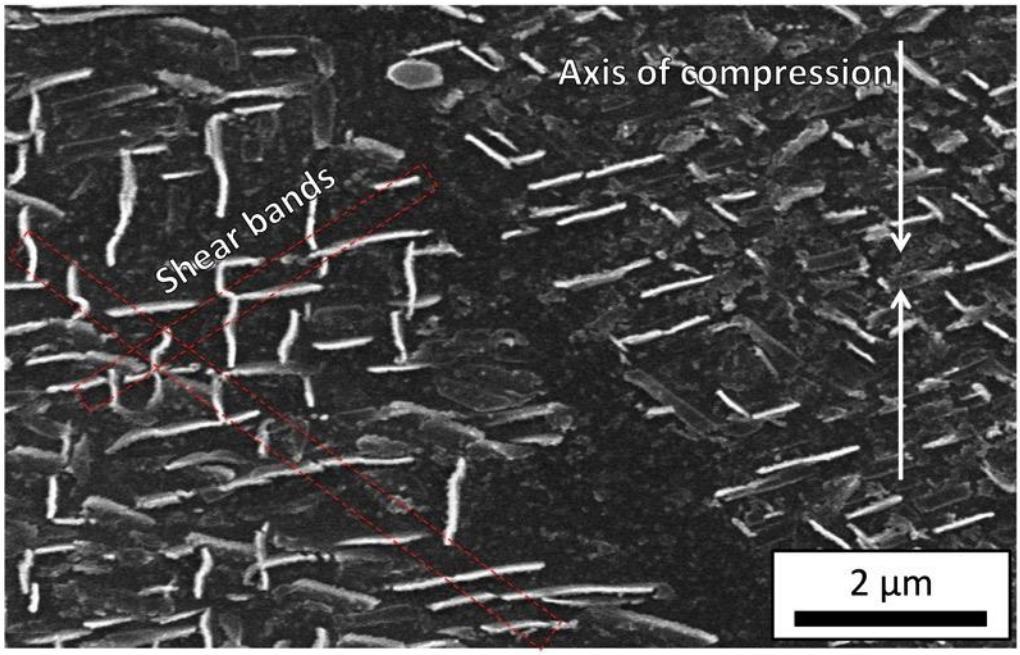

Figure 15. The RR350 alloy compressed at 300 ^{o}C and 1 per second, showing apparent shear banding in the grain bulk (red boxes). Extensive precipitate-deformation interaction is evident.

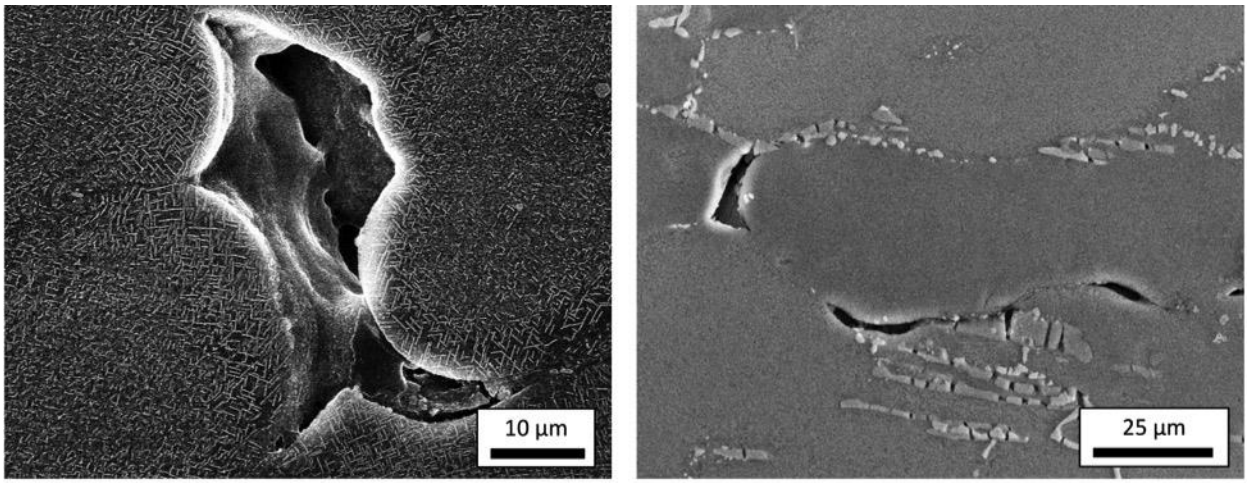

(a) RR350 compressed at 300 °C and 10^0 per second (b) RR350 compressed at 25 °C and 10^{-4} per second

Figure 16. Post-compression microstructure of the RR350 alloy under two contrasting testing conditions. (a) Shows a sample compressed at the highest temperature (300°C) and strain rate (1 per second) tested. (b) Shows a sample compressed at room temperature and the lowest strain rate (10^{-4} per second) tested. Under each condition, voids are formed at grain boundaries and triple points. Cohesion of grain boundaries is improved by the presence of intermetallics, which appear to pin adjoining grains to one another and/or interfere with vacancy diffusion along the boundary. This microstructure suggests that the cohesive strength of the bulk may be comparable to or greater than the adhesive strength of the grain boundaries.

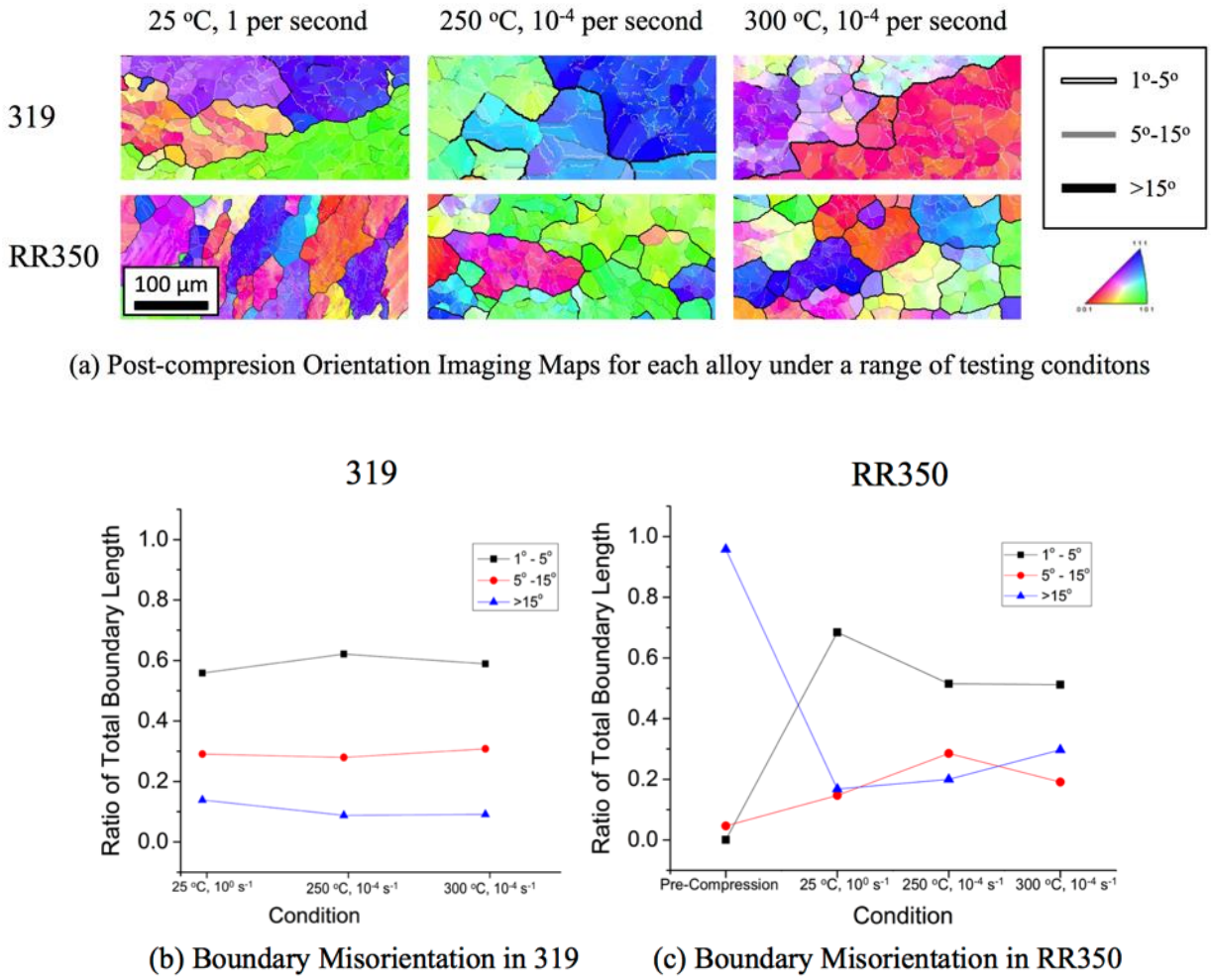

Figure 17. (a) OIMs of each alloy compressed under different conditions. Note the presence of substructure in the 319 alloy under each testing condition, and the evolution from elongated grains to grains with substructure to equiaxed, recrystallized grains as testing temperature increases in the RR350 alloy. (b) and (c) show the prominence of various boundary misorientation angles as a function of testing condition in each alloy. Data from the RR350 alloy in its pre-compressed state is included to illustrate that a typical, non-stressed microstructure is dominated by high angle boundaries. Note that the distribution of misorientation angles remains consistent in the 319 alloy while the RR350 alloy forms low angle boundaries during compression that are gradually consumed as intermediate and then high angle boundaries form during elevated temperature deformation.

high misorientation boundaries increase in prevalence, suggesting dynamic recrystallization has taken place [49, 51]. This is consistent with the OIMs for RR350 shown in Figure 17a, in which elongated grains are observed in the specimen compressed at 25 ^{o}C, a developed substructure is observed in the specimen compressed at 250 ^{o}C, and equiaxed grains with high angle boundaries are observed in the specimen compressed at 300 ^{o}C. Furthermore, this is consistent with the dynamic softening observed in RR350 under these conditions, as seen in Figure 18 below (reproduced from the data shown in Figure 9 using a smaller scale).

2.4. Discussion

2.4.1. *Defining Deformation Mechanism Regimes*

The deformation mechanisms active in each alloy under the given testing conditions were studied using several approaches. Empirical approaches included evaluation of pre-compression and post-compression microstructures (summarized in Table 5) and trends in mechanical properties (including flow stress shown in Figure 10 and strain rate sensitivity given in Table 4). These were complemented analytically by a comparison of calculated activation energies (shown in Figure 11) to theoretical values of activation energies associated with specific deformation mechanisms (detailed in Table 6).

Conventional creep mechanisms are not included in the following discussion. For the alloys and conditions tested, a steady state stress was never reached (with the possible exception of the RR350 alloy at 300 ^{o}C and 10^{-4}-10^{-3} per second, as shown in Figure 9) and the stress exponent (the inverse of m given in Table 4) was never less than 10, placing these experiments in the dislocation plasticity and/or power law breakdown regime [55, 74].

It is noted that since several deformation mechanisms can occur simultaneously, and their

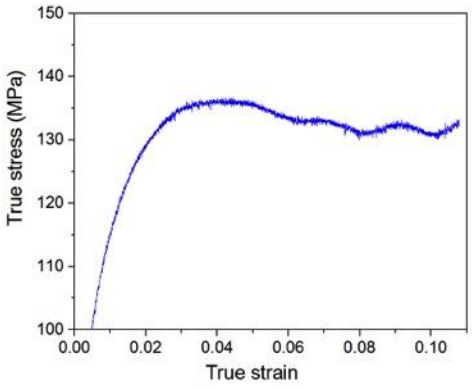

Figure 18. Stress-strain curve of RR350 compressed at 300 ºC and 10^{-4} per second, showing a distinct regime of dynamic softening after yield.

Table 5. Microstructural features observed in deformed specimens, organized by regime. Low T signifies 25 ºC and 200 ºC, low $\dot{\varepsilon}$ signifies 10^{-4} per second and 10^{-3} per second. High T signifies 250 ºC and 300 ºC, high $\dot{\varepsilon}$ signifies 10^{-1} per second and 10^{0} per second.

	Microstructural Features in Deformed 319 alloy				**Microstructural Features in Deformed RR350 alloy**			
	Testing conditions				**Testing conditions**			
	Low T, Low $\dot{\varepsilon}$	Low T, High $\dot{\varepsilon}$	High T, Low $\dot{\varepsilon}$	High T, High $\dot{\varepsilon}$	Low T, Low $\dot{\varepsilon}$	Low T, High $\dot{\varepsilon}$	High T, Low $\dot{\varepsilon}$	High T, High $\dot{\varepsilon}$
Bulk Pores or Cavities	+		+		+	+	+	+
θ and coarsened θ′			+	+				
Non-uniform θ′ Dimensions			+	+				
Bent/Shorn θ′					+	+	+	+
Triple Point / Secondary Dendrite Boundary Cracks	+	+	+	+	+	+	+ (fewer)	+
Triple Point / Secondary Dendrite Boundary Voids	+	+	+	+	+ (more)	+	+	+

Table 6. Reported activation energies for various deformation mechanisms in aluminum and aluminum alloys.

Mechanism	Activation Energy [kJ/mol]	Notes	Source
Dislocation Climb	144 [kJ/mol] < $Q_c^{\dagger}$ < 200 [kJ/mol]	Corresponds to 1-1.4x the activation energy for the diffusion of vacancies in aluminum, which is required for dislocation climb.	[43, 61]
Precipitate Deformation; Kinematic Hardening	$Q_c^{\dagger} \geq 288$ [kJ/mol]	Orowan looping leads to the elastic deformation of strengthening precipitates and is a central feature of kinematic hardening.	[61-63]
Cavity Formation	Q = 144 [kJ/mol]	Estimated as the activation energy for vacancy diffusion since vacancies must coalesce to form cavities.	[29]
Cross Slip of Dislocations	Q = 116 – 183 [kJ/mol]	The activation energy for cross slip depends on the identity of the secondary slip plane.	[64, 65]
Glide of Sub-Boundary Segments	Q = 67.5 [kJ/mol]	This is reported only at temperatures *below* 200^o C in pure aluminum, when a single slip system is active.	[66]
Glide with Solute Drag in the 319 alloy	Q = 130.4 [kJ/mol] for Mg Q = 104 [kJ/mol] for Mn	Mg and Mn have the largest and second largest misfit among solutes in the 319 alloy, respectively, and will therefore be the controlling solutes. These activation energies are based on dilute elemental diffusion in aluminum.	[29, 67]
Glide with Solute Drag in the RR350 alloy	Q = 242 [kJ/mol]	Zr has the largest misfit among solutes in the RR350 alloy by a large margin and will therefore be the controlling solute. This activation energy is based on dilute Zr's diffusion in aluminum.	[29, 67]
Dynamic Precipitate Coarsening	Q = 136 [kJ/mol]	This is based on the activation energy for the diffusion of dilute Cu in Al. Cu diffusion is required for the strengthening precipitates to coarsen. Applicable to coarsening that occurs *during* deformation.	[29]
Grain Boundary Sliding	Q = 60.2 – 84 [kJ/mol]	Various mechanisms of grain boundary sliding have been proposed, the majority of which cite the diffusion of vacancies at the grain boundary as the rate-limiting step. It can occur at room temperature [68] but is expected to be dominant only above 0.4 T_M (approximately 100 ^{o}C in Al) [69].	[68-76]
† Note:	In some cases, a corrected activation energy, Q_c, was reported [61], and is defined mathematically as: $Q_c = Q + \frac{n * R * T^2}{E} * \frac{dE}{dT}$ Where E denotes Young's modulus as a function of temperature (taken from [77]).		

contributions to mechanical response may be serial, parallel, or something intermediate, it is difficult to define a solely dominant deformation mechanism in any given regime. The objective of the following section is to examine the range of possible deformation mechanisms evidenced by each body of data (mechanical properties, microstructure, activation energies) and identify the mechanisms which appear to be dominant/rate controlling.

2.4.2. *Deformation Mechanisms*

319 alloy

Prior work by Russell and Ashby [63] and Teixeira *et al.* [62] has included a thorough analysis of the kinematic and isotropic hardening which results from the interaction of dislocations with θ′ particles in the as-aged 319 alloy at room temperature. The observed fracture and decohesion of eutectic Si and intermetallic particles between secondary dendrites in 319 alloys is well-described by Rincon *et al.* [35]. The temperature-dependent dislocation motion in the α-Al matrix along with its effects on strain hardening is reported by several authors [49, 63, 64, 78-80].

The direct study of dislocation-precipitate interaction in this family of alloys has not been extended to 200 ^{o}C in prior work. However, the empirical values of activation energy observed at 200 ^{o}C in this study (average Q_c value of ~ 250 kJ/mol, see Figure 11) correspond most closely with the theoretical activation energy for kinematic hardening (≥ 288 kJ/mol, see Table 6) [6, 49, 61]. This suggests that, so long as an adequate proportion of nanoscale θ′ precipitates are retained from the as-aged condition, the elevated temperature compressive response of the 319 alloy may be significantly influenced by kinematic hardening. It bears mentioning that the respective contributions of isotropic and kinematic hardening are functions of strain [6, 63], and that the apparent activation energy calculations in this study are based on data taken at ε_{true} = -0.05,

corresponding to the reported saturation point for kinematic hardening in these alloys (*i.e.* the strain at which the absolute contribution of kinematic hardening to total strain hardening is maximized) [62]. Above 200 ^{o}C, θ′ precipitates are substantially coarsened following the preconditioning treatment. This is accompanied by a drop in flow stress of approximately 40% between 200 ^{o}C and 250 ^{o}C (Figure 10), which suggests that precipitate strengthening becomes less effective [14]. Thus, at temperatures of 250 ^{o}C and above, other aspects of the 319 alloy's mechanical behavior may become more prominent. Because thermally activated processes are expected to have a bearing at these temperatures (T/T_m>0.5) the elevated temperature mechanical response of the 319 alloy will be discussed in terms of low strain rate behavior and high strain rate behavior.

In the low strain rate regime (10^{-4} per second and 10^{-3} per second) at 250 ^{o} C, the average Q_c value is ~ 165 kJ/mol, in agreement with the activation energy for dislocation climb (144 kJ/mol – 200 kJ/mol) reported by others [43, 61]. At 300 ^{o}C, the average Q value is ~ 135 kJ/mol, in agreement with the activation energy for dislocation glide with Mg solute drag, 130 kJ/mol. This suggests a possible transition from climb-controlled deformation at 250 ^{o}C to glide-controlled deformation at 300 ^{o}C, an inference that is also borne out in observations of the evolving microstructure of the 319 alloy (Table 7). The number density and average aspect ratio of precipitates decrease between 250 ^{o}C and 300 ^{o}C as θ′ coarsens and evolves into θ. This leads to an increased effective average spacing between dislocation obstacles, increasing the distance that a dislocation will glide relative to the distance it must climb around obstacles as it transverses a given section of microstructure [6, 40]. Additionally, dislocation climb is expected to occur more rapidly (and thus be less likely to limit the rate of deformation) at 300 ^{o}C than at 250 ^{o}C because it is facilitated by thermally activated processes of vacancy diffusion and cross slip. Prior reports

suggest that Mg diffusion plays a prominent role in the deformation of the 319 alloy at elevated temperatures [35], and solute drag may partially explain why the activation energy of the 319 alloy is substantially greater than that of the RR350 alloy across all conditions tested [81].

In the high strain rate regime (10^{-1} per second and 10^{0} per second), the deformation mechanisms in the 319 alloy are less determinate. At 250 ^{o}C, the average Q value of ~ 140 kJ/mol (Figure 11) indicates that dislocation cross slip, cavity formation, and dynamic coarsening are possible rate determining mechanisms (Table 6). Given that cross slip has been repeatedly observed for Al at this temperature [49, 63, 64, 78-80] while there was no microstructural evidence of cavitation or dynamic coarsening (Table 5, Figure 12), cross slip seems to be the most plausible rate controlling deformation mechanism. At 300 ^{o}C, the average Q value in the high strain rate regime is ~ 100 kJ/mol (Figure 11), which is consistent with the theoretical value for dislocation glide with solute drag of Mn (104 kJ/mol, Table 6). Taken together, the results suggest that dislocation glide and solute drag are important aspects of compressive response for the preconditioned 319 alloy over a broad range of strain rates at 300 ^{o}C.

RR350 alloy

Observations suggest that the interaction between dislocations and θ′ particles in the RR350 alloy is dependent on grain orientation. The shear banding of θ′ occurred almost exclusively in grains with a <100> type axis nearly parallel with the compressive axis, *i.e.* those with "vertical" and "horizontal" precipitates in the observation plane (*e.g.* the grain on the left in Figure 15). These grains have a high Schmid factor for their (1 1 1) type planes, as these planes are nearly aligned with the 45^{o} direction of maximum shear. By extension, these grains have lower Taylor factors than other grains and will undergo greater deformation for a given macroscopic stress (*i.e.* they are "soft" grains compared to their neighbors) [55, 82, 83].

In terms of kinematic analysis, the activation energy of the RR350 alloy is one third to one half of that of the 319 alloy under all testing conditions and is relatively temperature independent. At room temperature, a combination of kinematic and isotropic hardening is likely the dominant deformation response, as in the 319 alloy [6, 41,42]. Because the strengthening precipitates in the RR350 alloy are larger and more widely spaced, it is reasonable that this alloy yields at a lower stress (due to a lower number density of dislocation obstacles). At elevated temperatures, activation energy calculations suggest that two rate-limiting deformation mechanisms are possible in the RR350 alloy, as described below.

For low strain rates (10^{-4} per second and 10^{-3} per second), at temperatures of 200 ^{o}C and 250 ^{o}C, the empirical Q values of 94 kJ/mol – 121 kJ/mol are reasonably consistent with cross slip (Table 6), which has been observed for Al in this regime [49, 63, 64, 78-80]. For all other elevated temperature tests, the empirical Q values are most similar to that of grain boundary controlled deformation (sub-boundary glide is overlooked because multiple slip systems are active [66]). Grain boundary sliding under the conditions tested is also empirically supported. In prior work, grain boundary sliding has been observed in fine-grained pure Al at similar temperatures, resulting in a similar strain rate sensitivity and activation energy [76]. In the current work, it was observed that the deformation behavior of individual grains was very dependent on their orientation. Unequal strain between neighboring grains can be accommodated by decohesion of grain boundaries or the formation of voids at triple points [55], and both features are observed in the post-deformation microstructure of the RR350 alloy under all conditions. Figure 16 shows two examples of these microstructural features, one resulting from the lowest temperature and strain rate tested, one resulting from the highest temperature and strain rate tested. The extensive contribution of grain boundary related mechanisms to the deformation of the RR350 alloy above

200 ºC may indicate that the cohesive strength of the grain bulk, which is retained at these temperatures due to the thermal stability of its strengthening precipitates[14], is in excess of the adhesive strength of grain boundaries. It was observed that decohesion tended not to occur at points along the grain boundary populated by intermetallic particles. This observation suggests that these intermetallics inhibit grain boundary diffusion of vacancies and/or the separation of grains.

2.4.3. *Alloy Comparison*

Rate Determining Deformation Mechanisms

The inferred rate determining deformation mechanisms are summarized and compared for the two alloys in Table 7. These mechanisms have theoretical activation energies that are consistent with empirically determined Q values (Figure 11 and Table 6) and are corroborated by microstructural analysis, measured mechanical properties, and comparison to prior work. At room temperature, prior work suggests that both alloys deform by a similar mechanism. Furthermore, thermally activated cross slip of dislocations likely contributes to the plasticity of each alloy at intermediate temperatures. The notable difference between the 319 and RR350 alloys is in their elevated temperature deformation mechanisms. The evidence suggests that the 319 alloy may deform primarily *via* serial processes of solute drag and dislocation climb in its thermally softened dendritic bulk, and the RR350 alloy may deform primarily by grain boundary driven mechanisms due to an increased thermal stability of θ′ precipitates and higher strength in its grain bulk.

2.4.4. *Microstructure*

Accommodation of strain by void formation and particle cracking at grain boundaries/secondary dendrite boundaries appears to be the initial response of both alloys during compression (in

Table 7. Inferred rate limiting deformation mechanisms in each alloy, consistent with empirical activation energies, microstructural observation, mechanical properties, and prior work.

	319			
	Strain rate (per second)			
	10^{-4}	10^{-3}	10^{-1}	10^{0}
300 °C	Dislocation Climb and Solute Drag (with the latter becoming more prominent as temperature increases)			
250 °C			Cross slip of dislocations	
200 °C	Kinematic and isotropic hardening as described in [6, 41,42]			
25 °C				

	RR350			
	Strain rate (per second)			
	10^{-4}	10^{-3}	10^{-1}	10^{0}
300 °C	Grain boundary sliding			
250 °C	Cross slip of dislocations			
200 °C				
25 °C	Kinematic and isotropic hardening as described in [6, 41,42]			

agreement with [84], Figures 12b and 16b). These phenomena were consistent features of the deformed microstructure while the compressive response varied dramatically depending on alloy and test conditions. Therefore, it is apparent that this aspect of deformation does not play a significant role in determining the flow stress or work hardening of either alloy (although grain boundary related mechanisms contribute significantly to the activation energy of the RR350 alloy at elevated temperature). Thus, the deformation response of the grain bulk is expected to be the dominant contributor to the divergence of their mechanical behavior.

At high temperatures, the most significant difference between the two alloys is the nature of the θ/θ′ precipitates in the bulk. In the 319 alloy, the morphology, distribution, and dimensions of the strengthening precipitates become less consistent with increasing temperature. Cu is absorbed from θ′ precipitates by coarsening θ particles whose high energy, incoherent interfaces lead to the rapid growth of blocky particles at the expense of finely dispersed, disc shaped θ′ precipitates [6, 7]. This means that the strengthening effect of θ particles decreases while the amount of Cu "available" for the more effective θ′ precipitate phase is diminished. In contrast, the precipitates in the RR350 alloy retain their coherent and semi-coherent interfaces with the matrix up to 300 ^{o}C, as evidenced by strong dislocation interactions (Figures 14 and 15).

The as-aged microstructure of the RR350 alloy is similar to that of the more widely used forged aluminum alloy 2219, although there is some difference in their composition (See [1, 85] and Table 1). Trends in the yield strength of 2219 [1] suggest that its strengthening precipitates are thermally stable to a temperature between 250 ^{o}C and 300 ^{o}C, as compared to at least 350^{o}C in RR350 [14].

2.4.5. *Flow Stress*

Trends in the 319 alloy's high temperature flow stress seem to be dictated by a decrease in the prevalence of effective strengthening precipitates. This alloy's decrease in flow stress as a function of temperature is non-linear. It drops off sharply at testing temperatures greater than 200 ^{o}C (Figure 10). Trends in the high temperature flow stress of the RR350 alloy seem to be dictated by thermally aided glide and climb of dislocations. The decrease in flow stress with temperature is somewhat linear for the RR350 alloy at all strain rates (Figure 10). This phenomenon has a dramatic effect on high temperature mechanical properties. The 319 alloy is approximately 25% stronger than the RR350 alloy when they are compared in the as-aged condition (as measured by flow stress averaged across strain rates, Figure 10). However, the RR350 alloy is approximately 100% stronger than the 319 alloy when they are both preconditioned and compressed at 300 ^{o}C.

2.4.6. *Strain Rate Sensitivity*

Strain rate sensitivity is similar for the two alloys at 25 ^{o}C and 200 ^{o}C and is greater for the 319 alloy at 250 ^{o}C and 300 ^{o}C, an effect of microstructural instability in the 319 alloy. The increase of strain rate sensitivity with temperature is typically ascribed to evolving strain hardening mechanisms [36, 86]. In the as-aged condition, kinematic hardening is expected to contribute substantially to flow stress in the 319 alloy [6, 62]. At elevated temperatures, the number density and aspect ratio of dislocation obstacles is reduced, which decreases the extent of strain hardening and leads to other deformation mechanisms becoming dominant in the 319 alloy. In the RR350 alloy, the strain hardening mechanisms are more consistent throughout testing conditions due to its thermally stable microstructure, resulting in a lower variation of strain rate sensitivity.

2.4.7. *Activation Energy*

The 319 alloy generally demonstrates higher activation energy for deformation than does the RR350 alloy. Two factors may contribute to this difference in activation energy values. First, it is likely that grain boundary related deformation mechanisms are much more active in the RR350 alloy, and these are associated with a lower activation energy than most deformation mechanisms acting in the grain bulk (see Table 6). Second, a greater amount of solute in solid solution is associated with increased activation energy for deformation in similar alloys, due to solute drag effects [81]. The 319 alloy tested in this study is more highly alloyed than the RR350 alloy (see Table 1) and has a greater concentration of solute atoms in its α-Al matrix [7, 87].

The Q values of the RR350 alloy appear to be primarily dependent on strain rate, while Q values for the 319 alloy depend on both strain rate and testing temperature (with moderately greater dependence on the latter, Figure 11).[1] The temperature dependence of activation energy in the 319 alloy is related to the evolving morphology of its precipitates. As observed by Shi and Chen [49], a decrease in the ability of precipitates to pin dislocations corresponds to a decreased activation energy. Thus, the formation of increasingly coarse, globular precipitates at the expense of finely dispersed, disc-shaped precipitates may contribute to a decrease in activation energy with temperature for the 319 alloy. In comparison, the observed activation energy in the RR350 alloy is relatively independent of temperature, which suggests that the dislocation-pinning ability of its strengthening precipitates is maintained up to 300 ^{o}C.

[1] Compression can be characterized as isothermal, adiabatic, or intermediate between the two depending on strain rate [28]. Sample heating during compression was not accounted for in this study, but it is possible that this effect contributed to strain rate dependence of results.

2.4.8. *Plastic Relaxation Mechanisms*

In terms of plastic relaxation mechanisms, the two alloys differ substantially. The trends in boundary misorientation angles shown in Figure 17 as well as the fact that the RR350 alloy exhibits dynamic softening when compressed at 300 ^{o}C and 10^{-4} per second (Figure 9) suggest that the RR350 alloy undergoes dynamic recovery and recrystallization at low strain rates and elevated temperatures, while the 319 alloy does not progress beyond partial dynamic recovery. Additional EBSD analysis would be required to determine the precise threshold for a change in plastic relaxation mechanisms in the RR350 alloy.

2.5. Conclusions

This study compares the compressive response of two precipitate strengthened cast aluminum alloys, 319 and RR350, at a range of temperatures and strain rates. It quantifies the differences in their mechanical behavior and relates these differences to the thermally driven evolution of their microstructures. The principal conclusions of this study are as follows:

- Microstructural analysis and activation energy calculations suggest that localized dislocation-precipitate interaction observed in prior work for Al-Si-Cu alloys at room temperature might also be a significant aspect of compressive response in the 319 alloy up to 200 ^{o}C.
- The effectiveness of strengthening precipitates in the 319 alloy decreases with prolonged exposure to temperatures above 200 ^{o}C. Above 200 ^{o}C, θ' particles gradually coarsen and transform to incoherent θ particles. As this transformation progresses, the number density and aspect ratio of strengthening precipitates decreases, leading to increased contribution of mechanisms such as cross slip, dislocation climb, and solute drag to the compressive response of the 319 alloy.

- The effectiveness of strengthening precipitates in the RR350 alloy is maintained up to 300 ^{o}C. In comparison to the 319 alloy, coarsening of θ′ particles is substantially reduced and evolution of θ′ to θ is not observed. The stability of the θ′ strengthening precipitates leads to significantly improved elevated temperature mechanical properties for RR350 compared to the 319 alloy.
- Observed plastic relaxation mechanisms in the RR350 alloy at elevated temperature include dynamic recovery and recrystallization, while the 319 alloy did not progress beyond partial dynamic recovery.
- Due to the relatively high strength of the grain bulk in the RR350 alloy, grain boundary sliding may contribute significantly to deformation at temperatures of 250 ^{o}C and above for this alloy.

2.6. Chapter 2 Appendix

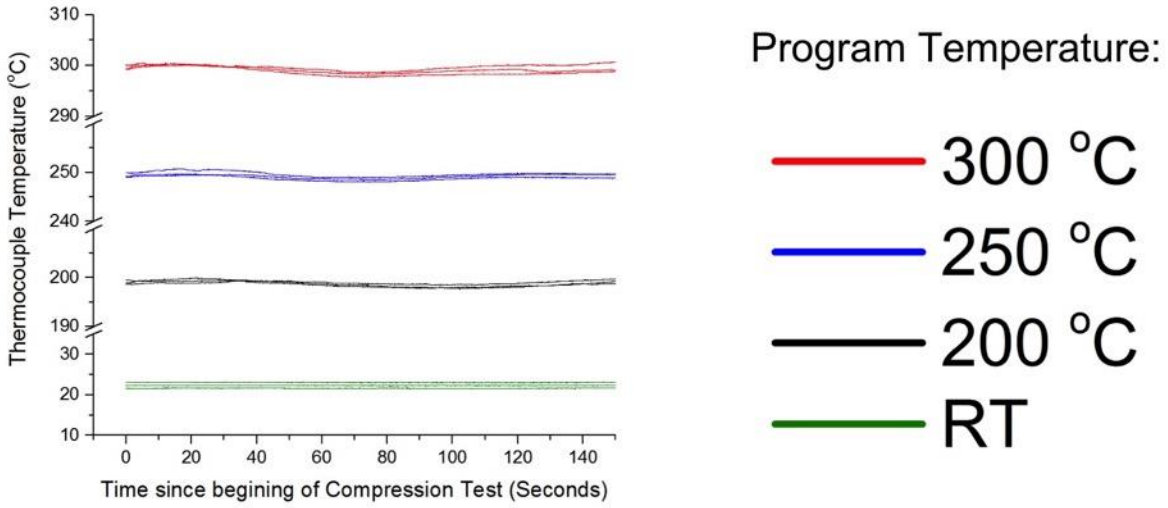

Figure 19. Specimen temperature vs. program temperature for RR350 during compression testing at 10^{-3} per second. There are three lines for each test because three thermocouples were used to record specimen temperature

Chapter 3

Onset of θ′ to θ Phase Transformation in Al-Cu alloys

This chapter is revised based on a drafted journal article with Patrick Shower as lead author:

P. Shower, J. Morris, D. Shin, L. Allard, B. Radhakrishnan, A. Shyam, Onset of θ′ to θ Phase Transformation in Al-Cu alloys (In Review) (2019).

My primary contributions to this paper include (i) objectives and design of study (ii) thermodynamic analysis (iii) developing and running phase field simulations for θ′ vs θ competition (iv) literature review (v) most of the writing.

Abstract

The θ′ → θ phase transformation that occurs during overaging in Al-Cu alloys is detrimental for their mechanical properties. Experiments suggest that the onset of this transformation is dependent on the temperature and duration of thermal exposure, but the microstructural conditions leading to this transformation are still unclear. In this study, we predict the critical conditions associated with the onset of θ′ → θ phase transformation using thermodynamic analysis. To test the predicted critical conditions, we compare against both new and previously reported microstructural observations, and also test the predictions using phase field modeling. This multi-pronged approach suggests that the tendency of a θ′ particle to transform into the θ phase depends primarily on temperature, particle size, and particle aspect ratio. We define a "critical" aspect ratio below which θ′ → θ phase transformation becomes favored and show how this critical aspect ratio increases with both temperature and particle volume. We illustrate, with this approach, the intimate link between phase stability and morphological stability/coarsening resistance for θ′ precipitates in Al-Cu alloys.

3.1. Introduction

The transformation of metastable, strengthening θ′ precipitates into the equilibrium θ phase is detrimental for the mechanical properties of Al-Cu alloys [6, 7, 14, 34, 42]. The intermetallic θ (body centered tetragonal Al_2Cu) is typically observed in the bulk microstructure of Al-Cu alloys that have been overaged [1]. In the earlier stages of aging, supersaturated Cu in the grain bulk commonly forms a series of metastable phases (GP Zones, θ″, θ′) which provide precipitate strengthening to naturally and artificially aged alloys [7, 30, 88]. These metastable phases have greater coherency with the α-Al matrix than the θ phase [89]. As a result, they have reduced interfacial energy and critical nucleus sizes relative to the θ phase, and nucleate more readily on the defects present within grains and dendrites [3, 30]. Given adequate time and temperature [42], the θ phase will generally nucleate on these metastable particles [90-92] and coarsen at their expense [42, 92]. However, the factors that determine this "adequate time and temperature" threshold are yet unknown. The objective of this study is to quantify the specific microstructural conditions that lead to the θ′ → θ phase transformation.

The structure, thermodynamics, and morphological evolution of the Al_2Cu phases have been well studied [1, 3, 6, 7, 35, 37, 43, 49, 88-90, 93-121]. There is an established consensus that the total free energy of the Al-Cu system is reduced in the progression of GP I → θ″ → θ′ → θ (the entire sequence may or may not be observed – the initial phase to nucleate depends on aging temperature) [30]. Many studies have found θ″ or θ′ in peak-aged microstructures and θ in overaged microstructures of the same alloy [37, 101, 104, 113, 122], but fewer studies have captured or analyzed the actual phase transition(s) [90, 91]. This is partly due to the fact that these structural transitions are rapid and sometimes ill-defined [123, 124]. Additionally, most aluminum alloys strengthened by θ″ or θ′ are designed for use at low homologous temperatures (T/T_{Melt} <

0.5) [1]. Under these conditions, there is reduced risk of the strengthening precipitates transforming into the equilibrium θ phase during service, and an explicit definition of the time/temperature threshold for θ′ → θ transformation is not critical. It is generally understood that θ′ → θ transformation can be mitigated if sustained service temperatures do not exceed 225 °C [1, 14, 35, 36], and simply avoiding this threshold for phase transformation through component design has proven adequate [2]. First-principles thermodynamic calculations have suggested that the bulk free energy of θ′ is lower than that of θ at low temperatures, but θ becomes the equilibrium phase at higher temperatures (above ~200 °C) due to entropic stabilization [89] [125]). This offers a potential explanation for the observed phase stability of θ′.

However, the kinetics of the θ′ → θ transformation can be substantially reduced in particular alloys, as shown by recent work [14, 126]. For example, Al-Cu-Mn-Zr alloys (termed *ACMZ alloys* hereafter) are strengthened by θ′ precipitates that do not transform during extended thermal exposure at 350 °C [14]. Given these observations, it is apparent that the threshold for θ′ → θ transformation is not simply fixed in terms of temperature [14]. This raises questions about what, precisely, determines the onset of θ′ → θ transformation, and what could be done to prevent or delay that transformation at elevated temperatures. The latter question is a subject of several recent studies [117-119]. In this chapter, we address the former question using multiple, complementary approaches.

We attempt to isolate the critical conditions for θ′ → θ transformation using an analytical approach, by collecting experimental observations, and by explicitly simulating the nucleation of θ particles on pre-existing θ′ particles in a phase field simulation. In Section 3.2 we present an analytic, thermodynamic approach examining the nature of θ′ → θ transformation, to determine the conditions under which there is a net driving force for a θ′ particle to transform into the θ phase.

We introduce a "map" indicating stability of the θ′ phase, as a function of both volume and aspect ratio. In Section 3.3, we integrate new and existing data about what morphologies of θ′ and θ have been observed at various temperatures, and compare them to the map of stability introduced in Section 3.2. This comparison highlights a small but consistent discrepancy between experiments and the analytic approach. In the phase field approach, presented in Section 3.4, θ nuclei are introduced onto a virtual θ′ precipitate under a range of conditions to evaluate whether or not the nuclei are stable and tend to grow at the expense of metastable θ′ particles. The phase field results offer an explanation for the discrepancy between thermodynamic analysis and experiment. Each of these approaches has advantages and limitations. In Section 3.5 we discuss what the combined results might indicate about the nature of θ′ → θ transformation, the limitations of the present methods, and how present conclusions relate to prior work. The use of multiple approaches to study θ′ → θ transformation helps us conclude that the size and aspect ratio of a θ′ particle are the primary factors determining its stability against phase transformation at a given temperature. Therefore, the coarsening resistance of θ′ precipitates is key to delaying or preventing the onset of θ′ → θ transformation during overaging.

3.2. Analytical Approach: Predicting θ′ → θ Transformation with a Thermodynamic Driving Force Criterion

To begin our investigation of the θ′ → θ transformation, we consider the thermodynamics of each phase. Theoretically, the phase transformation can only proceed if there is a driving force for it to do so. Whereas prior work has analyzed the bulk free energy of the θ′ and θ phases [89][125], we also account for interfacial energy and lattice strain energy. This allows the total free energy associated specific particle morphologies of each phase to be compared. This comparison reveals that the thermodynamic driving force for θ′ → θ transformation depends strongly on particle size

and aspect ratio, and not solely on temperature.

3.2.1. *Calculating the Driving Force for θ′ → θ Transformation*

The analytical approach used to determine the critical condition for θ′ → θ transformation is based on the assumption that this transformation will tend to occur if it reduces the total free energy of the microstructure. Here, we define "total free energy" using the following equation:

$$E_{Tot} = E_{Vol} + E_{Int} + E_{Strain} \quad (5)$$

Here, E_{Vol} is the volumetric Gibbs free energy of formation of a particle, E_{Int} is the interfacial energy of a particle, and E_{Strain} is the elastic energy associated with coherency strains in the bulk of the particle and the matrix arising from lattice misfit. Each of these terms and their calculations are discussed below.

E_{Vol}, the volumetric Gibbs free energy of formation of a particle, is dependent on temperature and the particle's volume (Eq. 6).

$$E_{Vol} = V_{Particle} \cdot \Delta G_{form}(T) \quad (6)$$

Where $V_{Particle}$ is the particle volume and $\Delta G_{form}(T)$ is the Gibbs free energy of formation of a phase as a function of temperature, relative to pure Al at 25 °C, normalized by unit volume (in terms of nm^3 in this study). Values of $\Delta G_{form}(T)$ were taken from the TCAL3 database as implemented in Thermo-Calc and are tabulated in Table 1, along with μ, the temperature-corrected shear modulus [77].

At each temperature listed in Table 8, ΔG_{form} is lower for θ than for θ′, meaning that θ is the predicted equilibrium phase. The difference between $\Delta G_{form,\theta}$ and $\Delta G_{form,\theta'}$ is the driving force that leads to θ′ → θ transformation. The driving force for θ′ → θ transformation has been

Table 8. Thermodynamic parameters used in the analytical approach.

Temp [°C]	μ [meV/nm^3]	$\Delta G_{form,\theta}$ [meV/nm^3]	$\Delta G_{form,\theta'}$ [meV/nm^3]
200	$1.41 \cdot 10^5$	$-2.08 \cdot 10^4$	$-1.94 \cdot 10^4$
250	$1.36 \cdot 10^5$	$-2.22 \cdot 10^4$	$-2.06 \cdot 10^4$
300	$1.31 \cdot 10^5$	$-2.37 \cdot 10^4$	$-2.19 \cdot 10^4$
350	$1.26 \cdot 10^5$	$-2.52 \cdot 10^4$	$-2.33 \cdot 10^4$
400	$1.21 \cdot 10^5$	$-2.69 \cdot 10^4$	$-2.48 \cdot 10^4$

investigated by Wolverton *et al*. who used Density Functional Theory with finite temperature considerations to show that such a transformation is increasingly favored at elevated temperatures [125]. They reason that this is due to vibrational entropy terms, which favor the θ phase and have a contribution to free energy that is proportional to absolute temperature. In the present work, we find the temperature-dependent bulk free energies of the θ′ and θ phases using the TCAL3 database and come to a similar conclusion: the driving force for θ′ → θ transformation increases almost linearly with temperature.

This driving force for θ formation is opposed by E_{Int} and E_{Strain} terms which both favor the more coherent θ′ phase. E_{Int} is the total interfacial energy of a particle, dependent on the particle's volume, aspect ratio, and three-dimensional morphology (Eq. 7).

$$E_{Int} = \sum \gamma_i \cdot A_i \tag{7}$$

Where γ_i is excess free energy per unit area associated with stretched and broken bonds (structural and chemical energy, respectively) that occur at a given type of interface between the particle and the α-Al matrix, and A_i is the area of each type of interface. A_i is found using simple geometric assumptions: that the θ′ particle is either cylindrical or prismatic, and that the θ particle is an oblate, or "squashed" spheroid. The surface area of an oblate spheroid is given in the following formula [30].

$$A_{Ob.\ Sph.} = \frac{\pi}{2} \cdot d^2 + \frac{\pi}{4} \cdot \frac{t^2}{e} \cdot \ln\left(\frac{1+e}{1-e}\right) \tag{8}$$

In Equation 8, d is the diameter of the particle measured in the equatorial direction, t is the thickness of the particle measured along the polar axis, and e is the "ellipticity" of the particle, defined as:

$$e \equiv \sqrt{1 - \left(\frac{t}{d}\right)^2} \tag{9}$$

γ_i values used in this study are given in Table 9, and are assumed to be independent of temperature. E_{Strain} captures the elastic strain energy in the bulk of both the particle and the matrix required for the two to geometrically conform [30]. Various approaches have been used to calculate E_{Strain} [127-131]. In this study, we use Nabarro's formulation [131] specifically tailored to spheroids of variable aspect ratio (Eq. 10). It assumes an incompressible inclusion, which is reasonable since the Young's moduli of θ and θ′ particles are approximately twice that of α-Al [100, 132, 133].

$$E_{Strain} = \frac{2}{3}\mu \cdot \Delta^2 \cdot V_{Particle} \cdot f\left(\frac{d}{t}\right) \tag{10}$$

In Equation 10, μ is the shear modulus of the matrix (listed in Table 8), Δ is the volume misfit of the particle, and $f(d/t)$ is a geometric function describing the way that the inclusion shape impacts the total energy associated with the surrounding strain field. $f(d/t)$ is defined mathematically by Nabarro [131]. Note that E_{Strain} is minimized for a disk-shaped inclusion, and that a balance between E_{Strain} and E_{Int} decides the equilibrium aspect ratio of θ′ and θ precipitates [30]. We calculated the volume misfit (Δ) of the θ phase within the α-Al matrix by comparing the volume occupied by 12 atoms of α-Al (*i.e.* the volume of 3 unit cells) and the volume occupied by 12 atoms of θ (8 Al, 4 Cu atoms within 2 unit cells). This approach predicts a volume misfit of -9.93% for a θ particle [30].

With all the thermodynamic terms in Equation 5 defined, the total free energy associated with each type of particle can be assessed. Specifically, we compare E_{Tot} for θ′ and θ particles with the same

Table 9. Interfacial energy values used in the analytical approach. θ′ values were calculated using DFT calculations (DFT supercell description elsewhere [14, 117, 118]). Stress free interfacial energy values for the θ phase were calculated by Kokotin and Hecht using molecular dynamics with embedded atom method (EAM) potential [41].

Phase	Type of Interface	Lattice Correspondence	$\gamma\ \left[\frac{mJ}{m^2}\right]$	$\gamma\ \left[\frac{meV}{nm^2}\right]$
θ′	Coherent	$(1\ 0\ 0)_{\theta'}::(1\ 0\ 0)_{\alpha}$	258	1610
	Semi-Coherent	$(0\ 1\ 0)_{\theta'}::(0\ 1\ 0)_{\alpha}$	527	3289
θ	Incoherent	Average over all possible	456	2846

number of atoms and the same aspect ratio. As a θ′ particle in the Al-Cu microstructure evolves, this comparison should indicate the point at which there is a driving force for that particle to take on θ crystallography. This approach is based on the mechanism reported by Laird and Aaronson for the nucleation of "Group I" θ particles on θ′, in which "the θ plate 'bodily' replaces its θ′ predecessor" [90]. This transformation mechanism was also observed more recently using transmission x-ray microscopy [92].

To generate free energy data, we first select a temperature and a particle volume for θ′. In order to determine the dependence of E_{Tot} on particle morphology, we then solve Eq. 5 for a range of particle aspect ratios (Eq. 11).

$$Aspect\ Ratio \equiv \frac{d}{t} \tag{11}$$

E_{Vol} is invariant because the particle volume is constant, E_{Int} and $E_{Lattice\ Strain}$ change as the geometric terms in their respective formulas are altered. This approach is similar to that recently taken by Liu and coworkers to compare the thermodynamics of θ′′ and θ′ particles [134].

A sample calculation is plotted in Figure 20, for a θ′ particle at 300 °C with a typical as-aged volume [119] and a disk-shaped morphology. To generate an analogous free energy curve for θ, its volume is calculated based on the premise that the θ particle contains the same number of atoms as the θ′ particle it is being compared to (*i.e.* that the quantity of Cu atoms is conserved). This requires a minor adjustment in particle volume, because the unit cell of θ is approximately 5.5% more dense than that of θ′, in terms of atoms per nm^3 [30]. With the newly calculated volume, the procedure above is repeated and another E_{Tot} curve is generated, also plotted in Figure 20.

We derive our analytical results from E_{Tot} curves like those shown in Figure 20. The equilibrium aspect ratio of each phase corresponds to the minima in the free energy curves (2.0 for θ′ and 4.6

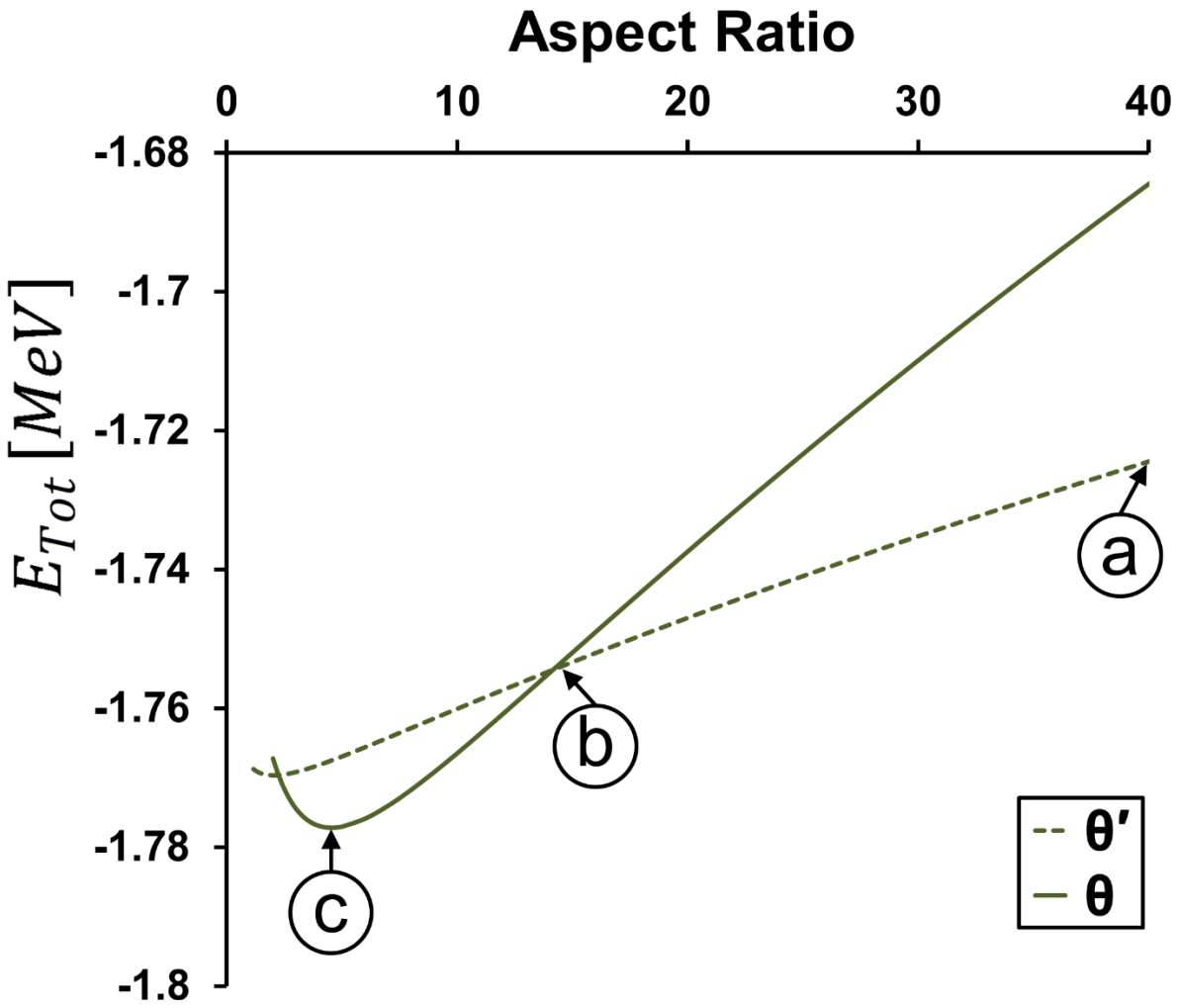

Figure 20. Comparative plot of $\boldsymbol{E_{Tot}}$ for θ′ and θ particles at 300 °C, based on the median volume of a θ′ particle observed in a 319 alloy after T7 aging (approximately 82,000 nm^3 [119]). Points "a", "b", and "c" are labeled to aid in the discussion of the relative stability of phases.

for θ). By comparing the curves, we posit that the relative stability of a θ′ particle as function of morphology can be determined. Consider an as-aged θ′ particle with a typical aspect ratio of 40 (point "a"). At this high aspect ratio, there is no driving force for the particle to transform into a θ particle with the same aspect ratio (at 300°C). During over-aging, the aspect ratio of the θ′ particle will tend to decrease, reducing E_{Tot} and approaching the equilibrium value [37, 100]. As aspect ratio decreases, the values of E_{Tot} for each phase become more and more similar. At point "b", there is a crossover and the θ phase becomes more stable. Thus, for aspect ratios below point "b", there will be a driving force for θ′ → θ transformation. Once the θ phase forms, it can minimize E_{Tot} by evolving towards its own equilibrium aspect ratio at point "c",.

The E_{Tot} curves also offer information about multi-particle interaction. If two particles of the same volume are present, a θ′ particle at point "a" and a θ particle at point "c", the θ particle will be more stable, and will tend to grow at the expense of the θ′ particle. Furthermore, a θ particle at point "c" with an equilibrium aspect ratio has a lower free energy than any θ′ particle of equivalent size, regardless of the aspect ratio of θ′. Therefore it is expected that once an initial θ particle is established, microstructural evolution in its vicinity becomes controlled by a coarsening mechanism as θ particles grow at the expense of nearby θ′ particles. This is consistent with prior microstructural observations [30, 42, 92]. For this reason, the initial formation of a θ particle is a watershed event in terms of microstructural evolution. In an as-aged Al-Cu microstructure with no θ particles present, the driving force for initial θ nucleation and growth will depend upon the aspect ratio value of one or more θ′ particles reaching point "b", corresponding to a "critical aspect ratio" at which E_{Tot} is equivalent for both phases. Eqs. 5-11 predict that the critical aspect ratio will be a function of temperature and particle volume. For the temperature (300 °C) and particle volume (82,000 nm^3, the median particle volume in cast aluminum alloy 319 aged to T7 condition [119])

used to calculate the curves shown in Figure 20, the critical aspect ratio is predicted to be 14. This critical aspect ratio can be calculated for any temperature and particle size of interest. Modifications to particle geometry or other parameters of interest can also be accounted for. By calculating the critical aspect ratio as a function of particle size for a series of temperatures, an analytical phase stability map was generated, as described in Section 3.2.2 below.

3.2.2. *Using Driving Force to Predict the Stability of θ′ as a Function of Morphology*

The analytical procedure described in Section 3.2.1 predicts whether a θ′ particle will be stable or have a thermodynamic driving force to transform into the θ phase, depending on temperature and the particle's morphology. As shown in Figure 20, the analysis suggests that above a critical aspect ratio, θ′ is stabilized, while below that critical aspect ratio, θ is stabilized. This critical aspect ratio was calculated at temperatures between 200 °C and 400 °C as a function of particle volume, and the result is plotted in Figure 21. Figure 21a illustrates how critical aspect ratio was calculated for a range of particle volumes to produce a critical aspect ratio vs. particle volume curve at 300 °C. Figure 21b shows how this critical aspect ratio calculation varies as a function of temperature.

To interpret the plot in Figure 21b, consider a θ′ particle with a constant volume of 10,000 nm^3, which falls along the y-axis. If the θ′ particle has an aspect ratio of 20, Figure 21b suggests that it is stable against phase transformation at 400 °C. However, if its aspect ratio decreased to a value of 10 or below, that particle would have a thermodynamic driving force to evolve into the θ phase at 400 °C. If the temperature were 300 °C, the θ′ particle would retain its stability until the aspect ratio decreased to a value of 5 or below. Note that this plot does not account for a scenario where a nearby θ particle is already present, in which case the θ′ particle may be consumed by coarsening regardless of its aspect ratio.

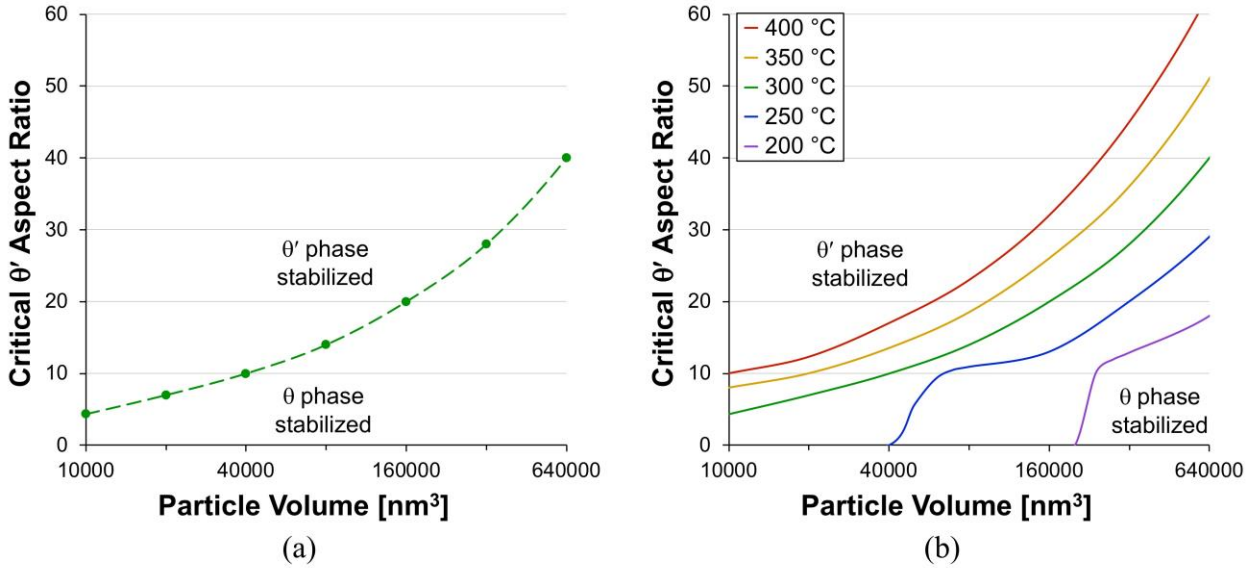

Figure 21. (a) The critical aspect ratio of θ′ (below which thermodynamic analysis predicts θ′ → θ transformation will become favored and above which θ′ is stabilized) was calculated for several particle volumes at 300 °C and a trendline was drawn. The critical aspect ratio increases with particle volume, suggesting that smaller θ′ particles are more stabilized against phase transformation into θ. Note the logarithmic scale of the x-axis (b) The procedure described for (a) was repeated for temperatures between 200 °C and 400 °C to create an analytical phase stability map. The critical aspect ratio of θ′ increases with temperature, suggesting that θ′ particles are more stabilized against phase transformation into θ at lower temperatures.

The analytical results shown in Figure 21 imply that the critical aspect ratio for θ′ → θ transformation is a strong function of temperature and particle size. Moreover, they suggest that *phase stability is tied to morphological stability in the Al-Cu system*. If a θ′ particle coarsens, or reduces its aspect ratio towards the equilibrium value, it is more likely to evolve into θ. During the coarsening process, larger particles tend to grow in volume and all particles tend decrease in aspect ratio [37]. Therefore, stabilizing the θ′ phase at any given temperature requires the coarsening process to be inhibited.

Figure 21 also captures noteworthy temperature effects. First, that the particle volume – aspect ratio regime for θ′ stability is significantly reduced as temperature increases from 200 °C to 400 °C. In other words, there is much more allowance for θ′ particles to coarsen at 200 °C without the risk of θ′ → θ transformation. For temperatures of 200 °C and 250 °C, the analysis also predicts that there is a "critical particle size", below which any aspect ratio of θ′ will be stable. This is consistent with the presence of very small, low aspect ratio θ′ particles observed by Bourgeois *et al.* after aging at 200 °C [109].

3.3. Experimental Approach: Comparing Analytical Phase Transformation Criteria to Microstructural Observations

In the experimental approach, we attempt to answer a simple question: what morphologies of θ′ and θ particles are empirically observed? If there is a clear boundary between θ′ morphology and θ morphology, that would support the analytical results which suggest that the stability of either phase is tied to the morphology of individual particles.

3.3.1. *Experimental Methods*

To evaluate the analytical results, we collected data on θ′ and θ morphology from several studies in the literature. Additionally, we examined precipitate morphology in an RR350 alloy (Al-5Cu-Ni, composition and heat treatment described elsewhere [42]) and a 206 alloy (Al-5Cu-Mg, composition and heat treatment described elsewhere [7]). Scanning electron microscopy (SEM) and aberration-corrected high angle scanning tunneling electron microscopy (STEM) were performed using standard methods, described previously [6, 7, 14]. The data collected for each precipitate included its observable dimensions and the temperature it was exposed to during aging or overaging. To calculate the volume and aspect ratio of each particle, it was assumed that the full diameter of the particle was visible in the micrograph [135], and that the particle morphology was either a disk (in the case of θ′) or an oblate spheroid (in the case θ). This allowed each particle to be plotted on a stability map analogous to Figure 21b. Because the thickness of θ′ particles (on the order of nm's) is uncertain in micrographs, error bars were applied to each data point. Low magnification micrographs have been reported to artificially increase the measured thickness of disk-shaped precipitates, in some cases doubling the thickness values measured at a high magnification [7, 99]. This phenomenon is inherent to TEM and SEM imaging, and was also observed in micrographs taken for the present study. Therefore, the error bars applied to the mostly low-magnification SEM and AC-STEM data account for an uncertainty of up to 50%.

3.3.2. *Relevant Observations from Prior Work*

To inform our interpretation of quantitative results from the literature, we note general observations that have been made on θ′ and θ evolution. When θ′ particles nucleate during aging, they undergo rapid radial growth and relatively sluggish thickening until excess Cu in the matrix

is consumed [30, 115]. During this process, the mean aspect ratio of θ′ is increasing and the growth kinetics are interface-controlled [37, 92, 113]. The peak-aged condition approximately corresponds to the time of maximum median aspect ratio of θ′. After the point of peak-aging, median aspect ratio begins to decrease [37, 92, 113]. Larger particles continue to grow while smaller particles shrink. Thickening continues at a constant pace, and particles begin to approach their equilibrium aspect ratio determined by a Wulff plot (reported as anywhere between 2 and 5 [37, 100]). At some point, generally after tens to hundreds of hours of thermal exposure at 200 °C or above, the θ phase nucleates in the bulk of the Al-Cu microstructure [37, 101, 104, 113, 122]. Aaronson and Laird [90], as well as Hornbogen [91], were able to capture this nucleation event with TEM, and reported that the nucleation of θ occurred on the semi-coherent interface of θ′. As thermal exposure continues, θ particles rapidly coarsen [7] and a θ′-free zone forms in their vicinity [42].

3.3.3. *Experimental Results*

To compare experimental observations with the analytical results presented in Section 3.2.2, we locate θ′ and θ particles on the analytical stability map shown in Figure 21b based on their volume, aspect ratio, and aging/overaging temperature. The result is shown in Figure 22. The lower bound of observed θ′ aspect ratios as a function of particle size at each temperature is plotted as a dotted line for comparison with analytical predictions of the critical aspect ratio.

There is generally good agreement between the analytical predictions and experimental observations. At each temperature, a minority of θ′ particles are observed below the critical aspect ratio predicted by thermodynamic analysis. However, the lower bound of experimentally observed θ′ aspect ratios follows the same basic trend as the analytical predictions. The possible implications

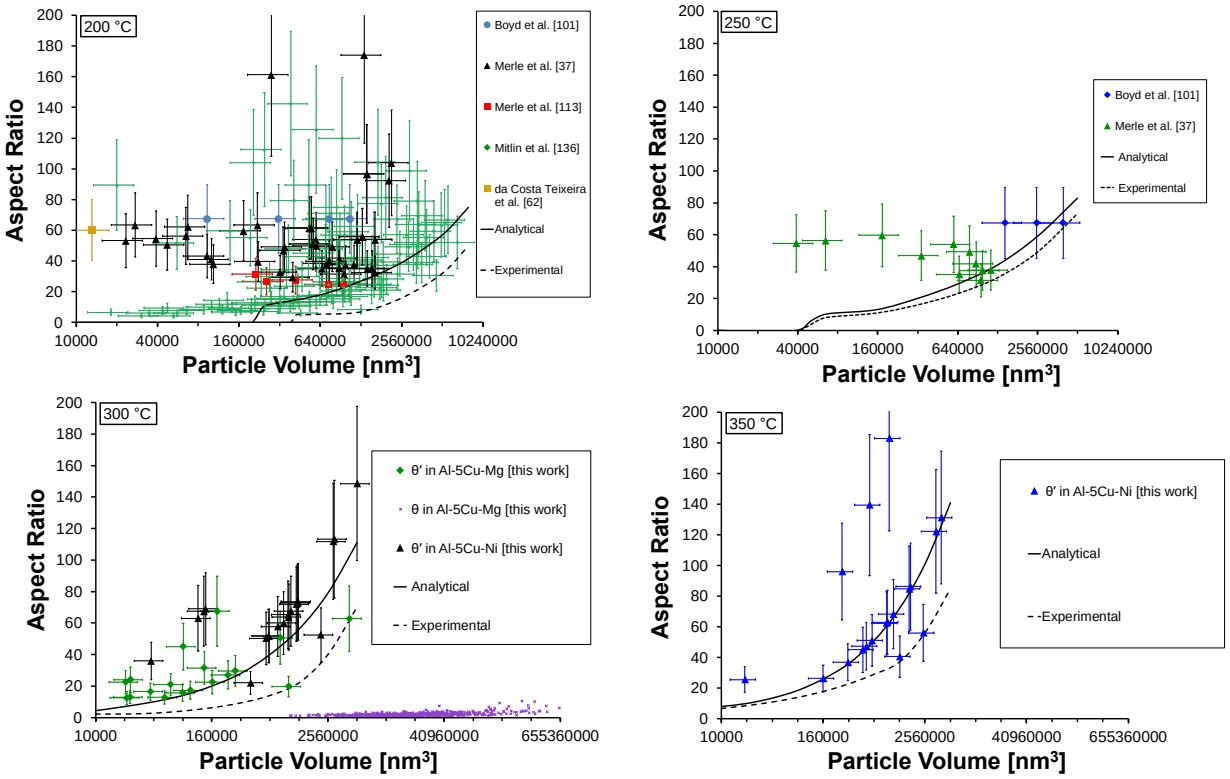

Figure 22. Experimentally observed particle volumes and aspect ratios compared to the analytically predicted critical aspect ratio at various temperatures. Most θ′ particles fall in the expected regime. Possible explanations for those that don't are described in Section 3.4. Data on θ′ morphologies was collected from Milton *et al.* [136], Merle and Merlin [113], Merle and Foquet [37], Boyd and Nicholson [101], and da Costa Teixeira *et al.*[62].

of this discrepancy are discussed in Section 3.4. At 300 °C, θ particles were observed. These particles all had low aspect ratios relative to θ′ (<10), and comprise a distinct morphological regime. While there is no precise agreement on critical aspect ratio values, the experimental results support the premise that the phase stability of θ′ particles is related to their size and aspect ratio. Note that the data plotted at 200 °C and 250 °C was collected from binary Al-Cu alloys reported in the literature, while the data plotted at 300 °C and 350 °C was collected from engineering alloys, with possible thermodynamic modifications to interfacial energy and/or strain energy due to solute segregation [118].

3.4. Phase Field Approach: Investigating the role of Nucleation

Both the analytical and experimental approach used in this study suggested that the onset of θ′ → θ transformation is tied to θ′ particles reaching a critical aspect ratio during overaging. However, there is incomplete agreement on the value of that aspect ratio under different conditions. As shown in Section 3.3, some θ′ particles in experimental microstructures appear at geometries predicted to be thermodynamically unstable. If both the thermodynamic analysis and experimental observation are correct, this suggest that a thermodynamic driving force is a necessary but not sufficient criterion for phase transformation. It is possible that θ′ particles existing below their critical aspect ratio are in a state analogous to undercooling. This would imply that there is a driving force for their transformation into the θ phase, but either insufficient time has passed for the continuous kinetics of the process to proceed, or a discreet, random nucleation event required for transformation simply has not occurred at the particle interface. If that is true, the introduction of a θ nucleus to a θ′ particle below the critical aspect ratio should result in of θ′ → θ transformation.

This is difficult to evaluate experimentally, but can be tested with phase field modeling. In this section we use phase field simulations to recreate a θ nucleation event, and observe the competition between θ′ and θ phases under a range of conditions.

Phase field modeling is a computational tool that simulates microstructural evolution over time. In this work, we use phase field modeling to predict the evolution of θ′ and θ particles during overaging. This involves deriving mathematical descriptions of each phase's thermodynamic and kinetic properties and designing simulations that effectively assess specific questions or hypotheses. The baseline model developed for this purpose is described in Section 4.2.1.

3.4.1. *Phase Field Model for θ Nucleation*

In the phase field approach, we assess the conditions under which θ can readily nucleate and grow. Specifically, our objective is to simulate a nucleation event and evaluate whether a θ particle would be stabilized or destabilized under a certain set of conditions. Given repeated experimental observations that θ particles tend to nucleate on the semi-coherent interface of θ′ particles [90-92], we place a θ nucleus at this location and observe the competition between phases. The specifics of the simulation are described below.

There are benefits and drawbacks to this approach that complement the experimental and analytical methods described previously. Both the analytical approach and phase field models predict phase evolution on the premise that the microstructure will tend to minimize free energy. However, there are a set of simplifying assumptions inherent to the phase field model. Atoms and interfaces are not explicitly tracked, so the lattice structure rearrangement and ledge growth that characterize the evolution of physical Al-Cu microstructures can only be approximated. There are several parameters required by the phase field model that are fit to physical values like interfacial energy

and diffusivity. When constructing a simulation of the Al-Cu microstructure, additional assumptions about initial condition, lattice misfit, and the anisotropy of properties must also be made. Fewer assumptions are required in an analytical approach. The phase field approach, however, also has several capabilities that the analytical approach does not. The phase field model predicts how a virtual microstructure with multiple phases evolves over time. Thus, it can simulate the explicit interaction between the θ′ and θ phases and predict intermediate stages of phase transformation: how particle size, particle morphologies, stress fields, chemical potential fields, and the balance of elastic vs. chemical vs. interfacial energy of the microstructure shifts as the transformation progresses.

With these capabilities and limitations in mind, a phase field simulation was designed to study the multi-phase competition between θ′ and θ. This simulation was based on a two-phase model established in prior work [119], which is itself based on the free energy constructions of the Al-Cu system developed by Chen, Wolverton, and others [95, 97, 137]. Simulations were designed using the Multiphysics Object Oriented Simulation Environment (MOOSE) [138]. Whereas the two-phase model described the thermodynamics and kinetics of the α and θ′ phases, the multiphase model must also include a description of the equilibrium θ phase. This description consists of the phase's bulk free energy as a function of composition and temperature, its lattice misfit with the α-Al matrix, its interfacial energy, and its growth kinetics. Each of these components is discussed in the following paragraphs, and defined numerically in this chapter's appendix.

The bulk free energy of the θ phase is critical to an accurate simulation, because it defines the driving force for θ′ → θ transformation, as well as the equilibrium Cu content of the α-Al matrix. In Table 8, the free energy of each phase at its equilibrium composition is given as a function of temperature. However, the phase field model also requires the free energy of each phase as a

function of Cu content. As suggested by Chen *et al*. [137] and implemented in Section 4.2.1, this can be achieved in simulations of the α/θ′ system without sacrificing accuracy by defining free energy curves of each phase that retain key thermodynamic data: the appropriate common tangent construction between phases and the driving force for transformation. The result is shown as solid lines in Figure 23. With the addition of a third phase, an additional free energy curve is required. We define the free energy curve of the θ phase by duplicating the free energy curve of the θ′ phase and giving it an energetic offset equivalent to the temperature-dependent driving force for θ′ → θ transformation (as defined in Section 3.2.1). This results in the dashed free energy curves shown in Figure 23 along with common tangent constructions predicting the equilibrium phase compositions (the functions are defined mathematically in this chapter's appendix).

The lattice misfit of each phase is also an important part of the phase field simulations. Unlike Nabarro's analytical solution for strain energy around a particle that depends on a scalar volume misfit term, the phase field model utilizes an eigenstrain tensor term. The elastic energy contribution to the total energy of the system is calculated at each mesh point, and depends on local displacement along with the stiffness tensor of each phase [132, 133]. The misfit of the θ′ phase within the α-Al matrix has been studied extensively using microscopy, DFT, and molecular dynamics [95, 106]. Lattice misfits of +0.7% along the coherent interface and -5.1% along the semi-coherent interface of θ′ have been theoretically established and used often and successfully to construct phase field simulations [95, 97, 106, 107, 139]. These misfits are associated with a lattice correspondence of $1a_{\theta'}$: $1a_{\alpha}$ at the coherent interface and $2c_{\theta'}$: $3a_{\alpha}$ at the semi-coherent interface. However, the θ phase is generally incoherent with the α-Al matrix, so the orientation relationships and lattice correspondence are not fixed [30]. For the purpose of this simulation, we assumed that the misfit of the θ phase was isotropic. Based on the calculated volume misfit of

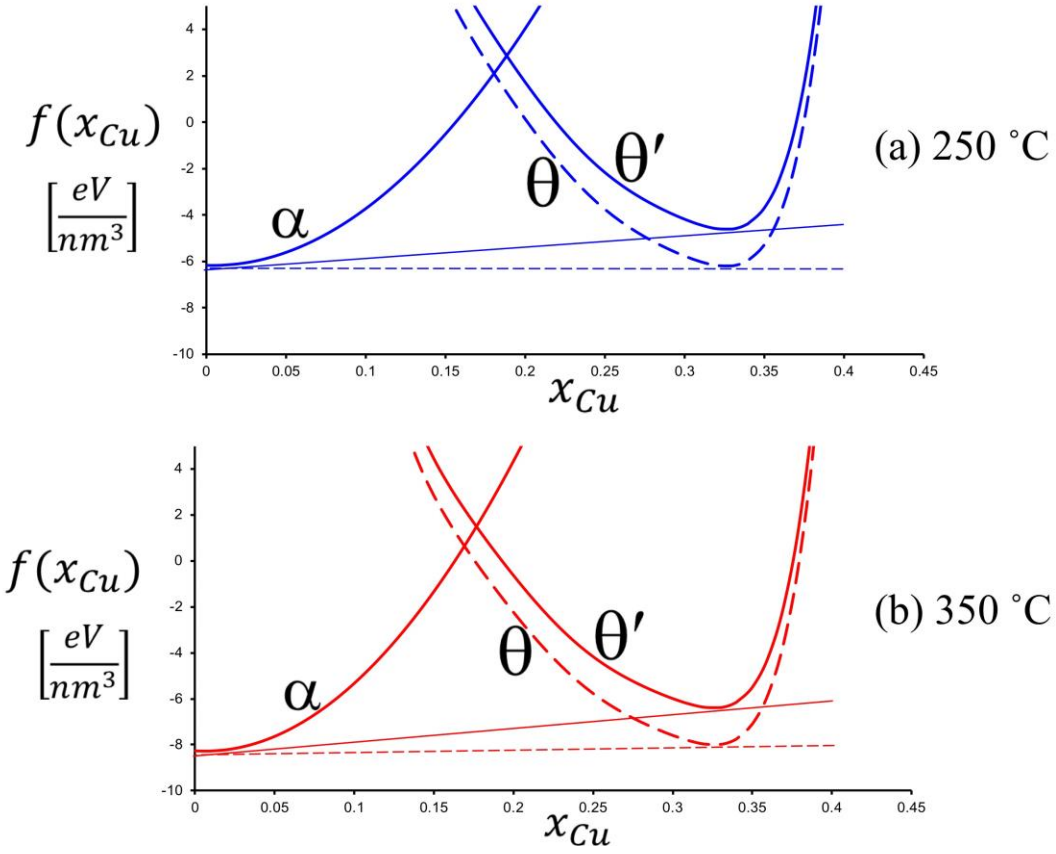

Figure 23. The temperature- and composition-dependent free energy of each phase in the present simulations, with common tangent lines drawn between the precipitate phases and the matrix phase. (a) shows the free energy functions at 250 °C, (b) shows the free energy functions at 350 °C.

-9.93% for the θ phase (Section 3.2.1), this translates to an eigenstrain of -3.43% along each dimensional axis.

The interfacial energy and growth kinetics of θ are more difficult to determine. Potential-based Molecular Dynamics calculations by Kokotin and Hecht predicted that the strain-free interfacial energy of θ within α-Al is anisotropic and depends on the orientation relationship between the particle in the matrix [41]. This is consistent with experimental observations: there are at least 15 recognizable orientation variants of θ that tend to take on distinct morphologies [90]. Based on some simplifying assumptions, Kokotin and Hecht calculated that the *average* strain-free interfacial energy of a θ particle in α-Al can be taken as 456 mJ/m^2. To this point, there have been no calculations reported that predict the interfacial energy between θ and θ′ particles. For the purpose of the current simulations, it is assumed that the strain-free interfacial energy between θ and θ′ is equivalent to the strain-free interfacial energy between θ and the α-Al matrix, and the strain-related component of interfacial energy is calculated using the microelasticity theory built into the MOOSE tensor mechanics module [138, 140, 141].

A simplifying assumption is also made in terms of the interfacial kinetics of θ. It is assumed that the interfacial mobility parameter for the θ phase, L_θ, is equivalent to $L_{\theta'}$, which seems reasonable given *in situ* observations of their similar growth/dissolution rates [90, 92]. Given that these simulations are aimed at predicting the outcome of the thermodynamic competition between a θ nucleus and an existing θ′ particle rather than the rate of phase transformation, this assumption is not expected to introduce any unacceptable inaccuracies.

With the simulation parameters in place, an initial condition for the virtual microstructure must be selected. In this case, the goal is to simulate a newly nucleated θ particle and observe whether that nucleus tends to grow at the expense of the θ′ phase or vice versa. The form of the virtual θ′ particle

in two dimensions was determined by the volume and aspect ratio being simulated, based on a disk-shaped three dimensional morphology. The initial morphology of the virtual θ′ phase was a rectangle with a height equivalent to the required disk thickness and a length equivalent to the disk diameter.

For our simulations, we placed the θ nucleus at the semi-coherent interface of θ′. This is the most realistic nucleation site, as suggested by multiple factors: several experimental observations of such θ nucleation have been reported, theoretical treatment suggests that the nucleation barrier for θ is minimized at planar defects (such as particle interfaces and grain boundaries) where curvature and Cu content are maximized [3], the coherency loss associated with θ formation requires dislocations which are present at the semi-coherent interface of θ′ [91], and because strain energy is minimized by the contractional eigenstrain associated with the θ particle conforming with the contractional eigenstrain at that interface.

The form of the nuclei was chosen to reflect the structure present at the instant after a nucleation event. We reason that the simplest structural rearrangement that could occur is the formation of half a unit cell of θ. We choose a half unit cell thickness of 0.304 nm, equivalent to bisecting the θ unit cell along either of its two *a* axes. Thus, we place the θ nucleus at the semi-coherent interface of a θ′ particle, extending 0.304 nm into the α-Al matrix from the edge of the θ′ (Figure 24). We then allow the simulation to proceed and observe whether the θ′ grows at the expense of the θ particle, or if the θ nucleus is stabilized and grows at the expense of θ′ (Figure 24). This simulation is performed for two θ′ particle sizes at 250 °C and three particle sizes at 350 °C. For each particle size, it is repeated with decreasing θ′ aspect ratios to observe whether or not such morphological changes induce a change in the stability of θ. Figure 24 shows the two possible outcomes of these simulations.

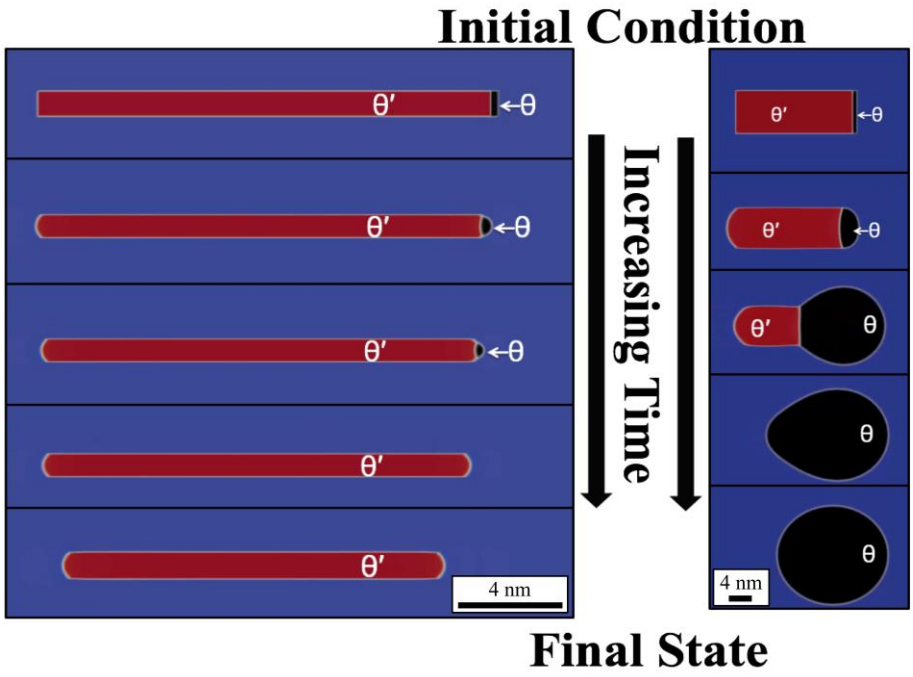

Figure 24. The competition between an existing θ′ particle and a θ nucleus placed on its semi-coherent interface, as predicted by phase field simulations for two sample conditions. Generally, higher aspect ratio θ′ particles are more stable against phase transformation into θ.

3.4.2. *Phase Field Results Compared with Analytical Predictions*

As shown in Figure 24, the two possible outcomes of a simulation are that the θ nucleus is stabilized and grows at the expense of θ′, or that the θ′ particle is stabilized and the θ nucleus is consumed. Figure 25 shows the simulated analytical stability map for 250 °C and 350 °C (reproduced from Figure 21), along with one data point for each simulation.

The phase field results are consistent with the analytical results, predicting that θ′ precipitates with small aspect ratios will tend to evolve to the θ′ phase, while those with larger aspect ratios remain in θ′ phase. For example, they predict that at 250 °C, a θ′ particle with a volume of 160,000 nm^3 will become destabilized below an aspect ratio of 15. That is, if a θ nucleus forms on the semi-coherent interface of such a particle, the θ particle will tend to grow at the expense of the θ′ particle. Meanwhile, for a smaller θ′ particle with a volume of 40,000 nm^3, there is no critical aspect ratio, and the θ′ particle will be stabilized regardless of its morphology.

The 350 °C phase field results show good agreement with the analytical results. At each θ′ size, there was a critical aspect ratio where the θ nucleus became stabilized. This critical aspect ratio was more sensitive to particle size than the analytical results predicted. In sum, the addition of a θ nucleus to a virtual θ′ particle largely reproduced analytical predictions for the phase stability of θ′ particles. This supports the hypothesis that the θ′ → θ phase transformation will tend to occur once a θ′ particle reaches a critical aspect ratio and a θ nucleus forms on its semi-coherent interface.

3.5. Discussion

In this section, we present a unified description of the onset of the θ′ → θ phase transformation based on the results produced by each approach, frame our conclusions in the light of prior work,

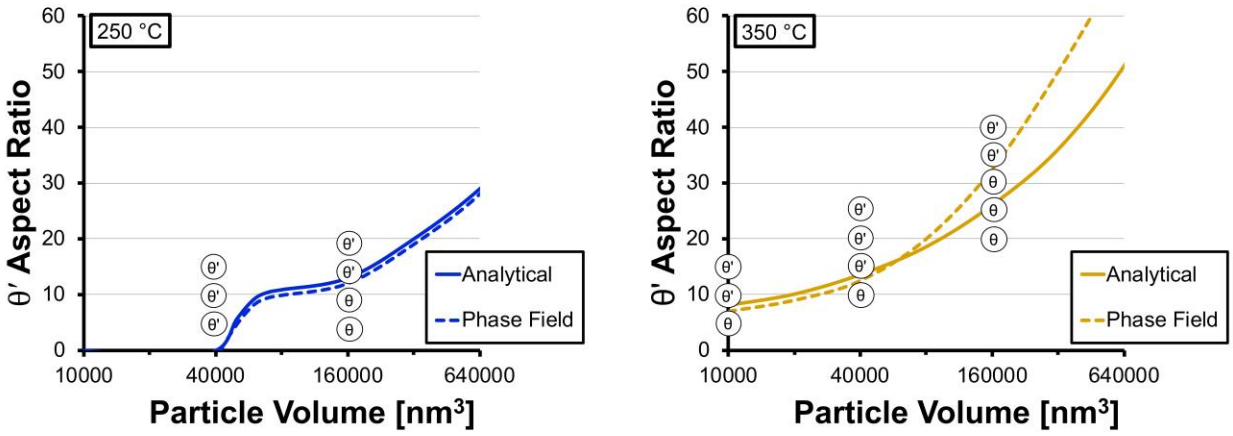

Figure 25. Phase field predictions of the stability of a θ′ particle with a θ nucleus formed at its semi-coherent interface, compared to the analytical stability maps described in Section 3.2. Both phase field results and thermodynamic analysis suggest that for a given temperature and particle size, there is a critical aspect ratio of θ′ below which it is destabilized and will tend to transform into θ.

and discuss a few important considerations that our main results did not address.

Thermodynamic analysis (Section 3.2) suggests that θ′ → θ phase transformation will become thermodynamically favorable if the aspect ratio of θ′ is below a critical value. Experimental observations (Section 3.3) are largely in agreement with these predictions: most θ′ particle exist above the critical aspect ratio predicted by thermodynamics, and all θ particles are below the critical aspect ratio. However, some θ′ precipitates exist below the critical aspect ratio. It was hypothesized that θ′ particles below the critical aspect ratio has a driving force to evolve into the θ phase, but the phase transformation requires the introduction of a θ nucleus. Phase field simulations in which a θ nucleus was present at the semi-coherent interface of θ′ were consistent with this hypothesis. The simulation results showed that if the θ′ particle was above the critical aspect ratio, the θ nucleus was unstable, bet below the critical aspect ratio, θ was stabilized and grew at the expense of θ′.

Taken together, the present results suggest that the formation of the θ phase during overaging of Al-Cu alloys depends on two criteria: θ′ particles coarsening to a thermodynamically unstable morphology, and the formation of a θ nucleus at the semi-coherent interface of θ′. Note that the formation of a θ nucleus was not explored here. In the phase field approach, we introduced a θ nucleus at the beginning of the simulations, and the simulation results specifically indicated conditions where a small θ nucleus, once formed by any mechanism, will grow without any free energy barrier. In reality, the formation of a θ nucleus is associated with a local loss in coherency at or near the semi-coherent interface of θ′ [91, 101, 142]. It is unclear what critical condition would lead to this local incoherency becoming energetically favorable, but a buildup in elastic lattice strain is likely involved [124], and Eshelby predicted that the conformational strain

associated with disk-shaped particles like θ′ is inversely proportional to the particles' aspect ratio [128]. Therefore, any strain-related nucleation conditions might imply a critical aspect ratio criterion similar to the purely thermodynamic criterion developed here.

Another consideration worth noting is the precise meaning of the analytical stability maps presented in Figure 21. They predict the aspect ratio below which a θ′ particle residing in a purely α/θ′ microstructure will have a driving force to undergo phase transformation. However, both the free energy calculations shown in Figure 20 and prior experimental observations suggest that once an initial θ particle forms, the thermodynamic nature of microstructural evolution shifts towards a coarsening mechanism, as incoherent θ particles with high interfacial energies grow at the expense of metastable θ′ particles regardless of θ′ particle aspect ratio [30, 42, 92]. Therefore, the initial formation of a θ particle quickly leads to microstructural degradation in its vicinity and marks a critical transition in the overaging of Al-Cu microstructures. This highlights the importance of understanding and isolating the onset of θ′ → θ phase transformation.

The analytical approach proves useful in defining a critical aspect ratio for the stability of θ′ precipitates, but has some inherent limitations. It does not account for the temperature dependence of interfacial energy, and makes a very specific comparison between θ′ and θ phases: two particles of equal aspect ratio and number of constituent atoms. In reality, a θ particle can take many morphologies in the intermediate stages of phase transformation. There are at least 15 distinct orientation relationships [90], each with slightly different interfacial energies and preferred particle shapes. The phase field approach was intended to address some of these shortcomings by simulating intermediate steps of phase evolution and inter-particle interaction.

One benefit of the analytical approach presented here is that it can easily be modified to account for other factors such as variable particle geometries. Various morphologies of θ′ that have been

observed (disks, square tetragonal prisms, hexagonal prisms, octagonal prisms) [7, 14, 101]. While the analytical approach assumed the classical disk-shaped θ′ particle, these other morphologies can be used to generate analytical stability maps analogous to Figure 21. The results for a square tetragonal prism, the observed morphology which is farthest removed from a disk in terms of surface area to volume ratio, is shown in Figure 26 below. It slightly increases the critical aspect ratio compared to the disk-shaped θ′ particle. Note that Boyd and Nicholson observed several faceted and non-faceted morphologies of θ′ during overaging of Al-Cu and concluded that faceting of θ′ particles had no significant impact on coarsening rate or the loss of interface coherency [101].

3.6. Conclusions

We analyzed the θ′ → θ phase transformation that occurs during overaging of Al-Cu alloys using a combination of thermodynamic analysis, experimental observations, and phase field modeling. It is concluded that coarsening of θ′ is interlinked with θ′ → θ transformation.

We present evidence that the onset of this detrimental phase transformation is determined by temperature and the morphology of the θ′ particles present in the microstructure, and follows a predictable series of events: As θ′ particles in an as-aged Al-Cu microstructure begin to coarsen and reduce their aspect ratio towards the equilibrium value, they eventually reach an aspect ratio at which their transformation into the θ phase becomes thermodynamically favored (Figure 20). If a particle is below this "critical aspect ratio" and a θ nucleus forms on its semi-coherent interface, the θ phase will tend to be stabilized and grow at the expense of θ′. If the resultant θ particle is of comparable size to the surrounding θ′ particles, it will continue to coarsen at their expense.

We also conclude that the value of the "critical aspect ratio" varies in a predictable way: The "critical aspect ratio" increases as temperature and particle size increase (*i.e.* larger θ′ particles at

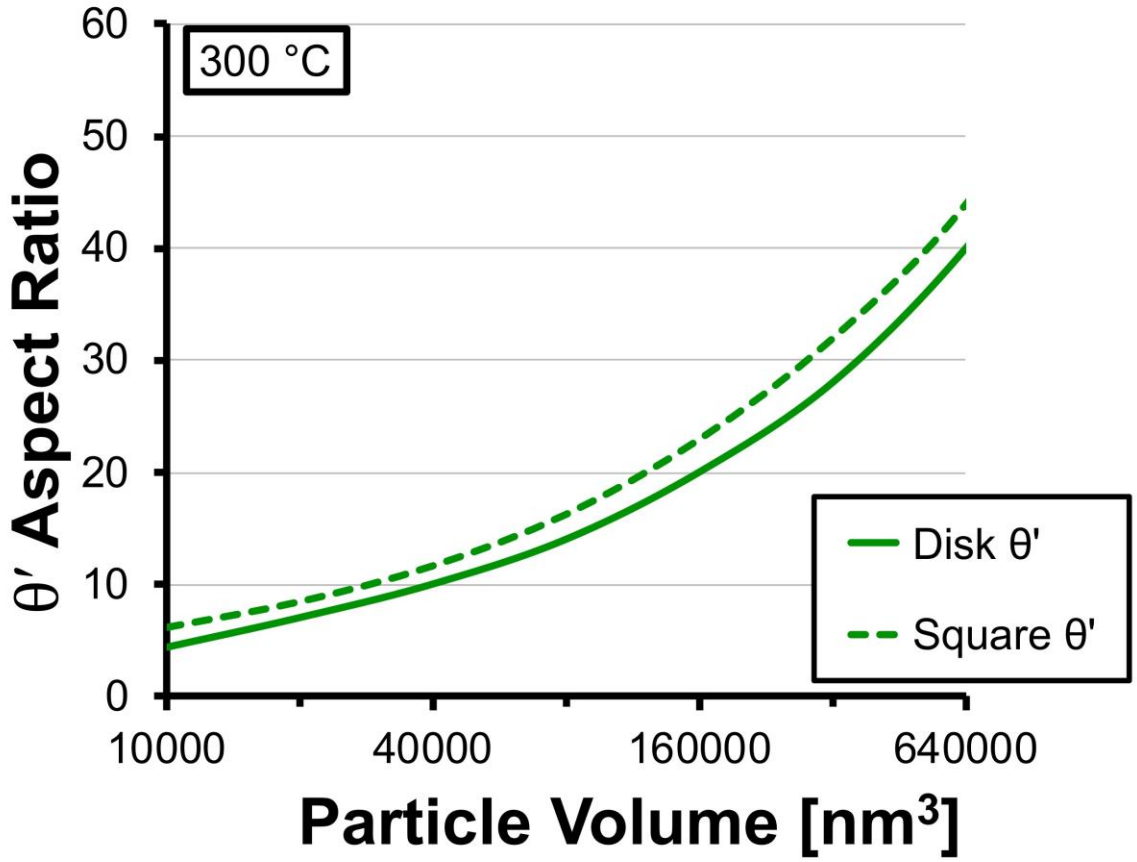

Figure 26. Assuming θ′ takes a square prismatic morphology slightly increases the critical aspect ratio relative to a disk-shaped morphology.

higher temperatures are more prone to phase transformation), as shown in Figure 21b. Finally, at temperatures of 250 °C and below, there is also a "critical particle volume" below which θ′ precipitates of any aspect ratio of will be stabilized against phase transformation.

In sum, the phase stability of θ′ precipitates at any given temperature is determined by their size and aspect ratio, so that stabilizing θ′ precipitates against detrimental transformation into the θ phase requires that are resistant to coarsening and aspect ratio reduction during overaging.

3.7. Chapter 3 Appendix

The free energy functions of each phase used in the simulations described in this chapter are shown below. The form of the functions is parabolic, described in Equation 12. The coefficents of each free energy function are given in Table 10.

$$f\left[\frac{ev}{nm^3}\right] = a \cdot {x_{Cu}}^6 - b \cdot {x_{Cu}}^5 + c \cdot {x_{Cu}}^4 - d \cdot {x_{Cu}}^3 + e \cdot {x_{Cu}}^2 - h \cdot x_{Cu} + j \quad (12)$$

Table 10. Coefficients of the free energy functions used in this study for the solution and precipitate phases at each temperature. The form of these functions is given in Eq. 12.

Temperature	Function	a	b	c	d	e	h	j
250 ˚C	f_α					265	1.9843	-6.17846
	f_θ	2.265E+06	3.266E+06	1.933E+06	6.012E+05	1.039E+05	9.594E+03	3.799E+02
	$f_{\theta'}$	2.265E+06	3.266E+06	1.933E+06	6.012E+05	1.039E+05	9.594E+03	3.815E+02
350 ˚C	f_α					337	4.2593	-8.27332
	f_θ	2.28E+06	3.29E+06	1.95E+06	6.06E+05	1.05E+05	9.65E+03	3.77E+02
	$f_{\theta'}$	2.28E+06	3.29E+06	1.95E+06	6.06E+05	1.05E+05	9.65E+03	3.79E+02

Chapter 4

Temperature-Dependent Stability of θ′-Al_2Cu Precipitates Investigated with Phase Field simulations and experiments

This chapter is revised based on a published journal article with Patrick Shower as lead author:

P. Shower, J. Morris, D. Shin, B. Radhakrishnan, L. Allard, A. Shyam, Temperature-dependent stability of θ′-Al2Cu precipitates investigated with Phase Field theory and experiments, Materiallia 5 (2019) 100185.

My primary contributions to this paper include (i) objectives and design of study (ii) microstructural analysis (iii) developing and running phase field simulations for θ′ evolution (iv) literature review (v) most of the writing.

Abstract

The upper limit of service temperature for many Al-Cu alloys is determined by the thermal stability of strengthening θ′ (Al_2Cu) precipitates. Above a certain temperature, θ′ precipitates will undergo morphological evolution and transform into the detrimental, equilibrium θ phase, leading to a rapid drop in strength. Certain alloying elements have recently been reported to increase the thermal stability of θ′ precipitates, by mechanisms that are yet unclear. Herein, we investigate the effect of modified interfacial energy and solute chemical mobility on the thermal stability of θ′ *via* high-throughput phase field study. We identify a critical θ′ aspect ratio to predict the onset of θ formation. Using this criterion, we predict the time required for θ′ to θ phase transformation as a function of temperature, Cu diffusivity, and the interfacial energy of θ′ precipitates. The predicted times compare favorably with reported times for formation under similar experimental conditions. These phase field simulations predict that a moderate reduction in Cu mobility or matrix-precipitate interfacial energy is adequate to stabilize the as-aged microstructure up to 300 ˚C, while substantial reductions to both interfacial energy and Cu mobility are needed to achieve similar stability at 400 ˚C. Experimental microstructural evolution results in commercial (319) and thermally stabilized (RR350) cast aluminum alloys are presented to complement the simulations.

4.1. Introduction

The mechanical properties of precipitate strengthened Al-Cu-(Si) alloys depend heavily on the volume fraction, number density, and aspect ratio of the strengthening precipitates [33]. At elevated homologous temperatures ($T/T_{Melt} > 0.5$), the number density and aspect ratio of precipitates in these alloys tend to decrease due to coarsening (Ostwald ripening and shape evolution) [6, 7]. For many commercial cast Al-Cu and Al-Si-Cu alloys, the primary strengthening precipitates are disc-shaped particles of the metastable θ′ phase (body centered tetragonal Al_2Cu, a=4.04 Å and c=5.80 Å) [1]. The as-aged microstructures in these alloys are populated by θ′ precipitates with a high number density and average aspect ratio (diameter/thickness) in the range of 25-50 [30]. Above approximately 225 $^{\circ}$C, the as-aged microstructure of these alloys deteriorates over time as θ′ particles rapidly coarsen [1, 6, 7, 35, 36]. As larger particles grow at the expense of smaller particles, individual particles also undergo shape evolution, reducing their aspect ratio [30, 37]. Eventually, this morphological evolution leads to a phase transformation as the detrimental, equilibrium θ phase (tetragonal Al_2Cu) nucleates on coarsened, low aspect ratio θ′ particles [30, 38, 39]. The formation of the θ phase further accelerates the coarsening process because it has high-energy, incoherent interfaces with the Al matrix [40, 41]. The θ phase may coarsen at the expense of finer θ′ particles, and the mechanical properties of the alloy deteriorate substantially following this phase transformation (~60% reduction in strength and hardness) [1, 6, 34, 42]. The reduced mechanical properties limit the usefulness of many cast Al-Cu-(Si) alloys at elevated temperatures [2].

It is, therefore, desirable to develop alloys in which the onset of θ′ to θ transformation is delayed or prevented at elevated temperatures. Such high temperature stabilization of θ′ has been recently reported: The addition of Mn and Zr to an Al-Cu alloy results in a θ′ strengthened microstructure

which is morphologically stable to a temperature of at least 350 ˚C [42]. Mechanisms have been proposed to explain the thermal stability of these alloys (termed *ACMZ* alloys hereafter), but the extent to which the individual mechanism(s) account for the high temperature microstructural stability remains unclear. It is also reported that Mn and Zr both tend to segregate to the interfaces between θ′ and the aluminum matrix [14]. This suggests that Mn and/or Zr might reduce the interfacial energy of θ′, which would lower the thermodynamic driving force for particle coarsening [30, 118]. It is also plausible that Mn and/or Zr atoms could provide a kinetic barrier, inhibiting the diffusion of Cu atoms to and from θ′ particles [26, 115].

The relative importance of kinetic versus interfacial thermodynamic mechanisms in stabilizing θ′ precipitates in ACMZ alloys is difficult to determine experimentally. Phase field simulations are, however, well suited for such an investigation. Phase field simulations have been successfully implemented to recreate microstructural phenomena in several materials systems (see reviews for various systems [143-147]), and in more recent years to guide materials design. In the case of the Al-Cu system, nucleation [98, 148-151], growth [97, 107], shape evolution [100, 137], and coarsening [95, 152] processes associated with θ′ have been simulated and are in broad agreement with experimental results. Here, we use phase field modeling with comparison to experiment to evaluate the potential sources of the thermal stabilization phenomenon described above, with the intent of determining whether its nature is most likely thermodynamic, kinetic, or a combination of the two. The thermodynamic and kinetic effects of solute segregation are treated implicitly, using inputs from *ab initio* calculations and diffusivity databases, to provide specific information on the role of Cu diffusivity and matrix/θ′ interfacial free energy on the kinetics of coarsening. We examine the role of both thermodynamic and kinetic modifications in determining the morphological stability of Al-Cu microstructures, and describe how their relative importance

varies with temperature.

The chapter is organized as follows: In Section 4.2, we first introduce the phase field model used in the study and then describe how thermodynamic and kinetic modifications are implemented. We further describe what metrics are used to evaluate the evolution of the simulated microstructure. In Section 4.3, we show phase field results and compare them to prior analytical approaches, as well as experimental microstructures. In Section 4.4, we discuss the implications of these results on alloy design and the understanding of overaging in Al-Cu alloys.

4.2. Materials, Methods, and Modeling Rationale

In Section 4.2.1 below, we first describe our phase field model, and the parameters that we have chosen to model the development of the Al-Cu systems. Section 4.2.2 describes the choices of modified parameters for Cu diffusivity and interfacial energetics, chosen to examine the potential of such changes for stabilizing the microstructure. In Section 4.2.3, we describe the choice of initial microstructures, and how that was selected based on experimental observations. Section 4.2.4 describes a phenomenological approach for determining the "lifetime" of the preferable θ′ microstructure, based upon the θ′ aspect ratio. Finally, Section 4.2.5 describes the experimental methods necessary for comparison with the model.

4.2.1. *Phase Field Formalism and Input Parameters for Simulations*

A two-dimensional phase field simulation of the Al-Cu system was implemented in the Multiphysics Object-Oriented Simulation Environment (MOOSE) framework [138]. Using analytical tools available in MOOSE, phase field formulations with demonstrated effectiveness in prior work [95, 100, 137, 152] were augmented with inputs from density functional theory (DFT)

calculations to account for new microstructural observations. The simulation included the solid solution α-Al matrix and the metastable θ′-Al_2Cu precipitate phase. The physical and chemical descriptors incorporated in the simulation included each phase's temperature- and composition-dependent bulk free energy, lattice constants, temperature-dependent stiffness tensors, and anisotropic interfacial energy, as well as the temperature-dependent mobility of Cu. The formulation and implementation of each of these descriptors are detailed below. First, the generic formulas are outlined, and then each term is described in more detail.

The phase field model seeks to simulate microstructural evolution on the premise that the microstructure will tend to evolve towards a lower free energy state. In these simulations, the evolution of local Cu concentration was dictated by the Cahn-Hilliard equation (Eq. 13) and the local phase evolution was governed by the Allen-Cahn formulation (Eq. 14) [143] given below.

$$\frac{\partial x_{Cu}}{\partial t} = \nabla \cdot M_{Cu} \nabla \frac{\delta F}{\delta x_{Cu}} \tag{13}$$

$$\frac{\partial \eta}{\partial t} = -L \frac{\delta F}{\delta \eta} \tag{14}$$

where x_{Cu} represents the mole fraction of Cu at a given mesh point, η is an order parameter that describes which phase is present at a given mesh point (η has a value of 0 for the α phase and 1 for the θ′ phase), M_{Cu} is the chemical mobility of Cu, and L is interfacial kinetic coefficient. F is the total free energy of the system. Eq.s 13 and 14 are linked by the free energy, which indicates that compositional and phase evolution are coupled. F is found using the following formulation:

$$F = \int_{Volume} \left(f_{bulk} + f_{gradient} + f_{lattice\ strain}\right) d(Volume) \tag{15}$$

where f_{bulk} describes the Gibbs free energy of each phase, $f_{gradient}$ describes energy associated with compositional gradients and interfaces between phases, and $f_{lattice\ strain}$ describes energy associated with elastic lattice strains. These quantities are all expressed in terms of energy per unit volume.

For each mesh point in the simulation, f_{bulk} is calculated using the following formula:

$$f_{bulk} = f_{\theta'}(x_{Cu}) \cdot g(\eta) + f_{\alpha}(x_{Cu}) \cdot \big(1 - g(\eta)\big) \tag{16}$$

where $f_{\theta'}$ is the bulk free energy of the θ′ phase, f_{α} is the bulk free energy of the α phase, and g is a switching function that smoothly transitions from a value of 0 in the α phase to 1 in the θ′ phase:

$$g(\eta) = 3 \cdot \eta^2 - 2 \cdot \eta^3 \tag{17}$$

This type of free energy construction (Eqs. 16 and 17) has been commonly used in prior phase field modeling of the Al-Cu system when only a single order parameter is required [106]. In models which have used multiple order parameters to describe the orientation variants of the θ′ phase (e.g. η1, η2, η3), additional functions are required to establish the energetic equivalence of each θ′ variant and the exclusivity of each variant (such that only one variant could be present at a given mesh location). The most common type of function is a Landau polynomial with multiple degenerate minima and symmetry operations, as described elsewhere [95]. Our model, however, only included a single order parameter, allowing us to utilize the more straightforward approach described by Chen [106]. Using the single order parameter, η, we used existing capabilities in the MOOSE framework to locally assign the correct Euler angle to the stiffness tensor, transformation strain, and interfacial energy anisotropy of θ′, as described later in this section.

To find $f_{\alpha}(x_{Cu})$ and $f_{\theta'}(x_{Cu})$, the molar Gibbs free energy of formation of each phase at

temperatures and compositions of interest was obtained from the TCAL3 database as implemented in Thermo-Calc, as shown in Figure 27. $f_\alpha(x_{Cu})$ was calculated for Cu concentrations of 0% and 33 atomic%. Because the θ′ phase has a fixed stoichiometry, its free energy is captured in a single data point at each temperature.

The inability to directly calculate the free energy of θ′ (a line compound) as a function of Cu composition presents a challenge in phase field simulations, which describe microstructures using continuously variable composition and order parameter fields [143]. This problem has been addressed by Chen *et al*., who introduced parabolic fitting functions of raw free energy data that retain critical thermodynamic parameters including the driving force for phase transformation and equivalent chemical potential between θ′ and α [95, 100, 137, 152]. This method [100] is used to derive parabolic functions describing the composition- and temperature-dependent bulk free energy of each phase. These functions are of the form shown in Eq. 18, with coefficients tabulated in Table 11.

$$f\left[\frac{ev}{nm^3}\right] = a \cdot {x_{Cu}}^6 - b \cdot {x_{Cu}}^5 + c \cdot {x_{Cu}}^4 - d \cdot {x_{Cu}}^3 + e \cdot {x_{Cu}}^2 - h \cdot x_{Cu} + j \tag{18}$$

Additionally, $f_\alpha(x_{Cu})$ and $f_{\theta'}(x_{Cu})$ at 400 °C are plotted in Figure 28.

$f_{gradient}$ is also calculated for each mesh point in the simulation, using Eq. 19:

$$f_{gradient} = \frac{\kappa_\eta}{2} \cdot \left|\nabla_\eta\right|^2 + \frac{\kappa_{Cu}}{2} \cdot \left|\nabla_{x_{Cu}}\right|^2 \tag{19}$$

Here, κ_η and κ_{Cu} are gradient coefficients related to the energy of phase interfaces and compositional gradients, respectively. The interfacial energy (γ) of θ′ precipitates was calculated using DFT calculations, as described elsewhere [14]. Interfacial energy was calculated separately for the coherent $(1\ 0\ 0)_\alpha||(1\ 0\ 0)_{\theta'}$ interface and the semi-coherent $(0\ 1\ 0)_\alpha||(0\ 1\ 0)_{\theta'}$ interface, and was assumed to be constant with respect to temperature. The gradient coefficient terms required

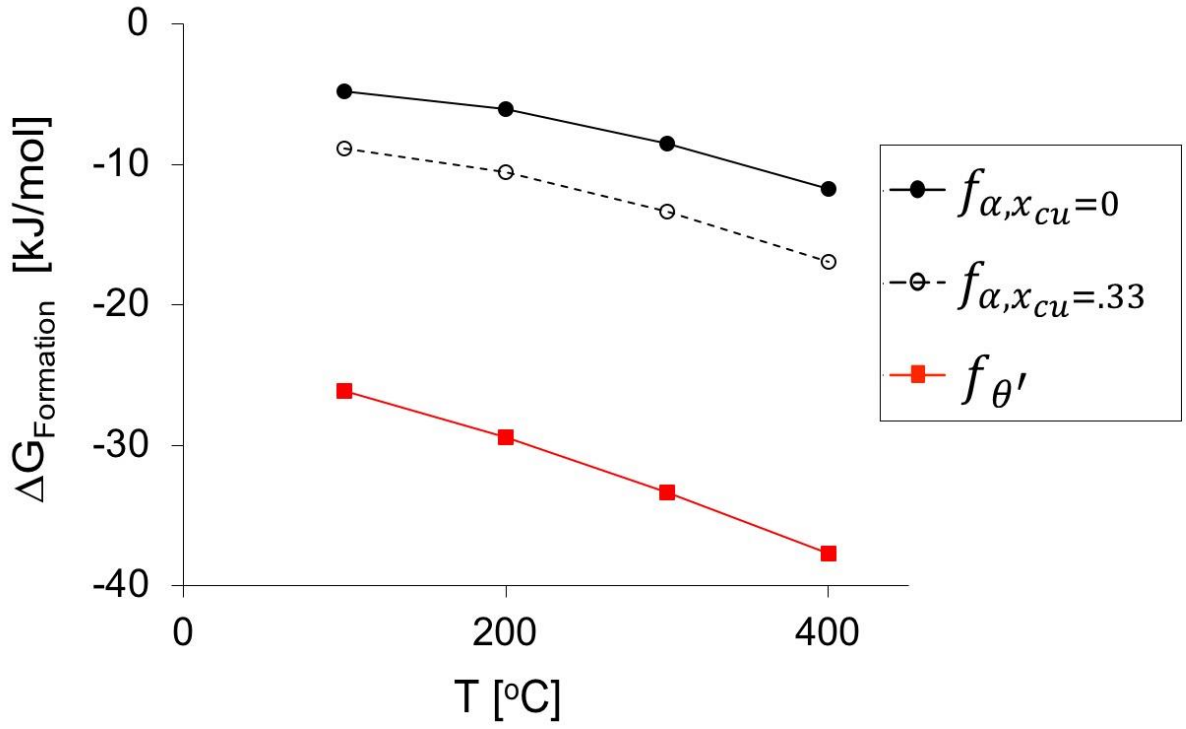

Figure 27. The free energy of formation of α and θ′ phases as a function of composition and temperature, as calculated by ThermoCalc. $f_{\alpha}(x_{Cu})$ and $f_{\theta'}(x_{Cu})$ in Eq. 16 were derived using these data by a method described previously [35].

Table 11. Coefficients of the free energy functions used in this study for the solution and precipitate phases at each temperature. The form of these functions is given in Eq. 18.

Temperature	Function	a	b	c	d	e	h	j
100 ˚C	f_{α}					$2.450 \cdot 10^{2}$	$1.225 \cdot 10^{0}$	$-2.995 \cdot 10^{0}$
	$f_{\theta'}$	$1.336 \cdot 10^{6}$	$1.929 \cdot 10^{6}$	$1.144 \cdot 10^{6}$	$3.562 \cdot 10^{5}$	$6.196 \cdot 10^{4}$	$5.913 \cdot 10^{3}$	$2.621 \cdot 10^{2}$
200 ˚C	f_{α}					$2.815 \cdot 10^{2}$	$1.408 \cdot 10^{0}$	$-3.829 \cdot 10^{0}$
	$f_{\theta'}$	$2.260 \cdot 10^{6}$	$3.259 \cdot 10^{6}$	$1.929 \cdot 10^{6}$	$6.000 \cdot 10^{5}$	$1.037 \cdot 10^{5}$	$9.581 \cdot 10^{3}$	$3.824 \cdot 10^{2}$
300 ˚C	f_{α}					$3.300 \cdot 10^{2}$	$1.650 \cdot 10^{0}$	$-5.338 \cdot 10^{0}$
	$f_{\theta'}$	$2.270 \cdot 10^{6}$	$3.272 \cdot 10^{6}$	$1.937 \cdot 10^{6}$	$6.024 \cdot 10^{5}$	$1.041 \cdot 10^{5}$	$9.607 \cdot 10^{3}$	$3.805 \cdot 10^{2}$
400 ˚C	f_{α}					$3.270 \cdot 10^{2}$	$1.635 \cdot 10^{0}$	$-7.364 \cdot 10^{0}$
	$f_{\theta'}$	$2.299 \cdot 10^{6}$	$3.314 \cdot 10^{6}$	$1.962 \cdot 10^{6}$	$6.100 \cdot 10^{5}$	$1.053 \cdot 10^{5}$	$9.689 \cdot 10^{3}$	$3.772 \cdot 10^{2}$

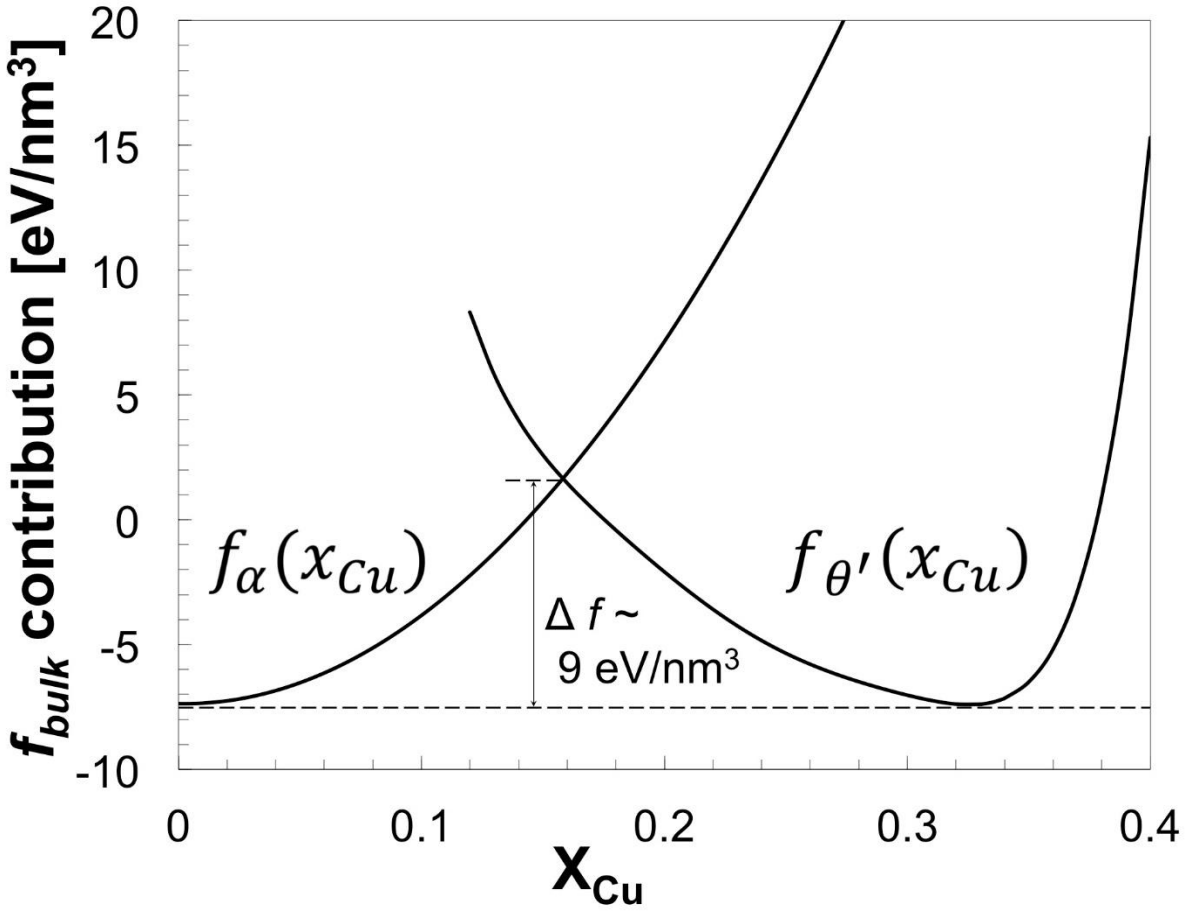

Figure 28. Bulk free energy functions of the α-Al and θ′ phases at 400 ºC. Compare to Figure 1 in [100], Figure 11 in [95], and Figure 6 in [106].

by Eq. 19 were calculated from γ values using the method described by Kim *et al*. [100]. Because the excess energy at the simulated θ′ interfaces arises from a combination of parameters including κ_{Cu}, κ_{η}, and f_{bulk}, each of these must be accounted for in order to implement the desired values for γ. The relationship between these terms was derived by Cahn and Hilliard [153], and is applied to the α/θ′ system in Eq. 20 [95, 100]:

$$\gamma = 2 \cdot \int_{x_{Cu,\alpha}}^{x_{Cu,\theta'}} [\kappa_{Cu} \cdot \Delta f_{bulk}(x_{Cu})]^{\frac{1}{2}} \cdot \left[1 + \frac{\kappa_{\eta}}{\kappa_{Cu}} \cdot \left(\frac{d\eta}{dx_{Cu}}\right)^2\right]^{\frac{1}{2}} dx_{Cu} \tag{20}$$

where $\Delta f_{bulk}(x_{Cu})$ is the difference between f_{bulk} at a given value of x_{Cu} (minimized with respect to the value of η using the switching function) and the common tangent construction between f_{α} and $f_{\theta'}$ at that composition, $\frac{d\eta}{dx_{Cu}}$ is the change in order parameter with respect to composition, calculated using the value of the order parameter that minimizes f_{bulk} at the given composition, $x_{Cu,\alpha}$ (the Cu content of α) is taken to be 0.0025, and $x_{Cu,\theta'}$ (the Cu content of θ′) is taken to be 0.33. Again following the approach outlined in Ref. [100], γ, $\Delta f_{bulk}(x_{Cu})$, and $\frac{d\eta}{dx_{Cu}}$ were calculated initially, leaving two unknown parameters, κ_{Cu} and κ_{η}. κ_{Cu} was then assigned the same value assumed in prior work [95], and finally κ_{η} was calculated using Eq. 20. κ_{η} was calculated separately for the coherent and semi-coherent interfaces. Because $\gamma_{coherent}$ and $\gamma_{semi-coherent}$ were assumed to be constant, and $\Delta f_{bulk}(x_{Cu})$ was relatively invariant with temperature, the calculated values of $\kappa_{\eta,coherent}$ and $\kappa_{\eta,semi-coherent}$ were also relatively invariant with temperature. In order to improve the model's simplicity and consistency, $\kappa_{\eta,coherent}$ and $\kappa_{\eta,semi-coherent}$ were assumed to be temperature-independent, and were assigned a single value based on the average of their values calculated at each temperature. The values of each interfacial parameter are given in Table 12.

Table 12. Interfacial energies of the coherent and semi-coherent interfaces reported by Shyam et al. [14] were used to determine the gradient coefficient terms required by Eq. 19.

Parameter	Value
γ_{coherent}	1.610 $\left[\frac{\text{eV}}{\text{nm}^2}\right]$ [3]
$\gamma_{\text{semi-coherent}}$	3.289 $\left[\frac{\text{eV}}{\text{nm}^2}\right]$ [3]
$\kappa_{\eta,\text{coherent}}$	4.128 $\left[\frac{\text{eV}}{\text{nm}}\right]$
$\kappa_{\eta,\text{semi-coherent}}$	10.290 $\left[\frac{\text{eV}}{\text{nm}}\right]$
κ_{Cu}	3.826 $\left[\frac{\text{eV}}{\text{nm}}\right]$

To calculate κ_η values at interface orientations intermediate to the coherent and semi-coherent interfaces of θ′, a compound sinusoidal function was used to smoothly interpolate between $\kappa_{\eta,coherent}$ and $\kappa_{\eta,semi-coherent}$ as a function of interface orientation. This function is:

$$\kappa_\eta = 1.845 \cdot \cos(4\psi + 180^o) + 3.081 \cdot \sin(2\psi + 90^o) + 9.055 \quad (21)$$

where ψ denotes the angle of the interface normal relative to that of the semi-coherent interface. The resulting κ_η profile is shown in a Wulff plot format in Figure 29. For comparison, the κ_η profile produced by applying the prior methodology [95, 100] to the same interfacial energy values is also plotted. The smooth, continuous energy minima applied in the present study serve to improve computational efficiency in the MOOSE framework.

The calculation of $f_{lattice\ strain}$ using the microelasticity theory of Khachaturyan *et al.* [154] within the MOOSE framework is described elsewhere [138, 140, 141]. The principal inputs to this calculation are the stiffness tensors of each phase and the lattice mismatch between them. The temperature-dependent stiffness tensors of α-Al and θ′ were taken from acoustic measurements in the literature [132, 133] and are provided in Table 13. The anisotropic lattice mismatch between the α and θ′ phases along each interface was calculated by Vaithyanathan *et al.* using DFT models [95]. These calculations yield a 0.7% (dilatational) misfit of the θ′ particle along the coherent interface and a -5.1% (contractional) misfit along the semi-coherent interface. These misfit strains were adopted in the present study and assumed to be invariant with precipitate size, as applied by others [95]. Although this is a simplification, multiple DFT studies have suggested that neither coherent nor semi-coherent interfacial energy of θ′ vary significantly with precipitate size [106, 110].

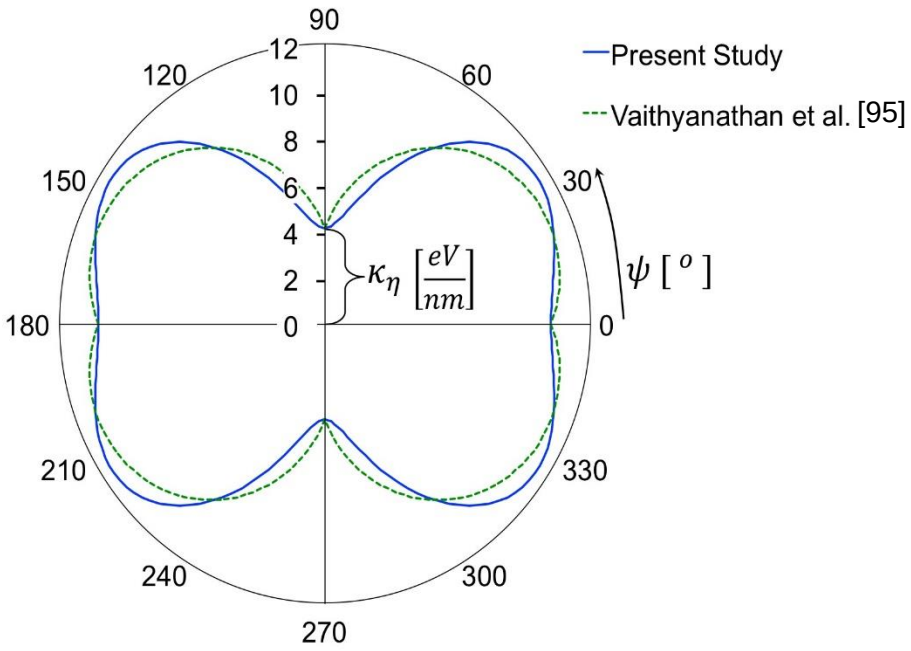

Figure 29. A Wulff plot showing $\boldsymbol{\kappa_\eta}$ vs. interface orientation angle $\boldsymbol{\psi}$ as used in this study (Eq. 21). A $\boldsymbol{\kappa_\eta}$ vs. $\boldsymbol{\psi}$ relationship which has been used in prior studies [95] is also plotted. The primary difference in the present study is the smoothing of the utilized energy minima.

Table 13. Elastic Constants of Al and θ′, values from the literature [132, 133]

	Elastic moduli of α and θ′ [GPa]									
	FCC α Aluminum				Tetragonal θ′					
	c11	c12	c44		c11	c33	c44	c66	c12	c13
100 ˚C	101.0	59.8	26.0		178.8	169.7	28.0	44.2	72.0	75.3
200 ˚C	99.8	58.8	25.7		176.8	167.0	27.6	43.4	72.0	73.9
300 ˚C	95.6	57.8	24.1		174.8	164.3	27.3	42.6	72.0	72.6
400 ˚C	91.3	56.8	22.5		172.8	161.7	27.0	41.8	72.0	71.2

The mobility of Cu (M_{Cu} in Eq. 13) was also calculated using the formula presented by Vaithyanathan *et al.* in their simulations of the α/θ′ system, given below [95]:

$$M_{Cu} = D_{o,Cu} \cdot e^{-\frac{Q_{diff,Cu}}{R \cdot T}} \cdot \{X_{Cu} - (X_{Cu})^2\} \quad (22)$$

where $D_{o,Cu}$ is the diffusional prefactor, $Q_{diff,Cu}$ is the activation energy for tracer diffusion of Cu in pure Al, R is the ideal gas constant, T is absolute temperature, and X_{Cu} is the overall molar composition of Cu in the alloy. Note that, in this approach, the mobility of Cu is independent of local Cu composition. The diffusional terms were taken from the literature [29] and X_{Cu} was set at 2.1 at.% (~4 wt. %) in the simulations to replicate the conventional cast aluminum alloy 319 [7]. The resultant mobility terms are given in the Table 14. L, the kinetic prefactor term related to the formation and dissolution of θ′, was calculated for each simulation by solving the series of temporal equations given by Vaithyanathan *et al*. [95].

In the MOOSE Framework, Eqs. 13 and 14 are discretely evaluated at each point on a Finite Element Mesh using residual equations in the weak form [155]. In the present study, the residual equations were solved at each time step using Newton's method in the PETSc software package. Adaptive time steps and mesh densities were used to maximize computational efficiency while meeting residual convergence criteria. Using increasing mesh densities, we found that the thickness of the coherent interface ($0.05<\eta<0.95$) converged to approximately 0.7 nm, while the thickness of the semi-coherent interface converged to approximately 1.1 nm. Using the standard adaptive mesh capability in MOOSE, the local mesh point distribution becomes finer if the compositional or order parameter gradient between two mesh points is a certain degree higher than the average in the simulation. We adjusted that degree to ensure that the narrowest interface, the coherent interface, was populated by 3 to 5 mesh points. This required at least 4.29 mesh points

Table 14. Diffusional terms used in this study. The baseline activation energy value and the diffusional prefactor $D_o = 0.654\ \left[\frac{cm^2}{sec}\right]$ \were taken from the literature [29], The formula used to find chemical mobility formula was taken from [35].

$Q_{diff,Cu}$ Modification	$Q_{diff,Cu}$ [kJ/mol]	Mobility at 100 ˚C [nm^2/sec]	Mobility at 200 ˚C [nm^2/sec]	Mobility at 300 ˚C [nm^2/sec]	Mobility at 400 ˚C [nm^2/sec]
0%	136	1.25E-07	1.32E-03	5.51E-01	3.82E+01
+5%	143	1.40E-08	2.35E-04	1.32E-01	1.13E+01
+10%	150	1.56E-09	4.17E-05	3.17E-02	3.36E+00
+15%	156	1.74E-10	7.40E-06	7.61E-03	9.98E-01
+20%	163	1.95E-11	1.31E-06	1.83E-03	2.96E-01
+25%	170	2.18E-12	2.33E-07	4.39E-04	8.79E-02

per nm of interface. Thus, we utilized an adaptive mesh with a maximum, density of 6.4 mesh points per nm of interface.

4.2.2. *Quantifying the Influence of Global Kinetic and Thermodynamic Parameters*

Once a baseline model for the α/θ′ system was established, a numerical experiment was designed to quantify the influence of interfacial thermodynamics and diffusion kinetics on microstructural stability. Specifically, the time required for a virtual α/θ′ microstructure to evolve beyond a critical aspect ratio (as discussed in Section 4.2.3 below) was measured as a function of temperature, Cu mobility, and the interfacial energy of θ′. To frame this approach differently, we used phase field simulations to quantify the thermodynamic and/or kinetic modifications necessary to stabilize the α/θ′ microstructure at different temperatures. This strategy is described below.

Once a virtual microstructure was established, the effects of modifying the thermodynamic and kinetic parameters associated with interfacial energy and Cu diffusion, respectively, on that microstructure's evolution were quantified. Thermodynamic modifications were introduced in order to reduce the driving force for microstructural evolution, while kinetic modifications were introduced in order to impede the rate-limiting step for microstructural evolution. These modifications are not a direct simulation of the Mn and Zr segregation to the interface of θ′ that has been observed experimentally . Instead, they are intended to capture the thermodynamic and kinetic effects that such solute segregation might produce.

Considering the high temperature coarsening of the α/θ′ microstructure, the interfacial energy of θ′ particles provides the primary thermodynamic driving force. Ostwald ripening and shape evolution take place concurrently, reducing interfacial free energy as the large number of small, high aspect ratio (25-50) θ′ particles in the as-aged microstructure evolve into fewer, larger θ′

particles with an aspect ratio closer to the low equilibrium value (2-5) [37, 100]. Within this system, the semi-coherent interface has a greater energy (due to its structural and chemical differences with the Al matrix) and mobility (due to the ledge mechanism by which θ′ grows) than the coherent interface and is largely determinant in coarsening behavior [30, 123]. The interfacial energy of the semi-coherent interface was, therefore, identified as the key global parameter controlling the system's thermodynamics. We introduced reductions in $\gamma_{\text{semi-coherent}}$ up to -25% (a value which recent DFT work suggests is reasonable for alloying additions of Mn and Zr [118]), in increments of 5%, thereby implementing systematic interfacial thermodynamic modifications to the virtual microstructure. For each level of thermodynamic modification, $\kappa_{\text{semi-coherent}}$ was recalculated using Eq. 21 and Eq. 22 was refit to the new value (see Table 15 for values).

The kinetics of θ′ coarsening are volume diffusion controlled, limited by the mobility of Cu in the α-Al matrix [30, 115]. In order to simulate a rate-limiting step which might alter the mechanism of Cu diffusion (*e.g.* a diffusion barrier at the θ′ interface or the motion of di-vacancies or vacancy-solute clusters, as has been hypothesized for similar systems [26]), the activation energy for Cu diffusion ($Q_{diff,Cu}$ in Eq. 22) was increased by up to +25%, in 5% increments. For each level of kinetic modification, M_{Cu} was recalculated using Eq. 22 (see Table 14 for values).

With a baseline phase field model, 5 levels of thermodynamic modification, and 5 levels of kinetic modification, a 6x6 test matrix results, wherein there are 36 "simulated alloys" with modified interfacial energy and Cu mobility, each of which has a unique combination of thermodynamic and kinetic characteristics. These simulated alloys were held at various simulated temperatures to observe how their microstructures evolved. By using several simulated alloys with varying degrees of kinetic and thermodynamic modification, this approach sidesteps the need for precise knowledge of solute element characteristics while determining the sensitivity of the virtual

Table 15. Modifications to interfacial energy and gradient coefficients in the phase field simulations were introduced.

$\gamma_{\text{semi-coherent}}$ Modification	$\gamma_{\text{semi-coherent}}$ [mJ/m^2]	$\gamma_{\text{semi-coherent}}$ [eV/nm^2]	$\kappa_{\eta,semicoherent}$ [eV/nm]
0%	560	3.289	10.29
-5%	532	3.125	9.69
-10%	504	2.960	9.08
-15%	476	2.796	8.48
-20%	448	2.631	7.88
-25%	420	2.467	7.27

microstructure to these parameters. We expect that this method would be generally effective in developing a high-level understanding of which physical factors are most crucial in producing a microstructural evolution phenomenon of interest.

4.2.3. *Initial Microstructure and Simulation Conditions*

We reproduce the morphology and distribution of θ′ precipitates in an as-aged 319 aluminum alloy microstructure (alloy composition and heat treatment described elsewhere [6, 7, 42]) to create an initial *virtual microstructure*. 460 θ′ precipitates were imaged using high-angle annular dark-field (HAADF) scanning transmission electron microscopy (methods described in Section 4.2.4). A representative micrograph is shown in Figure 30a. The average number density of precipitates in the observation plane was determined to be 0.00008865 per nm^2 (as viewed along the $[100]_\alpha$ zone axis, neglecting precipitates with coherent faces parallel to the observation plane). This was implemented as 14 virtual particles populating a 397 nm x 397 nm α-Al matrix. The simulations were two dimensional, with θ′ precipitates modeled initially as rectangles (i.e. cross-sections of discs viewed edge-on). Two orthogonal orientation variants were used (excluding the third, in-plane variant which previous work suggests can only be accurately captured in a three dimensional mesh [95, 97, 100]), and 7 precipitates of each variant were included. The location of each precipitate was determined by a random number generator, under conditions that the precipitates intersected neither each other nor the simulation boundary. This method resulted in the virtual microstructure shown in Figure 30b. The simulation boundary was periodic with respect to all compositional and order parameter variables and the strain at each simulation boundary was held to zero. The thickness and diameter of the fourteen θ′ precipitates in the virtual microstructure were based on the distribution of measured precipitate dimensions. The measured and simulated

dimensions are described in histograms (Figures 30c and 30d). For comparison to precipitate dimensions observed for other alloys and heat treatments, see elsewhere [108, 109, 156, 157].

The conditions of the phase field simulations were decided based on experimental observations. Given that conventional precipitate strengthened cast aluminum alloys are thermally destabilized above 200 °C while ACMZ alloys are thermally stable to at least 350 °C, the temperature range of interest was 100 °C to 400 °C, which we sampled in 100 °C increments. The simulations were run for 200 hours of physical time, corresponding to the industrial practice of preconditioning, in which cast aluminum alloys are held at temperature for 200 hours to evaluate the thermal stability of their microstructures [2, 6, 7, 34]. The following expression [95] was used to relate simulated time (t^*) to physical time (t):

$$t^* = L \cdot |\Delta f| \cdot t \tag{23}$$

where $|\Delta f|$ is the maximum value of $\Delta f_{bulk}(x_{Cu})$.

4.2.4. *Aspect Ratio of θ' as a Metric of Microstructural Evolution*

To gauge microstructural stability as a function of temperature, kinetic modification, and thermodynamic modification, a metric of microstructural evolution must be defined. In this study, the particle aspect ratio was chosen as that metric. The aspect ratio of θ′ particles has important implications for both the mechanical properties and microstructural evolution of precipitate strengthened Al-Cu alloys. For a given volume fraction and number density of θ′ particles, the effectiveness of precipitate strengthening is diminished as average aspect ratio decreases during elevated temperature exposure [6, 40, 99]. Furthermore, the transformation of θ′ into the equilibrium θ phase, which is detrimental to mechanical properties, is predicated by the aspect ratio of θ′ particles reaching a critical value at which point the formation of incoherent θ particles

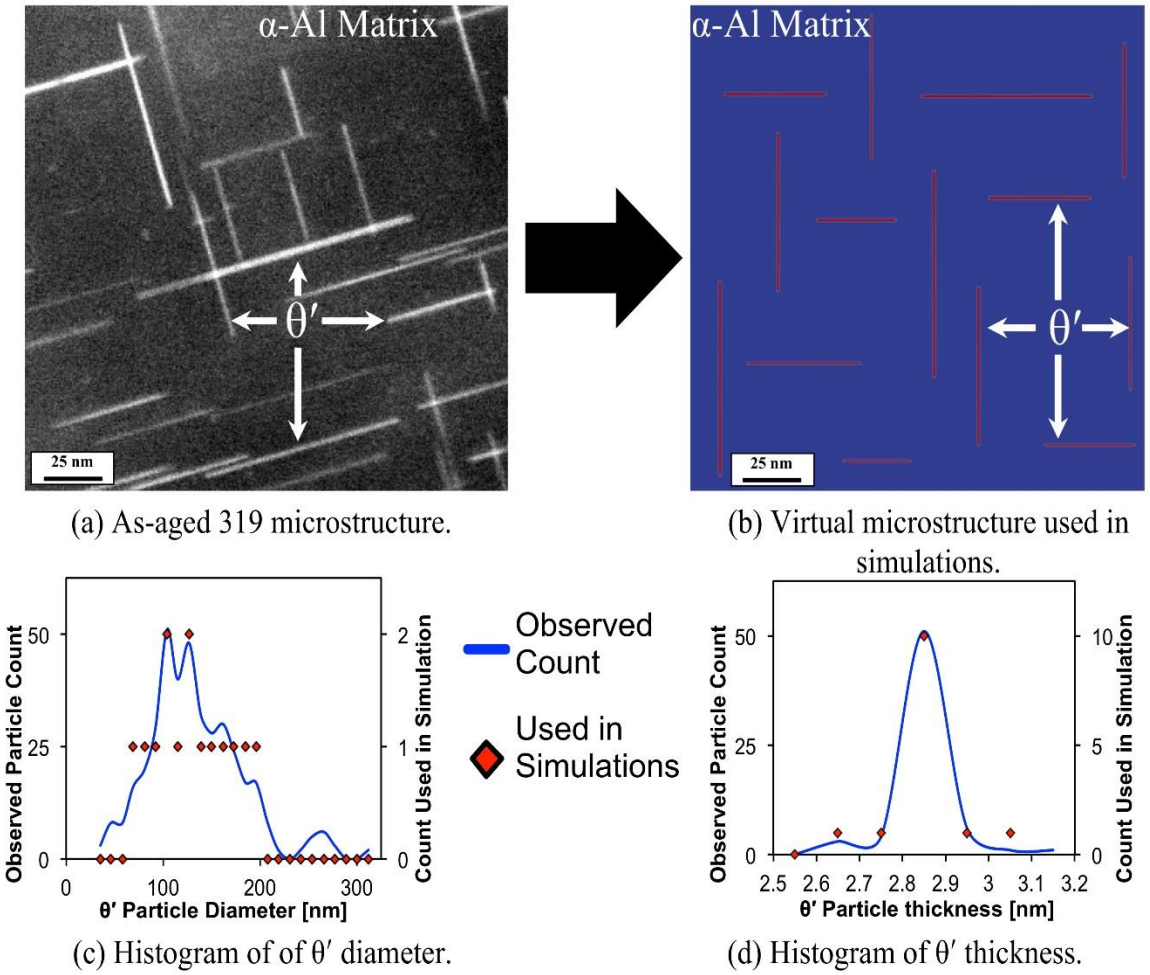

Figure 30. The microstructure of an as-aged 319 aluminum alloy was used to create an initial microstructure for phase field simulations. (a) A representative micrograph of this as-aged microstructure and (b) the virtual microstructure used as the initial condition in the phase field simulations. (c) and (d) show histograms which compare the measured distribution to the simulated distribution of θ′ particle diameter and thickness, respectively.

becomes energetically favorable [30, 37].

This "critical aspect ratio" is theoretically a function of temperature and particle size, so a range of values are possible [101]. Empirical results suggest this aspect ratio can be approximated as 13-18 in the Al-Cu alloy system [37, 38]. Preliminary calculations based on expressions given by Boyd *et al.* are consistent with this value, predicting that this critical aspect ratio is likely between 10 and 20 for temperatures and particle sizes of interest [101]. For simplicity, we choose a single value: 15. In other words, we assume that once the aspect ratio of a θ′ particle drops to 15 or below, it transforms into the θ phase. The θ phase forms as relatively large, globular particles, and is not an effective strengthening precipitate. Furthermore, due to their incoherent nature and high interfacial energy, θ particles tend to coarsen rapidly and consume nearby θ′ particles. Thus, the θ′ to θ phase transformation corresponds to a dramatic loss in mechanical properties for the alloy [1, 6, 34, 42].

Given these considerations, the point at which the aspect ratio of one or more simulated θ′ particles reduces to 15 is assumed to be the "onset of instability" in the virtual microstructure, and the physical time (t) when this onset occurs in the simulation is termed the "duration of stability" for the simulated alloy. The duration of stability was determined for each simulated alloy at each temperature. If the end of the 200-hour simulation was reached without the onset of instability, the simulated alloy was considered thermally stable at that temperature. It is noted that recent studies of coarsening in Ni alloys have also used aspect ratio to quantify microstructural evolution [158]. By using the critical aspect ratio metric as a proxy for θ′ to θ transformation in the virtual microstructure, we increased the computational efficiency of our simulations compared to a direct simulation of the phase transformation. As described later, we also found that this criterion yielded realistic predictions.

4.2.5. *Microstructural Characterization*

The microstructural evolution predicted by phase field simulations was compared to the evolution of experimental microstructures. Specifically, as-aged samples of 319 (a conventional θ′ strengthened Al alloy) and RR350 (a θ′ strengthened Al alloy containing Mn and Zr with improved thermal stability) were held at elevated temperatures (one sample each at 200 ˚C and 300 ˚C) for 200 hours and then air cooled (composition and aging conditions described in Chapter 2). After polishing and etching with Keller's reagent (by volume: 95% H_2O, 2.5% HNO_3, 1.5% HCl, 1% HF) the samples were examined using a Hitachi S4800 Field Emission Gun – Scanning Electron Microscope (FEG-SEM) in secondary electron (SE) mode.

As-aged RR350 and 319 were also examined using HAADF scanning transmission electron microscopy. Thin-foil specimens of each alloy were prepared for high-resolution electron microscopy using standard methods of electropolishing, where 3-mm diameter x 100-μm thick discs were electropolished with a TenuPol system, as described in more detail elsewhere [3]. A JEOL 2200FS STEM/TEM instrument equipped with a CEOS GmbH corrector for the illuminating lenses allowed acquisition of HAADF images of electron-transparent alloy grains oriented via a double-tilt specimen holder with the electron beam incident along a matrix <001> zone-axis orientation. Details for acquisition of the HAADF images are given elsewhere [3]. The disc-shaped θ′ precipitates are seen edge-on in bright contrast with HAADF imaging of this zone orientation, as seen in Figure 30a.

4.3. Results and Discussion

In Section 4.2, we introduced the phase-field model, and the generation of the initial microstructure. In Section 4.3.1 below, we examine how the simulated microstructures evolve, particularly the

distribution of aspect ratios. Based upon our assumption (Section 4.2.4 above) that once precipitates drop below a critical aspect ratio, they will rapidly transform into the equilibrium θ phase, we construct "stability maps" in Section 4.3.2, showing how reductions of Cu mobility and interfacial free energy affect the time required for the onset of θ′ to θ phase transformation at elevated temperatures. Section 4.3.3 compares the phase-field results to previous models and to experimental results. Finally, in Section 4.3.4, we discuss the results specifically in comparison to specific alloys where microalloying may affect both interfacial energies and diffusion between the matrix and θ′ phase.

4.3.1. *Evolution of θ′ Aspect Ratio*

In general, the phase field simulations predicted that larger particles grew at the expense of smaller particles and all particles underwent thickening and shortening as they approached the equilibrium aspect ratio. Figure 31 gives a summary of this microstructural evolution, specifically for the baseline simulated alloy at 300 ^{o}C. The largest and smallest θ′ particles in the simulation are highlighted, and their evolution can be seen by comparing Figure 31a (the beginning of the simulation) to 5b (after 100 hours). While not visually dramatic, the smaller particle has shrunk while the larger particle has grown and both have reduced in aspect ratio, as is expected during overaging. A clearer demonstration of the coarsening tendency is shown in a map of Cu's chemical potential in the evolving microstructure at 300 ^{o}C (Figure 31c). Here, it is obvious that Cu has the highest potential at the semi-coherent interface of particles, and will thus tend to migrate to where chemical potential is lowest, coherent interfaces and larger particles. There is also substantial interaction of the stress fields around precipitates, as shown in Figure 31d. Note that dislocations were not explicitly accounted for in these simulations. It has been shown that dislocations in the

α-Al matrix play a significant role in the nucleation and growth of θ′ particles [123]. In a physical microstructure, it is possible that dislocations may accommodate some amount of the inter-particle strain predicted by phase field simulations [30].

The distribution of particle aspect ratios over time was tracked in each simulated alloy at each temperature to determine when the minimum aspect ratio reduced to the critical value of 15 (chosen to represent the "duration of stability" as discussed in Section 4.2.3). We then examine this evolution as a function of interfacial energy and Cu diffusivity. Figure 32 illustrates the effects of thermodynamic and kinetic stabilization on the rate of microstructural degradation in Al-Cu alloys at 400 $^{\circ}$C. With no stabilization, the lower aspect ratio particles (which are also the smallest particles) undergo immediate and rapid shape evolution. With intermediate kinetic and thermodynamic stabilization, the minimum θ′ aspect ratio is relatively unchanged until approximately 90 hours into the simulation (possibly an effect of time-dependent impingement of Cu diffusion fields). After 90 hours, the minimum aspect ratio decreases monotonically and reaches the critical value of 15 before the end of the simulation. When the microstructure is fully stabilized, it retains its as-aged morphology and little evolution is observed during the simulation. The duration of stability of each simulated alloy at each temperature provides a single data point, and when collected, these data points provide insight into the overall trends of microstructural stability versus temperature and alloy modification. This analysis is described in the following section.

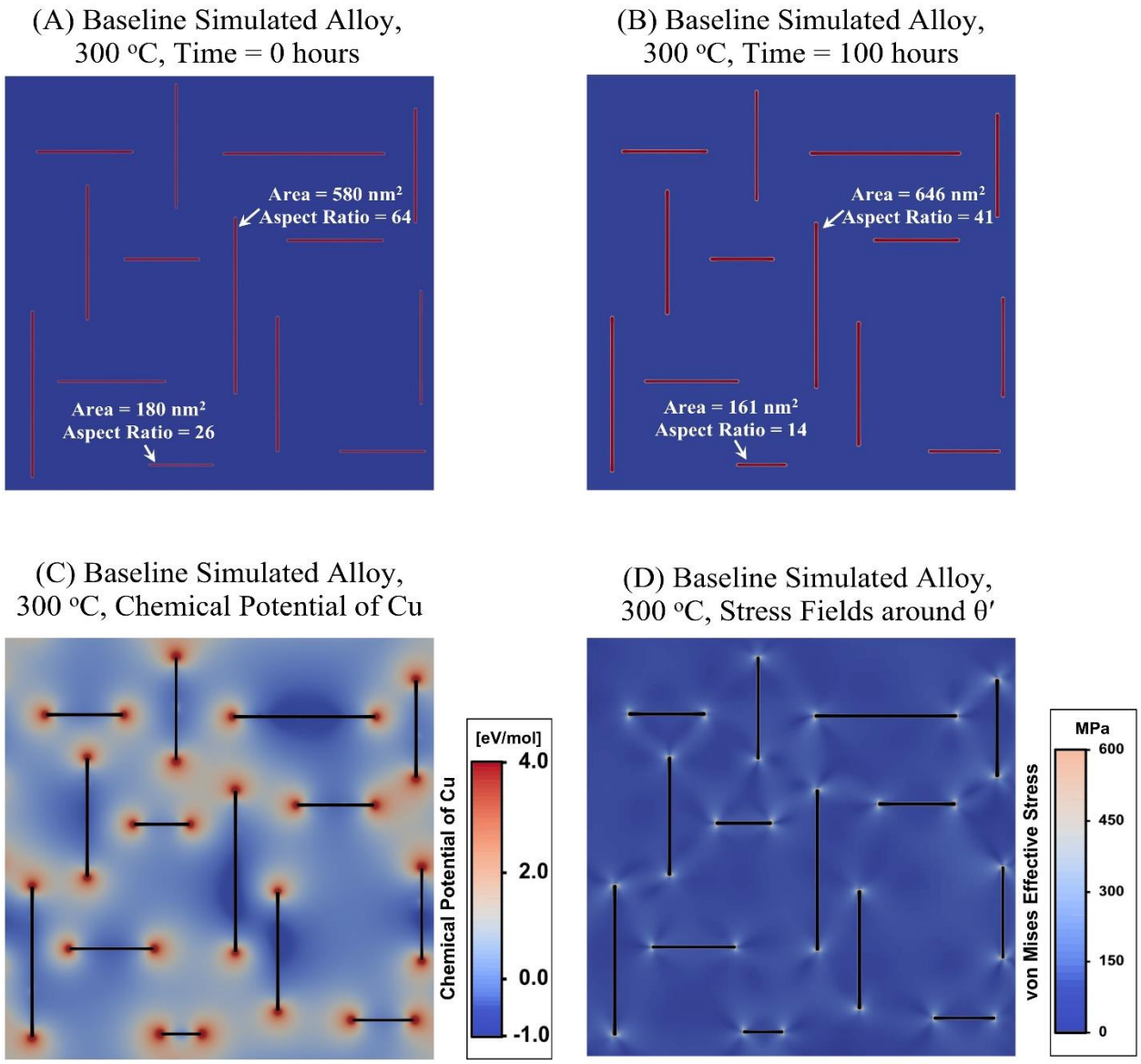

Figure 31. A snapshot of microstructural evolution in a baseline Al-Cu alloy at 300 °C predicted by the phase field simulations. (a) The initial condition of the simulation, highlighting the area and aspect ratio of the largest and smallest particles and (b) the virtual microstructure after 100 hours of evolution, soon after the critical minimum aspect ratio of 15 was reached for the smallest particle with (c) and (d) being instantaneous maps of Cu chemical potential in the simulation and the stress field surrounding θ′ particles, respectively, after 100 hours of evolution at 300 °C.

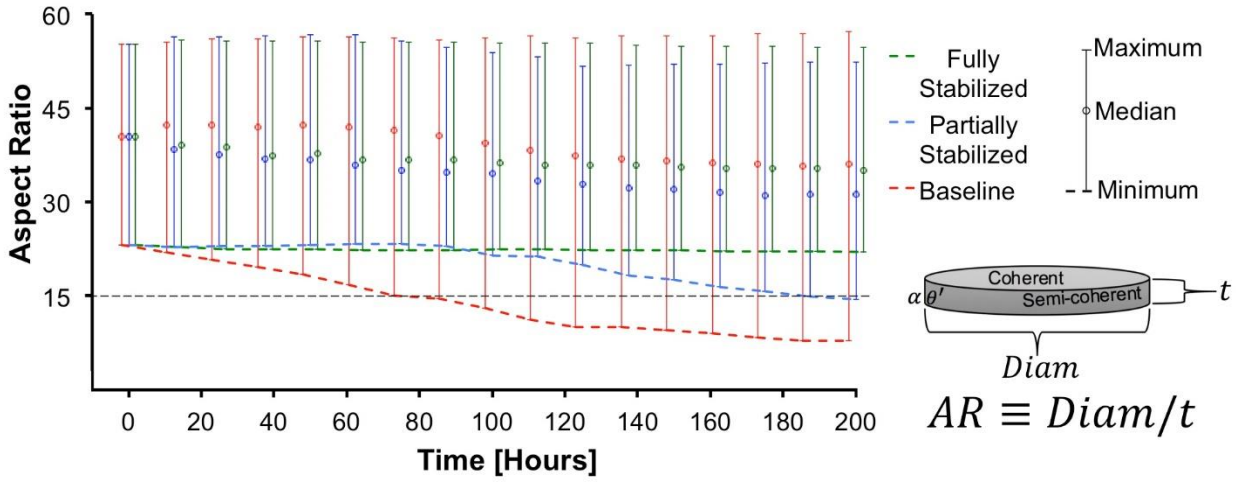

Figure 32. Distribution of θ′ particle aspect ratio vs. time for selected simulated alloys at 400 ˚C. The baseline simulated alloy has no modifications. Its "duration of stability" at this temperature is 75 hours, at which time the lowest aspect ratio reaches a critical value of 15 (see Section 4.2.4). The "Partially Stabilized" simulated alloy has a 15% interfacial energy modification and 15% $Q_{diff, Cu}$ modification. Its "duration of stability" is 187 hours. The "Fully Stabilized" simulated alloy has 25% interfacial energy modification and 20% $Q_{diff, Cu}$ modification. Its minimum aspect ratio is greater than 15 for the duration of the simulation, so its "duration of stability" is considered 200 hours.

4.3.2. *Stability Maps for θ′ to θ Evolution up to 400 ˚C*

The duration of stability described in Section 4.2.3 is plotted as a function of temperature for each simulated alloy in Figure 33. Each alloy is represented by a black dot, located on the plot according to its extent of kinetic ($Q_{diff,Cu}$) and thermodynamic ($\gamma_{semi\text{-}coherent}$, denoted "interfacial energy") modification relative to a baseline Al-Cu alloy. Interpolation between data points is done using a modified Shepard's method [60]. If a simulated alloy reached the end of the 200 hour simulation without any particles attaining an aspect ratio of 15 or less, it is considered "thermally stable" and is indicated with dark blue shading.

At 100 ˚C, all simulated alloys reach 200 hours without any θ′ particles attaining the critical aspect ratio of 15. Therefore, the "Regime of Stability" as annotated in Figure 33a includes all simulated alloys. In other words, no modifications to a binary Al-Cu alloy (represented by 0% interfacial energy modification and 0% $Q_{diff,Cu}$ modification) are necessary to achieve thermal stability at 100 ˚C. At 200 ˚C, the unmodified Al-Cu simulated alloy begins to show microstructural transformation before 200 hours.

At 300 ˚C, distinct regimes of stability and instability emerge. At this temperature, the unmodified simulated alloy is thermally destabilized early in the simulation. Furthermore, the thermal stability of any simulated alloy is most sensitive to the activation energy for Cu diffusion in that alloy (i.e. kinetics), and a 10 % modification to $Q_{diff,Cu}$ is sufficient to stabilize the simulated alloy. This observation suggests that a kinetic stabilization mechanism might be the most effective strategy to achieve microstructural stability at 300 ˚C. Considering ACMZ alloys, which experimentally demonstrate this level of thermal stability, it is likely that a mechanism which alters the kinetics of diffusion/coarsening/ledge growth would be adequate to account for such stability through solute segregation.

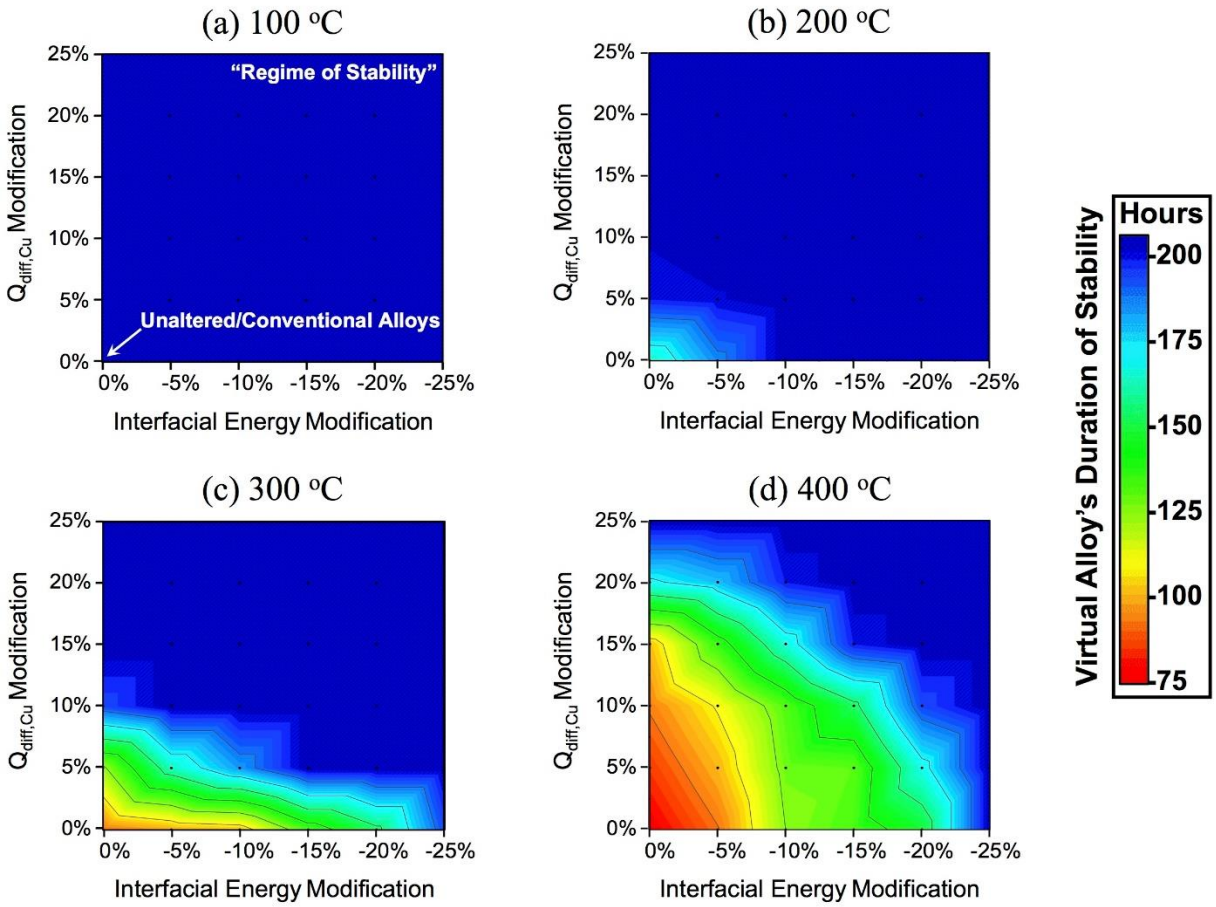

Figure 33. Duration of stability maps for 36 simulated alloys as a function of temperature. Each simulated alloy has a unique combination of thermodynamic modification (x-axis) and kinetic modification (y-axis) and is shown as a black dot. The regime of stability at each temperature is indicated with dark blue shading. (a) All simulated alloys are thermally stable at 100°C. (b) Slight kinetic or thermodynamic modification is needed to stabilize the simulated alloys at 200 °C. (c) A kinetic modification is needed to stabilize the simulated alloys at 300 °C. (d) Substantial modification to both thermodynamic and kinetic parameters is required to stabilize a simulated alloy at 400 °C.

At 400 ˚C, the regime of instability has expanded significantly, indicating that a much greater modification to a baseline Al-Cu alloy is necessary to achieve thermal stability at this temperature. In contrast to the duration of stability map at 300 ˚C, these higher temperature results indicate that microstructural stability at 400 ˚C is sensitive to thermodynamic modifications and kinetic modifications to a similar degree.

4.3.3. *Comparison to Prior Analysis and Experiment*

In order to assess the quantitative accuracies and shortcomings of the present model, three key results are compared against prior analyses and experiments: θ′ diameter evolution, θ′ aspect ratio evolution, and the onset of θ formation as a function of time and temperature. Experimental results are compared with the baseline, unmodified simulated alloy (Figures 34 and 35), and an analytical model for θ′ aspect ratio evolution from the literature [159] is used in Figure 36 to generate duration of stability maps analogous to those shown in Figure 33.

Although a direct comparison at a single temperature was not available, there is close agreement on the normalized mean θ′ diameter evolution between the phase field simulations of an unmodified, baseline Al-Cu alloy microstructure and prior experimental observations [113] as shown in Figure 34a. In a comparison with another prior work [37], mean aspect ratio had a similar initial condition and reduced over time during preconditioning in both simulation and experiment (note that the evolution of the minimum aspect ratio was used to generate the duration of stability maps in Figure 33, not the evolution of the mean aspect ratio). Experimentally, the aspect ratio dropped quickly within the first several hours of preconditioning, with the rate of change gradually reducing thereafter. The phase field simulations also predicted a rapid initial drop in mean aspect ratio, followed by a more consistent rate of change, a rate which approximately matches the later

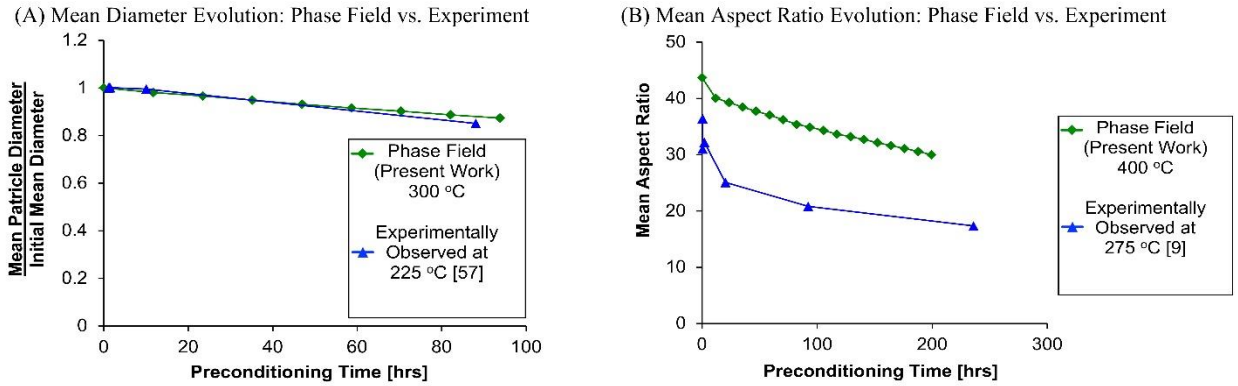

Figure 34. Comparisons of phase field predictions and experimental observations for (a) mean θ′ diameter and (b) mean θ′ aspect ratio evolution over time. The mean diameter evolution was measured at 225 °C [113] and is compared to 300 °C baseline alloy phase field predictions, normalized to account for the fact that the initial condition in the experiment was a larger mean diameter than that used in the simulations. The mean aspect ratio evolution was measured at 275 °C [37] and is compared to 400 °C baseline phase field predictions, which matches it most closely.

stages of the experimental preconditioning.

Both the aspect ratio and diameter evolutions were evaluated in a heated TEM foil, which may have resulted in surface diffusion of Cu and accelerated microstructural evolution [39, 115]. In addition, there are well documented difficulties in accurately measuring the thickness of disc-shaped θ′ particles, with low magnification measurements generally overestimating average thickness by a factor of ~2 [7, 99]. This would artificially depress the calculated aspect ratio and may be partially responsible for the discrepancy seen in Figure 34b.

We now compare the phase field prediction of θ′ to θ transformation to experimental observations in existing literature. Consistent with the phase field simulations, this transformation is observed in Al-Cu alloys when held at temperatures of 200 ^{o}C and above for adequate time. Some experiments in this area [37, 101, 103, 104, 113, 122] have been either isothermal or isochronal studies, allowing the combination of temperature and time leading to θ formation to be pinpointed. Results from these studies are plotted on a semi-log chart in Figure 35, along with predictions of the same from the current phase field simulations of the baseline alloy. There is reasonable agreement between phase field predictions and experiment, suggesting that the method used to predict θ′ to θ transformation in this work is adequately predictive. This comparison is an important benchmark for the phase field model used in this study. Given that a two dimensional simulation is used to predict the evolution of a three dimensional system, inaccuracies such as reduced lengths of diffusion paths and uncertainty in particle cross-section were introduced. These are in addition to the inherent limitations of the phase field model, such as the use of imprecise input parameters meant to represent complex, temperature-dependent processes and difficulty capturing important atomic-scale phenomena like ledge nucleation. Therefore, the fact that both prior work and the present simulations suggest relatively consistent times required for θ′ to θ transformation in binary

Al-Cu alloys is key to establishing the usefulness of the model's other results. And while the use of two dimensional simulations rather than three dimensional simulations represents a tradeoff between the number of simulations which can be performed and their individual accuracy, this indicates that the penalty to accuracy was not severe.

Along with developing phase field simulations which are representative of binary Al-Cu alloys, one key objective of the present work is to quantify the thermodynamic and/or kinetic modifications necessary to stabilize the Al-Cu microstructure at different temperatures. This result is captured in the duration of stability maps, shown in Figure 33. Given that these predictions involve adjusting parameters that cannot be directly controlled in alloy design, they cannot be directly compared to experimental results. Instead we compare the predictions to an analytical model for θ′ aspect ratio evolution that explicitly accounts for semi-coherent interfacial energy and the diffusivity of Cu [159]. Specifically, the model predicts aspect ratio evolution of a single particle in an equilibrium solid solution. This model is captured in three equations. The first, Eq. 24, states that the aspect ratio of a θ′ will evolve over time, at a rate which depends on the thermodynamic driving force for the evolution (captured in the ϕ term), and the limiting kinetics of the system (captured in the β term). Eq. 25 describes how the kinetic β term depends on alloy chemistry, temperature, copper diffusivity, and ledge growth. Eq. 26 describes how the thermodynamic ϕ term depends on the value of the particle's instantaneous aspect ratio in relationship to the equilibrium aspect ratio. The definition and values of each parameter used in these equations is given in Table 16.

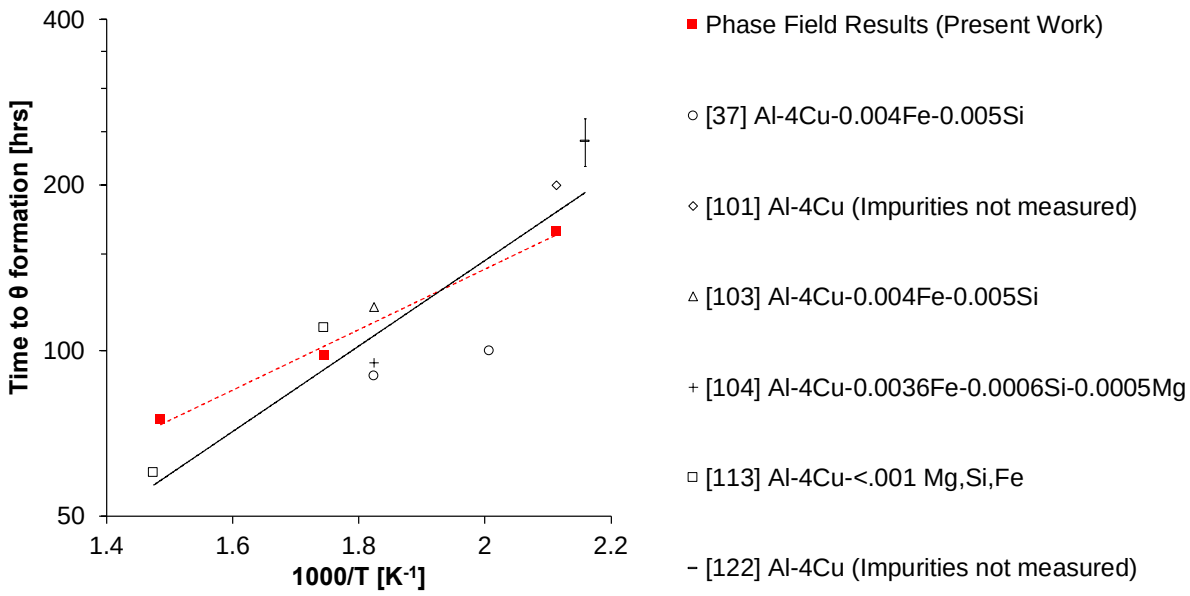

Figure 35. Preconditioning time and temperature combinations for which θ′ to θ transformation occurs in binary Al-Cu alloys (all compositions in weight percent). Experimental observations [37, 101, 103, 104, 113, 122] are plotted in black, fitted with a power law trend line. Predictions from the current phase field simulations are plotted in filled red squares and also fitted with a power law trend line. Some studies offered valuable information on θ′ to θ transformation, but either used differential scanning calorimetry [160] or could not be accurately plotted in this figure due to thin foil effects or wide time margins [90, 105, 161, 162].

$$\beta t = \phi(AR) - \phi(AR_o) \tag{24}$$

$$\beta = \frac{1}{3}\left(\frac{\pi}{4V}\right)^{\frac{2}{3}}\left(\frac{6V_m x_{Cu,\alpha}}{RT}\right)\left(\frac{D_{Cu}}{\alpha\lambda}\right)\left(\frac{\gamma_{semicoherent}}{x_{Cu,\theta'} - x_{Cu,\alpha}}\right) \tag{25}$$

$$\phi(AR) = \frac{1}{AR^{\frac{1}{3}}\left(AR - AR_{eq}\right)} - \frac{AR^{\frac{1}{3}}}{AR_{eq}\left(AR - AR_{eq}\right)} + \frac{1}{2AR_{eq}{}^{\frac{5}{3}}}\left(\ln\left(\frac{\left(AR - AR_{eq}\right)^{\frac{1}{3}}}{AR^{\frac{1}{3}} - AR_{eq}{}^{\frac{1}{3}}}\right)\right) - \frac{1}{\sqrt{3}}\tan^{-1}\left(\frac{AR^{\frac{1}{3}}}{AR^{\frac{1}{3}} + 2AR_{eq}{}^{\frac{1}{3}}}\right) \tag{26}$$

In the case of an as-aged θ′ particle with an aspect ratio much greater than the equilibrium value, this model predicts that the aspect ratio will approach the equilibrium value at a rate that decreases with time [113, 159]. To compare this model's predictions to those of the present phase field simulations, the parameters given in Table 16 were substituted into Eqs. 24 – 26 with systematic variations in $Q_{diff,Cu}$ and $\gamma_{semicoherent}$ (Section 4.2.2). The model was then used to calculate the preconditioning time required for the defined θ′ particle to reach an aspect ratio of 15, the same critical condition used for the phase field duration of stability maps. This allows for new duration of stability maps to be generated based entirely on the analytical model. These are shown for 300 ^{o}C and 400 ^{o}C in Figure 36 (the analytical model predicts that all alloy variations are stable at 100 ^{o}C and 200 ^{o}C).

There are some similarities and some discrepancies between the two sets of duration of stability maps. Generally speaking, there is agreement on the effect of $Q_{diff,Cu}$ modification, whereas the phase field simulations are more sensitive to $\gamma_{semi-coherent}$ modification (especially at 400 ^{o}C).

Table 16. Parameters used in the analytical model [159] for aspect ratio evolution of a single θ′ particle, defined by Eq.s 24 – 26.

Symbol	Definition	Value	Justification
AR_o	Initial Aspect Ratio	26	Minimum initial aspect ratio of a particle present in the simulations, and the most likely to reach the critical value of 15 first.
AR_{eq}	Equilibrium Aspect Ratio	2.04	Ratio of $\gamma_{semicoherent}$ to $\gamma_{coherent}$ shown in the supplementary file.
V	Precipitate volume	7.49×10^{-24} $[m^3]$	Volume of a disc with the diameter and thickness of the minimum initial aspect ratio particle present in the simulations.
V_m	Molar Volume of θ′	2.85×10^{-5} $[m^3]$	From the literature [113].
$x_{Cu,\alpha}$	Cu content far from θ′	. 25 $[atomic\ \%]$	Typically observed Cu content in matrix of θ′ strengthened alloys.
$x_{Cu,\theta'}$	Cu content of θ′	33.33 $[atomic\ \%]$	From stoichiometry.
D_{Cu}	Diffusivity of Cu in Al	$D_{o,Cu} \cdot e^{-\frac{Q_{diff,Cu}}{R \cdot T}}$	Calculated for each temperature/ $Q_{diff,Cu}$ combination using parameters given in the supplementary file.
$\gamma_{semicoherent}$	Interfacial energy of semi-coherent interface	Varies	Values given in the supplementary file.
α	Ratio between the width of the Cu diffusion field and θ′ ledge height	201.7	Ledge height of 0.29 nm (minimum value observed, half of c value for θ′ unit cell), diffusion field of 58.5 nm (median radius of θ′ from data in Figure 30, as suggested by Merle *et al.* [113]).
λ	Spacing between ledges	117 $[nm]$	Median diameter of θ′ from data in Figure 30, as suggested by Merle *et al.* [113]).

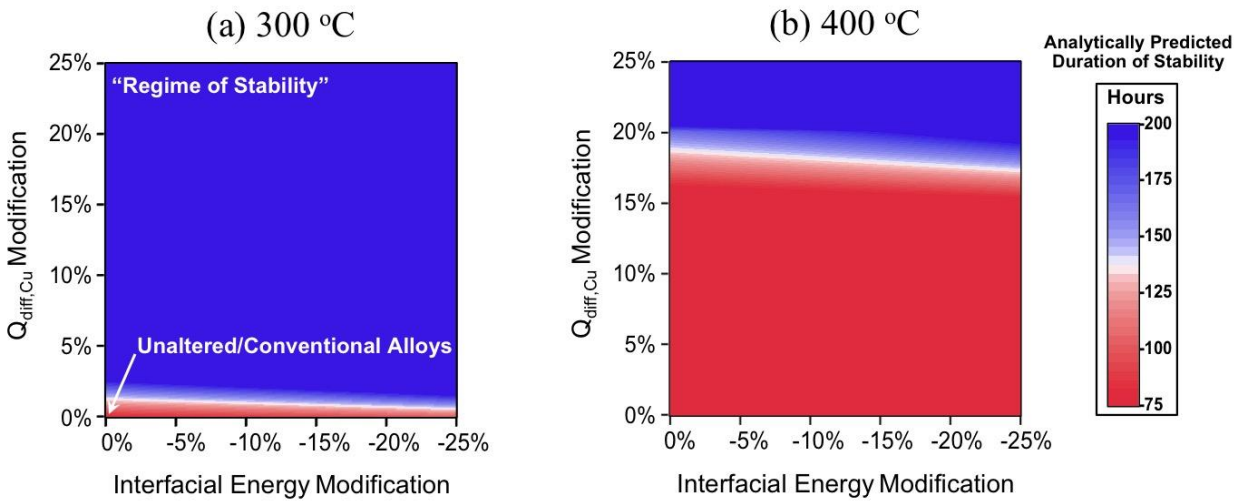

Figure 36. Duration of stability maps predicted by an analytical model for aspect ratio evolution [159] at (a) 300 °C and (b) 400 °C. The analogous duration of stability maps predicted by phase field simulations are shown in Figure 33.

According to the analytical model, $Q_{diff,Cu}$ is the dominant parameter controlling microstructural stability at every temperature. The increased sensitivity to $\gamma_{semicoherent}$ modification in the phase field simulations may be partly due to the curvature of the semi-coherent interface, which is assumed to be flat in the analytical model. This curvature increases the total area of the semi-coherent interface, and therefore its contribution to the system's total free energy. The analytical model also does not account for a particle's growth or shrinking during coarsening nor the nature of the surrounding particles – their number density, aspect ratio distribution, non-uniform Cu content due to dissolving particles *etc*. There are likely important interactive effects between particles that are not captured by the analytical model. Additionally, note that Eq.s 24-26 (as well as the Langer-Schwartz-Wagner coarsening model modified to describe disc-shaped particles [101]) predict that the rates of shape evolution and coarsening are equally sensitive to D_{Cu} and $\gamma_{semi-coherent}$: Eq. 25 indicates a dependence on the product $(D_{Cu})(\gamma_{semicoherent})$, suggesting that these cannot be entirely decoupled. However, in our calculations, D_{Cu} is being modified exponentially by adjustments in $Q_{diff,Cu}$ while $\gamma_{semi-coherent}$ is being varied linearly, thus explaining the sensitivity to $Q_{diff,Cu}$ shown in Fig. 36. This was done to reflect key physical aspects of θ′ evolution and potential stabilization mechanisms, as described in Section 4.2.2.

Overall, this comparison reveals the contrasting nature of the analytical and phase field approaches to predicting θ′ aspect ratio evolution. While the analytical approach invokes simplified particle geometry and surroundings, it also addresses a gap in the phase field approach: it allows for precise and direct modifications to particle descriptors such as interfacial energy, which require multiple fitting parameters in phase field. Moving forward, a more mechanistic phase field simulation that can explicitly illustrate the effects of solute segregation (including not only interfacial energy and Cu mobility reduction, but also solute drag and strain field interactions) is in order. The following

section discusses the implications of the present phase field simulation results for understanding current alloys and designing improved alloys.

4.3.4. *Relating Phase Field Predictions to Conventional and ACMZ Alloys*

The trends in duration of stability shown in Figure 33 correspond well with experimental observations . The microstructural evolution that occurs during 300 °C preconditioning in θ′ strengthened cast aluminum alloys 319 and RR350 is shown in Figure 37, for comparison with phase field results. In agreement with experiment [37], all simulated alloys in the phase field simulations are thermally stable at 100 °C, even the unmodified, baseline Al-Cu alloy. At 200 °C, the unmodified virtual Al-Cu alloy is destabilized near the end of the 200 hour test. The microstructure of conventional alloys (such as 319) held at this temperature, demonstrate moderate to severe coarsening of θ′ particles, and sometimes θ′ to θ transformation, depending on alloying and the duration of exposure [6, 42].

At 300 °C, the distinct regimes of stability and instability predicted by simulations correspond to the divergence in microstructure and mechanical properties between conventional and thermally stable alloys. Thermally stable ACMZ alloys such as RR350 largely retain their as-aged microstructures at this temperature while conventional alloys such as 319 show extensive degradation of their as-aged microstructures at this temperature [1, 6, 7, 35, 36]. While the precise extent of thermodynamic and/or kinetic modification caused by the segregation of Mn and Zr to the interface of θ′ particles in RR350 is unknown, the observations shown in Figure 37 can be generally related to the stability map shown in Figure 33c. If the model parameters could be used to accurately capture the nature of θ′ interfacial energy and Cu diffusivity in 319, it would be expected to correspond to a simulated alloy in the regime of instability shown in the bottom of

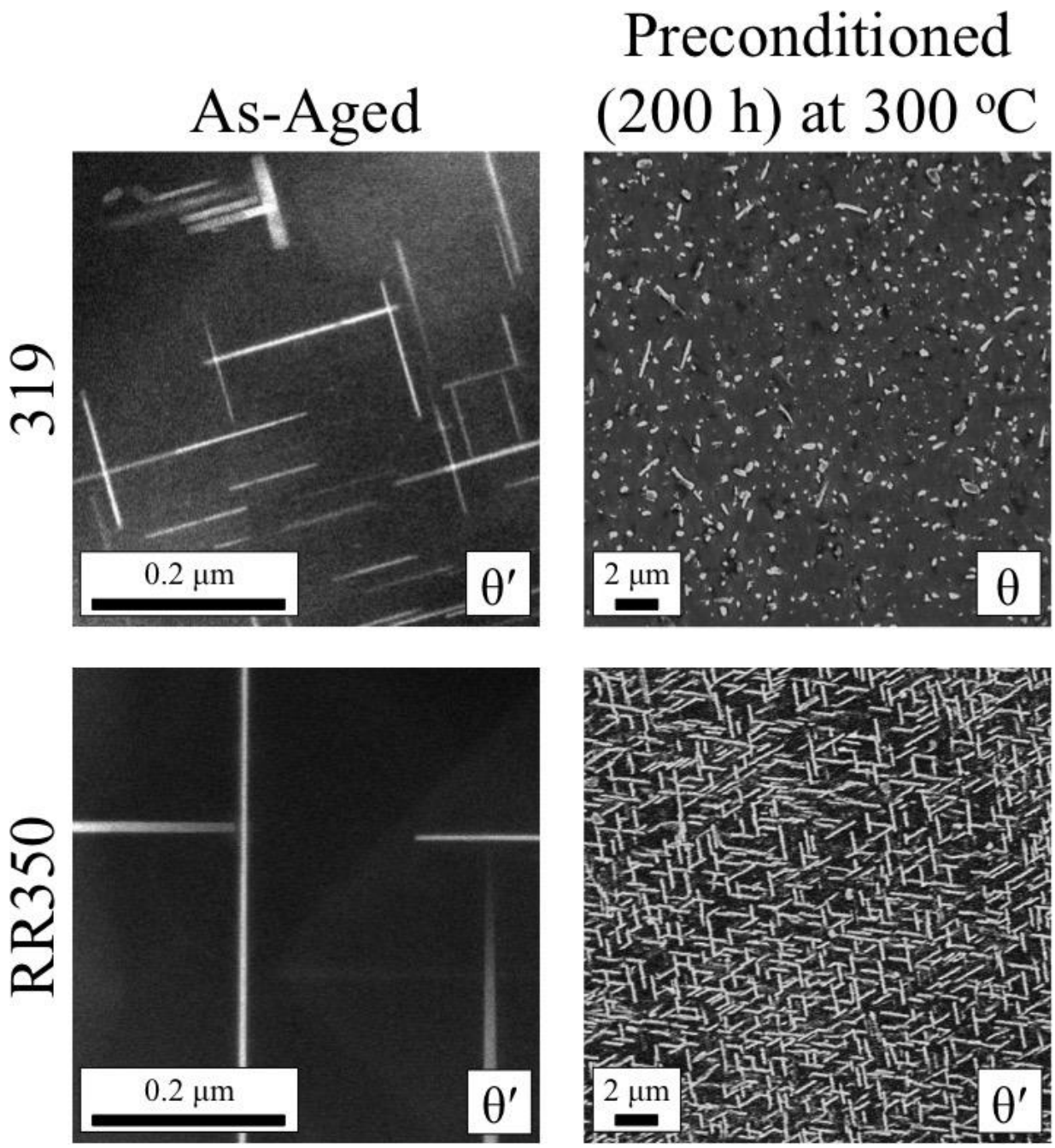

Figure 37. The microstructural evolution that takes place in 319 (a conventional alloy) and RR350 (an alloy with improved thermal stability) when as-aged microstructures are held at 300 °C for 200 hours. 319 shows substantial coarsening of θ′ precipitates as well as phase transformation of θ′ into θ. Meanwhile, θ′ precipitates in RR350 retain their as-aged morphology at 300 °C. The as-aged micrographs were collected with HAADF, the preconditioned micrographs with SEM.

Figure 33c. A simulated alloy which recreates RR350, meanwhile, would be located somewhere in the regime of stability in Figure 33c, as it is thermally stable at 300 ˚C. At 400 ˚C, however, RR350 precipitates are not thermally stable[14], so the simulated alloy recreating RR350 must also be located outside the regime of stability shown in Figure 33d.

The discussion above highlights the challenge of designing a θ′ strengthened aluminum alloy that is thermally stable at 400 ˚C. At the time of this study, no precipitate strengthened Al-Cu alloy has demonstrated extended microstructural stability at this temperature. Referring to Figure 33, the regime of stability at 400 ˚C is much more limited than at 300 ˚C, and appears to exclude even novel alloys with improved thermal stability . Present results suggest that new alloy design strategies will be necessary to address this challenge. While a kinetic stabilization mechanism such as solute drag or a diffusion barrier at the θ′ interface might be adequate to produce the 300 ˚C capable alloys that have been observed , the introduction of a synergistic thermodynamic mechanism which can effectively reduce interfacial energy will likely be necessary to stabilize the Al-Cu microstructure at 400 ˚C.

In addition to providing insight into how solute segregation driven thermal stabilization mechanisms might operate in the Al-Cu system, these results indicate the importance of kinetic considerations in phase field modeling of the Al-Cu system. Generally speaking, the aspect ratio of θ′ particles increases during aging as radial growth outpaces particle thickening, reaches a maximum in the as-aged state, and then decreases as particles continue to thicken without mean diameter growth in the process of coarsening [46, 67]. Experimental observations suggest that, with the exception of very small particles, θ′ evolves into θ before it attains the equilibrium aspect ratio (reported as 2-5) [1, 28, 30, 33, 67, 68]. Thus, thermodynamic equilibrium conditions do not offer a complete description of microstructural evolution and the ability to quantify particle

coarsening kinetics enhances the utility of present generation phase field models for the Al-Cu system.

4.4. Conclusions

The thermal stability of the α/θ′ microstructure in Al-Cu alloys was studied using a combination of phase field simulations and experimental observations. Simulations were carried out using the MOOSE phase field module, and experimental observations were made by exposing two different θ′ strengthened alloys to elevated temperatures for 200 hours. In agreement with the experimental results, the phase field simulations predicted that strengthening θ′ precipitates are relatively stable at temperatures of 200 °C and below in unmodified Al-Cu alloys. At 300 °C and above, the α/θ′ microstructure is thermally destabilized, and rapid θ′ coarsening and shape evolution take place. The rate of shape evolution predicted by phase field simulations was similar to that observed experimentally. In order to predict the onset of detrimental θ′ to θ transformation, a critical θ′ aspect ratio criterion was proposed. Using this criterion, the phase field simulations accurately predicted the time required for the onset of θ formation in a binary Al-Cu alloy as a function of temperature. The phase field simulations also predicted that thermodynamic and/or kinetic modifications to a simulated alloy can lead to microstructural stability at higher temperatures.

The mobility of Cu in the α/θ′ microstructure was shown to be the dominant factor in determining its morphological stability at 300 °C. Phase field simulations predict that a reduction in effective Cu diffusivity is adequate to thermally stabilize the α/θ′ microstructure at this temperature. At 400 °C, however, significant modification to both Cu mobility and interfacial energy of θ′ particles is required to effectively stabilize the microstructure. These predictions help explain the thermal stability of recently reported Al-Cu-Mn-Zr alloys, whose as-aged microstructure is coarsening

resistant at 300 ^{o}C but undergoes substantial degradation at 400 ^{o}C.

Finally, these 300 ^{o}C and 400 ^{o}C phase field predictions were compared to predictions made by an analytical model for θ′ aspect ratio evolution reported previously. The analytical model agreed on the effect of reducing effective Cu diffusivity, but was much less sensitive to interfacial energy reduction compared to the phase field simulations. This discrepancy suggests that geometric effects such as particle curvature and particle volume change, as well as interactive effects between growing and shrinking particles that occur during coarsening, influence θ′ precipitate shape evolution. Such effects are difficult to capture in an analytical model of a single particle but can be evaluated using phase field simulations.

Chapter 5

Mechanisms for Stabilizing θ′(Al_2Cu) Precipitates at Elevated Temperatures Investigated with Phase Field Modeling

This chapter is revised based on a published journal article with Patrick Shower as lead author:

P. Shower, J. Morris, D. Shin, B. Radhakrishnan, J. Poplawsky, A. Shyam, Mechanisms for stabilizing θ′(Al_2Cu) precipitates at elevated temperatures investigated with Phase Field modeling, Materialia (2019) 100335.

My primary contributions to this paper include (i) objectives and design of study (ii) mathematically defining each of the four stabilization mechanisms studied (iii) developing and running phase field simulations for θ′ evolution (iv) literature review (v) most of the writing.

Abstract

While most Al-Cu and Al-Si-Cu alloys strengthened by the metastable θ′ phase exhibit extensive microstructural degradation above 200 ˚C, recent experimental work has demonstrated that θ′ precipitates can be stabilized to 350 ˚C by microalloying additions of Mn and Zr, resulting in improved mechanical properties at elevated temperatures. The present work utilizes phase field modeling to study the relationship between microalloying solute elements and the coarsening resistance of θ′. Simulations are designed to parse out the relative influence of various stabilization mechanisms on microstructural evolution of θ′ precipitates at elevated temperatures. Specifically, a ternary alloying element is added to a virtual microstructure to study the operation and effectiveness of stabilization mechanisms including solute drag, diffusion barriers, interfacial energy reduction, and lattice strain modification. Simulation results are compared with atom probe tomography observations. The simulations rationalize experimental observations of microstructural evolution and solute segregation in Al-Cu-Mn-Zr alloys, and reveal the interlinked thermodynamic and kinetic mechanisms that determine the elevated temperature stability of θ′ precipitates.

5.1. Introduction

Many critical components of modern internal combustion engines (ICE's) are made from cast aluminum alloys, and one of the fundamental factors limiting the design space of these engines is the thermal stability of these alloys' as-aged microstructures [2, 6, 7, 14]. Al-Cu and Al-Si-Cu are common alloy systems in ICE applications; for these alloys, θ′ (Al_2Cu) precipitates are the primary strengthening phase [1, 7]. In conventional alloys, θ′ particles undergo rapid coarsening and transformation into the equilibrium θ phase above 200 ˚C, leading to deteriorated mechanical properties [6, 7]. This susceptibility to thermal softening determines the operating temperature and physical dimensions of powertrain components, and ultimately imposes an upper bound for an ICE's energy efficiency [2, 5, 8, 163]. Recent developments have shown that θ′-strengthened alloys microalloyed with Mn and Zr (termed *ACMZ* alloys) can maintain microstructural stability at temperatures up to 350 ˚C [14]. These alloying elements segregate to the interfaces of θ′, and may increase its thermal stability by reducing the thermodynamic driving force for microstructural evolution [118], impeding the kinetics of such evolution [24, 164], or both [30, 119, 165]. The increased thermal stability of θ′ improves the alloy's creep resistance [34], elevated temperature yield strength [42], and room temperature hardness after prolonged thermal exposure [14].

The present work develops an understanding of the physical mechanism(s) which may contribute to the thermal stabilization phenomenon in ACMZ alloys, using a phase field modeling approach. Such an understanding provides a promising avenue for further development of cast aluminum alloys that maintain microstructural stability to even higher homologous temperatures. In theory, the thermal stability of precipitates in a microstructure may be improved by modifying the thermodynamic and/or kinetic characteristics that control their evolution. In the case of θ′ precipitates undergoing coarsening, the primary thermodynamic driving force is interfacial energy

(both structural and chemical) [30] and the kinetics are limited by the diffusion of Cu atoms [39]. Recent work [119] has used a parametric phase field study to evaluate whether the stabilization mechanism(s) observed in ACMZ alloys are more likely to be thermodynamic or kinetic in nature. The approach used high-throughput phase field simulations to determine the extent of interfacial energy reduction (thermodynamic), and Cu mobility reduction (kinetic) required to recreate the observed high temperature stability in a virtual microstructure. It was shown that the virtual microstructure could be thermally stabilized at temperatures of 200 ˚C to 400 ˚C given adequate modification. Specifically, it was demonstrated that moderate kinetic modification is sufficient to achieve microstructural stability up to 300 ˚C, but additional thermodynamic modification becomes necessary for microstructural stabilization at 400 ˚C.

Practically speaking, there are multiple mechanisms which modify the thermodynamics and kinetics of particle evolution, and such modifications depend on the alloying element(s) present. The objective of the present work is to simulate the addition of ternary alloying elements to an Al-Cu microstructure and study the effects of the alloying addition. The simulations are performed to understand the mechanism(s) by which solute segregation to the interface of θ′ precipitates can lead to improved coarsening resistance. These simulations capture solute segregation to θ′ interfaces explicitly, illustrating the mechanisms by which segregation can affect interfacial energy and coarsening kinetics. These simulations provide two principal scientific advancements:

- The simulations predict the solute segregation profiles at the α/θ′ interface produced by each stabilization mechanism. The simulated segregation profiles are compared directly to experimental segregation profiles observed for various elements using atom probe tomography (APT). This comparison explains the distinct segregation profiles around θ′ precipitates observed for different alloying elements. The simulated segregation profiles depend both on the

thermodynamic interactions of the solute with the interface, and the kinetics associated with precipitate coarsening and with solute mobility, which may contribute significantly, for example, to the behavior of slow-diffusing elements such as Mn and Zr in the Al matrix.

- The relative effectiveness of each mechanism in reducing the precipitate coarsening rate (acting both individually and in concert with other mechanisms) is quantified. This quantification allows us to evaluate which mechanism or combination of mechanisms can most readily account for the improved coarsening resistance of θ′ particles observed in some Al-Cu alloys.

These insights are of interest in the ACMZ system, and also in Al-Cu-(Sc, Si, Ag) systems where extensive solute segregation occurs [14, 121, 126] and Al-Cu-(Sn, Cd, In, Mg, Au) where interactions between the θ′ interface and clusters of solute atoms are known to exert significant influence in the early stages of aging [116, 120, 149, 166].

Phase field modeling was chosen as an approach that may directly examine microstructural evolution, accounting for kinetics, thermodynamics, and strain effects, including the effects of solute segregation to the interfaces, as well as the anisotropic properties of the θ′/α-Al interface. We are interested in studying how microalloying elements segregate to the interface of coarsening θ′ precipitates in a virtual microstructure, and how this segregation might affect microstructural evolution. There are three key physical aspects of the coarsening process, and a solute element might affect any of them:

- The thermodynamic driving force for the coarsening of θ′ precipitates in an Al-Cu microstructure is the reduction in total interfacial energy, as well as longer-ranged strain energy arising from the precipitates.
- Coarsening takes place *via* the movement of Cu atoms from smaller θ′ precipitates to larger θ′ precipitates.

- As this exchange of Cu atoms proceeds, the larger θ′ precipitates become larger *via* the nucleation and growth of ledges which accommodate the incoming Cu atoms and advance the interface of θ′ into the α-Al matrix, while the smaller θ′ precipitates shrink *via* the retreat of ledges.

In this work, we use phase field simulations to introduce virtual solute elements that can specifically interact with each of these three physical aspects of coarsening. Rather than simulating actual elements like Mn and Zr, we attempt to capture the salient *characteristics* of elements that might interact with a coarsening microstructure. These include (a) virtual solute elements that reduce excess energy at the interface of θ′ precipitates, which decreases the driving force for coarsening and introduces a driving force for solute segregation, (b) virtual solute elements with a volume misfit in the α-Al matrix, which can interact with the coherency strains present around a virtual θ′ particle, (c) virtual solute elements that reduce the mobility of Cu in the virtual α-Al matrix, affecting the rate of Cu exchange between smaller and larger θ′ particles, and (d) slow-diffusing solute elements that must be displaced by the advancing interface of a virtual θ′ precipitate, recreating the essential nature of solute drag without explicitly simulating the atomic-level interactions between solute atoms and ledge dislocations which are known to occur in physical microstructures. In the present simulations, we evaluate how each of these four characteristics (a-d) affect the segregation of virtual solute elements and the coarsening of virtual θ′ particles.

These simulations demonstrate that the contributions from thermodynamic and kinetic stabilization mechanisms can be delineated using a systematic phase field approach in a way that experiment alone does not allow. The paper is organized as follows: In Section 5.2, we present both modeling and experimental methods. Section 5.3 presents the main results of the phase field model. It is demonstrated that a combination of stabilization mechanisms is necessary to maximize

stability, but that some combinations of mechanisms compete with each other. It is further shown that phase field simulations predict realistic solute segregation profiles. These time-dependent segregation profiles can be used to explain coarsening resistance of θ′ particles, based on their interaction with solute elements. Section 5.4 discusses these results in light of prior work.

5.2. Methods and Modeling Rationale

In this work, we develop phase field simulations to study how key thermodynamic and kinetic characteristics of solute elements in an Al-Cu microstructure effect the solutes' interaction with coarsening θ′ precipitates. As detailed in the rest of Section 5.2, we base these characteristics on our available knowledge of actual solute elements from literature and first principles calculations. Thus, the present simulation results offer insight on the observed coarsening resistance of the θ′ phase in certain alloys as well as mechanisms that influence the segregation profiles of various solute elements around θ′ particles. However, they do not offer any new information on how solute elements interact with vacancies, dislocations, or discrete interface ledges. These features are not captured explicitly in the diffuse interface phase field model, and there is an inherent assumption that their behavior is "blended out" over the length and time scales of interest by the selection of appropriate model parameters.

In Section 5.2.1 below, we present the baseline model for the evolution of the θ′ precipitates. Section 5.2.2 describes the broad strategy of relating the phase field simulations to microstructural stability. Section 5.2.3 describes the specifics of how solute effects were implemented into the phase field model, and how relevant parameters are chosen. Section 5.2.4 describes the alloy, heat treatment, and atom probe methods used to compare experimental solute segregation profiles with the simulations.

5.2.1. *Baseline Model*

The Multiphysics Object-Oriented Simulation Environment (MOOSE) framework [138] was used to construct a two-dimensional simulation of the Al-Cu microstructure as described in a previous publication [119]. In prior work, this simulation reproduced coarsening phenomena observed in experimental microstructures, and accurately predicted microstructural evolution rates at temperatures between 100 ˚C and 400 ˚C [12]. The same simulation framework is used in the present work with some modifications to explicitly simulate a set of ternary alloys with composition Al–4%Cu–0.25%(solute) (all percentages refer to atom %), where the solute is chosen to mimic the effects of the addition of Mn or Zr. The mathematical model upon which the simulation is based is summarized briefly here, and the incorporation of a ternary alloying element and the associated stabilization mechanisms are described in Section 5.2.3.

In phase field simulations, microstructural evolution proceeds in such a way as to minimize the total energy of the system while being constrained by physical laws, a premise defined by the Allen-Cahn and Cahn-Hilliard formulations [143]. The total energy of the system depends on the bulk free energy of each phase, elastic lattice strain energy, and gradient energy that is associated with compositional gradients and phase interfaces. These, in turn, depend on the physical and chemical descriptors of each phase and element. The formulae used in the present phase field simulations are summarized in Table 17, followed by definitions of each variable. The values of function parameters are given in the supplementary file.

Table 17. Formulas implemented in the present phase field model. A more thorough description of the model is given in Section 4.2.

Name	Function	Purpose
Cahn-Hilliard formulation	$\frac{\partial x_{Cu}}{\partial t} = \nabla \cdot M_{Cu} \nabla \frac{\delta F}{\delta x_{Cu}}$	Dictates how local composition evolves over time.
Allen-Cahn formulation	$\frac{\partial \eta}{\partial t} = -L \frac{\delta F}{\delta \eta}$	Dictates the formation and dissolution of θ′ over time.
Total Free Energy	$F = \int_{Volume} \left(f_{bulk} + f_{gradient} + f_{lattice\ strain}\right) d(Volume)$	Sums all components of the system's free energy.
Bulk Free Energy	$f_{bulk} = \left(f_{\theta'}(x_{Cu}) + f_{\theta'}(x_{sol})\right) \cdot g(\eta) + \left(f_{\alpha}(x_{Cu}) + f_{\alpha}(x_{sol})\right) \cdot \left(1 - g(\eta)\right)$	Determines coarse-grained free energy as a function of phase and composition.
Switching Function	$g(\eta) = 3 \cdot \eta^2 - 2 \cdot \eta^3$	Interpolates between α and θ′ free energy functions.
Gradient Free Energy	$f_{gradient} = \frac{\kappa_\eta}{2} \cdot \lvert\nabla_\eta\rvert^2 + \frac{\kappa_{Cu}}{2} \cdot \lvert\nabla_{x_{Cu}}\rvert^2 + \frac{\kappa_{Sol}}{2} \cdot \lvert\nabla_{x_{sol}}\rvert^2 + p(\eta) \cdot f(x_{sol})$	Free energy associated with particle interfaces and compositional gradients.
Interface identifying function	$p(\eta) = \frac{\eta^8 \cdot (1-\eta)^8}{.5^8 \cdot (1-.5)^8}$	Equals 1 at the θ′ interface and 0 elsewhere.
Interfacial Energy	$\gamma = 2 \cdot \int_{x_{Cu,\alpha}}^{x_{Cu,\theta'}} [\kappa_{Cu} \cdot \Delta f_{bulk}(x_{Cu})]^{\frac{1}{2}} \cdot \left[1 + \frac{\kappa_\eta}{\kappa_{x_{Cu}}} \cdot \left(\frac{d\eta}{dx_{Cu}}\right)^2\right]^{\frac{1}{2}} dx_{Cu}$	Relates physical interfacial energy to model parameters.
Gradient Energy parameter profile	$\kappa_\eta = 1.845 \cdot \cos(4\psi + 180^o) + 3.081 \cdot \sin(2\psi + 90^o) + 9.055$	Accounts for anisotropic interfacial energy.
Copper Mobility	$M_{o,Cu} = D_{o,Cu} \cdot e^{-\frac{Q_{diff,Cu}}{R \cdot T}} \cdot \{X_{Cu} - (X_{Cu})^2\}/(R \cdot T)$	Determines *baseline* Copper mobility as a function of temperature.
Simulation Time	$t^* = L \cdot \lvert\Delta f\rvert \cdot t$	Relates physical time to simulation time.

x_{Cu} ≡ local mole fraction of Cu †

η ≡ order parameter (0 for α, 1 for θ′) †

M_{Cu} ≡ mobility of copper †

L ≡ kinetic prefactor for θ′ formation/dissolution †

F ≡ total energy of the system †

f_{bulk} ≡ local bulk free energy

$f_{gradient}$ ≡ local gradient energy

$f_{lattice\ strain}$ ≡ local elastic lattice strain energy †

$f(x_{sol})$ ≡ change in $f_{gradient}$ due to solute segregation

$f_{\alpha}(x_{sol})$ ≡ ideal solution free energy of solute in α-Al †

$f_{\theta'}(x_{Cu})$ ≡ free energy of θ′ phase †

$f_{\alpha}(x_{Cu})$ ≡ free energy of α phase †

κ_{η} ≡ order parameter gradient coefficient

κ_{Cu} ≡ compositional gradient coefficient †

γ ≡ interfacial energy of θ′ precipitates

$\Delta f_{bulk}(c)$ ≡ energy difference between f_{bulk} and a common tangent construction

ψ ≡ angle of the interface normal relative to that of the semi-coherent interface

$D_{o,Cu}$ ≡ diffusional prefactor †

$h(x_{sol})$ ≡ change of M_{Cu} in the presence of solute atoms †

$Q_{diff,Cu}$ ≡ activation energy for tracer diffusion of Cu in pure Al

R ≡ ideal gas constant

T ≡ absolute temperature

X_{Cu} ≡ overall molar composition of Cu in the alloy.

x_{sol} ≡ local mole fraction of generic ternary solute element

t^* ≡ simulated time

t ≡ physical time

$|\Delta f|$ ≡ maximum value of $\Delta f_{bulk}(c)$.

$f_{\theta'}(x_{sol})$ ≡ energy penalty function that makes the solute element insoluble in θ′.

† Parameter/Function value given in the supplementary file

The simulations incorporated the two primary phases found in the bulk as-aged microstructure of commercial Al-Cu(-Si) alloys: a matrix of α-Al (FCC solid solution) populated by the metastable θ′ phase (tetragonal Al_2Cu precipitates). Each phase was defined using unique physical and chemical descriptors including their bulk free energy (as a function of temperature and composition), lattice constants, and temperature-dependent stiffness tensors. An anisotropic θ′ interfacial energy as well as the temperature-dependent mobility of Cu were also incorporated. Additionally, a ternary alloying element was included with variable mobility, atomic radius misfit, energetic interactions with the θ′ interface, and influence on the mobility of Cu.

In this study, the bulk free energy ($\boldsymbol{f_{bulk}}$) of each phase was derived from ThermoCalc data. The gradient free energy ($\boldsymbol{f_{gradient}}$) was derived from Density Functional Theory (DFT) calculations [14, 119], and reproduced the calculated anisotropic interfacial free energies and the calculated segregation energies of the solute atoms to the interface [118]. The elastic lattice strain energy ($\boldsymbol{f_{lattice\ strain}}$) was calculated within the MOOSE framework using the microelasticity theory of Khachaturyan *et al.* [140, 141, 154] along with lattice parameter and stiffness tensor data taken from the literature [95, 132, 133]. Parameters related to $\boldsymbol{f_{bulk}}$ and $\boldsymbol{f_{lattice\ strain}}$ were calculated discretely at 300 ˚C and 400 ˚C. The terms describing the gradient energies were assumed to be invariant with temperature and particle size, as described in Chapter 4.

5.2.2. *Modeling Objective and Rationale*

The objective of this work is to determine the influence of ternary alloying elements on the stability of θ′ precipitates at elevated temperatures using phase field simulations, particularly the potentially synergistic or competing thermal stabilization mechanisms associated with a ternary solute element. We simulate the coarsening of a virtual microstructure, wherein larger θ′ precipitates are

allowed to grow in size as smaller θ′ precipitates shrink and eventually disappear (details of the virtual microstructure given in Section 5.3.1). This process, known as Ostwald ripening, is central to the complex evolution of a coarsening microstructure. In our phase field simulations, we measure the time required for the complete consumption and disappearance of the smaller θ′ precipitates and designate it the "duration of stability". This metric is a simple analog to coarsening rate, and it facilitates quantitative comparisons between simulations. When a ternary alloying element is added, the "duration of stability" is changed, allowing us to evaluate the influence of alloying on coarsening resistance and analyze the kinetics of the complicated coarsening process. In addition to predicting coarsening resistance, the phase field simulations allow us to study the time-dependent segregation profiles that arise depending on the characteristics of the virtual alloying element (numerical description and implementation of virtual alloying elements detailed in Section 5.2.3).

Coarsening resistance, quantified using the "duration of stability" metric defined above, was the focus of this study because of its bearing on mechanical properties. As larger θ′ precipitates grow at the expense of smaller precipitates, the number density of strengthening particles is reduced and the alloy's mechanical properties deteriorate [1, 6, 7, 34, 42]. The coarsening of θ′ precipitates is also associated with detrimental θ′→ θ transformation. The θ′ phase is metastable, and larger θ′ precipitates have a greater driving force to transform into the deleterious, equilibrium θ phase (due to the fact that θ particles have a lower volumetric free energy and a higher average interfacial energy than θ′ particles) [30, 38, 39].

Given the detrimental impact of θ′ coarsening and eventual θ′→ θ transformation, any mechanisms which can effectively reduce the coarsening rate of θ′ (*i.e.* increase the duration of stability) are relevant for the purpose of alloy design. The present work explores the influence of specific

thermodynamic and kinetic stabilization mechanisms on microstructural evolution. The mechanisms examined in this study are all tied to a ternary alloying element in the α/θ′ microstructure, motivated by the experimental observation that segregation of Mn and Zr to the surface of θ′ precipitates is associated with a substantial improvement in high temperature microstructural stability [14]. As shown in Section 5.3.3 below, very little Mn or Zr solute is found within the θ′ precipitates, so partitioning of solutes is assumed to have no effect on the volumetric terms associated with the θ′→ θ transformation. This is also consistent with prior DFT calculations [14].

The thermal stabilization mechanisms considered in this study include the formation of a diffusion barrier around θ′, solute drag at the particle interface, a reduction in interfacial energy, and modifications to the strain field around θ′ particles. Depending on the characteristics of the ternary alloying element, these mechanisms can act individually or in concert. The methods used to implement these mechanisms in a phase field model and determine their impact on coarsening rate are discussed in Section 5.2.3. In each case, the objective was to determine the greatest magnitude of thermal stabilization that could be reasonably expected as a result of individual or combined mechanisms. Therefore, each stabilization mechanism was simulated with the intent of creating a "best case scenario" for that mechanism's effectiveness, based on the characteristics of Mn and Zr, which are known to have a significant stabilizing effect on the Al-Cu microstructure at elevated temperatures. To frame this approach in a different light, it is known that Mn and Zr exert a stabilizing effect on the Al-Cu microstructure, and these simulations are used to determine which characteristics of Mn and Zr are most likely to account for this stabilization.

5.2.3. *Implementation of Solute-driven Stabilization Mechanisms*

In order to study the effect of the four thermal stabilization mechanisms of interest (solute drag, a diffusion barrier, lattice strain modification and interfacial energy reduction) a generic solute element with variable properties was explicitly included in the simulated alloys at a concentration of 0.25 atomic %. At the beginning of the simulations, the solute is uniformly distributed throughout the matrix. Specific solute characteristics associated with each thermal stabilization mechanism were identified, so that by altering these characteristics, each mechanism could be turned "on" or "off" from one simulation to the next for the purpose of studying its effects. These mechanism-characteristic pairs are listed in Table 18.

Some solute characteristics were constant across simulations. The solute was made insoluble in θ′, the free energy of mixing of the solute in α was accounted for by assuming an ideal solid solution [30], and the value of $\kappa_{sol}$was taken to be 1% of κ_{Cu} to minimize the energy contribution of its concentration gradient and allow for a narrow segregation profile, which has been observed in experiments [14, 118, 167, 168]. While some of these characteristics are a simplification (for instance, certain elements such as Si and Mg are soluble in θ′) or are not derived from first principles, they are consistent with experimental observations in the ACMZ alloy system [14].

The four solute characteristics listed in Table 18 are all treated independently of one another in the simulations. Therefore, the ternary solute element in the simulated Al–4%Cu–0.25% (solute) alloy (atomic %) could have any combination of these four characteristics, for 16 different combinations in total (four independent mechanisms, each either "on" or "off", leads to 2^4 = 16 possible combinations). Each combination of characteristics/mechanisms resulted in a simulated alloy with distinct behavior. Thus, 16 different simulated alloys were analyzed in order to understand their microstructural evolution at 300 ˚C and 400 ˚C. This approach allows us to evaluate each set of

Table 18. List of thermal stabilization mechanisms considered in this study, along with the characteristics of a solute element that are responsible for each stabilization mechanism.

Thermal Stabilization mechanism	Solute characteristic
Diffusion Barrier	M_{Cu} is a function of local solute concentration.
Solute Drag	Solute has low mobility.
Interfacial energy reduction	$f_{gradient}$ is a function of local solute concentration.
Lattice strain modification	Solute has a size misfit in the α-Al matrix.

stabilization mechanisms for their impact on coarsening resistance and solute segregation. The incorporation of each mechanism is expanded upon below.

A ***diffusion barrier*** for Cu was introduced by making M_{Cu} a function of solute concentration rather than a global constant. To find appropriate input parameters, DICTRA software was used to determine Cu's mobility as a function of local composition as well as temperature. Because extensive thermal stabilization of θ′ particles has been observed in Al-Cu alloys containing Mn and Zr, the diffusivity of Cu in the presence of these alloying additions was of interest. Mn and Zr both have low solubility in the bulk of α-Al (<0.9 atomic % [1]), but local concentrations as high as 4 atomic % at the θ′ interface have been reported at 300 °C [14]. Diffusivity calculations in DICTRA were carried out for an Al-0.25 atomic % Cu solid solution (a typical composition of the α-Al matrix [95]) with Mn and Zr additions up to 4 atomic %.

According to these calculations, the presence of 4 atomic % Mn in solution is expected to reduce the diffusivity of Cu by 40% to 50% at a given temperature, while the addition of Zr has little effect on Cu mobility (although the latter may be due to a limited amount of available data). Therefore, in order to produce a reasonably realistic simulation of a diffusion barrier mechanism, the relationship between Cu diffusivity and Mn content was used. Specifically, the mobility of Cu in the virtual matrix was calculated using a variable diffusivity value which was fit to the DICTRA calculations. This resulted in two second order polynomial functions for $M_{Cu,}$, one at each temperature (Eqs. 27a and 27b).

$$M_{Cu,300\,^{\circ}\mathrm{C}}\left[\frac{nm^2}{sec\left[\frac{meV}{nm^3}\right]}\right] = M_{o,Cu,300\,^{\circ}\mathrm{C}} + 203 \cdot x_{sol}^2 - 15.13 \cdot x_{sol} \tag{27a}$$

$$M_{Cu,400\,^{\circ}\mathrm{C}}\left[\frac{nm^2}{sec\left[\frac{meV}{nm^3}\right]}\right] = M_{o,Cu,400\,^{\circ}\mathrm{C}} + 12810 \cdot x_{sol}^2 - 990.2 \cdot x_{sol} \tag{27b}$$

When the diffusion barrier mechanism was not active, the x_{sol} terms were removed from Eqs. 1a

and 1b and M_{Cu} was solely a function of temperature.

A ***solute drag*** mechanism was introduced by giving the ternary solute element a mobility of 0.1% $M_{o,Cu}$ at the temperature being simulated. Through iterative testing, the 0.1% mobility ratio was determined to be effective in impeding the kinetics of coarsening through drag. Virtual solutes with a lower mobility than 0.1% of $M_{o,Cu}$ generally were not able to segregate to the θ′ interface quickly enough to influence coarsening kinetics. On the other hand, virtual solutes with a mobility greater than 0.1% of $M_{o,Cu}$ provided only modest kinetic inhibition to the motion of the θ′ interface. The 0.1% mobility ratio is also realistic, as there are several elements including Sc, Er, and Fe whose mobility in Al is similar to this value at 300 ˚C and 400 ˚C [23, 29, 164]. Furthermore, Sc has been shown to segregate to the α/θ′ interface and reduce the rate of θ′ particle growth [126, 139].

An ***interfacial energy reduction*** mechanism, associated with solute segregation to the interface, was introduced using the $p(\eta) \cdot f(x_{sol})$ term in the formula for $f_{gradient}$ (Table 1). Specifically, the interface identifying function was chosen as Eq. 28.

$$p(\eta) = \frac{\eta^8 \cdot (1-\eta)^8}{0.5^8 \cdot (1-0.5)^8} \tag{28}$$

Note that $p(\eta)$ has a value of 1 at the interface of θ′ (corresponding to η=0.5) and decays to zero in the bulk of the α phase (η=0) and the θ′ phase (η=1). The gradient energy was reduced in the vicinity of the interface, according to the solute concentration. This is defined in Eq. 29.

$$f(x_{sol}) = \tag{29}$$

$$-3.4482 \left[\frac{meV}{nm^3}\right] \cdot (-1.749 \cdot 10^8 \cdot {x_{sol}}^6 + 3.828 \cdot 10^7 \cdot {x_{sol}}^5$$

$$-3.5862 \cdot 10^6 \cdot {x_{sol}}^4 + 1.904 \cdot 10^4 \cdot {x_{sol}}^3$$

$$-6.227 \cdot 10^3 \cdot {x_{sol}}^2 + 1.189 \cdot 10^2 \cdot x_{sol})$$

$f(x_{sol})$ was chosen in order to fit a typical interfacial energy reduction due to Mn/Zr segregation predicted by DFT for this system [14, 118]. It provides a broad energy well with a maximum depth of $3.4482 \left[\frac{eV}{nm^3}\right]$, occurring at $x_{sol} = 4\%$ (typical segregation levels reported by Shyam *et al.* [14]), and imposes an energetic penalty for negative values of x_{sol}. Eqs. 28 and 29 are plotted in Figure 38. The incorporation of Eqs. 28 and 29 into the formula for $f_{gradient}$ means that the interfacial energy of θ′ is reduced as the ternary solute elements segregate to the α/θ′ interface (independent of whether the interface is coherent or semi-coherent). Thus, these equations impart a driving force for solute segregation. When the interfacial energy reduction mechanism was not activated, $f(x_{sol})$ was set to zero.

A ***lattice strain modification*** mechanism was introduced using a localized eigenstrain [138, 140, 141, 154] term as a function of a solute element's misfit and concentration at any given mesh point:

$$\varepsilon_{xx}, \varepsilon_{yy} = \sqrt[3]{(1 + x_{sol} \cdot 0.74100 \cdot ((1+\epsilon)^3 - 1))} - 1 \tag{30}$$

The derivation for this equation is provided in Appendix A. The misfit term ϵ is defined as

$$R_{solute} = R_{Al} \cdot (1 + \epsilon) \tag{31}$$

where R is the atomic radius. The implementation of Eqs. 30 and 31 allowed for simulations which demonstrated how a solute element with a size misfit might segregate to the interface of θ′ and affect the local strain field. This phenomenon is of interest for alloy systems like ACMZ, in which the precipitate generates a strain field in the matrix [117, 118]. To a first order approximation, the largest atom in such a system (i.e. Zr in ACMZ), might be expected to exert the most significant

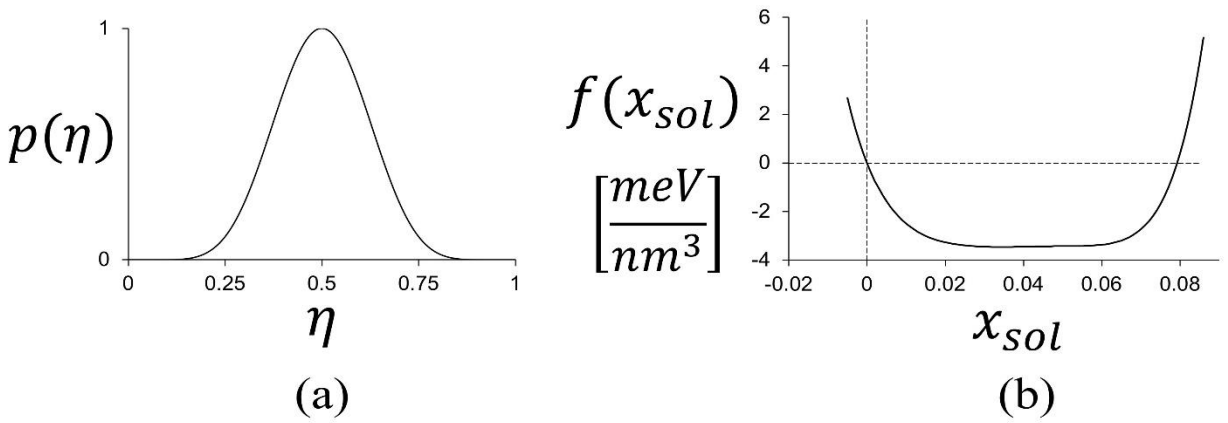

Figure 38. Plots of (a) the interface identifying function (Eq. 26) and (b) the interfacial energy reduction function (Eq. 29). Eq. 28 has a value of 1 at the θ′/α-Al interface and approaches 0 elsewhere. Eq. 29 is an energy well describing a decrease in free energy as a function of solute concentration. The product of Eqs. 28 and 29 imparts a thermodynamic driving force for solute segregations to the θ′/α-Al interface.

influence on the surrounding strain field. In order to gauge what this influence might be, the ϵ value implemented in these simulations was that of Zr (0.746) [169]. When the lattice strain mechanism was not active, ϵ was simply set to zero.

5.2.4. *Atom Probe Tomography*

In order to compare solute segregation profiles predicted by phase field simulations to those that occur experimentally, an ACMZ alloy (designated RR350) preconditioned at 300 ˚C for 200 hours post-aging was analyzed using atom probe tomography (APT) [14] (alloy composition and heat treatment described elsewhere [42]). Preconditioned RR350 samples were fabricated into needle shaped specimens using standard electropolishing methods [170]. The final APT specimens were shaped with annular Ga ion milling using a FEI Nova 200 dual beam scanning electron microscope (SEM) and focused ion beam (FIB). The APT experiment was conducted within a CAMECA LEAP 4000XHR using ~10 ps 355 nm wavelength UV laser pulses with a 50-60 pJ laser pulse energy, a 200 kHz pulse repetition rate, a 30 K specimen temperature, and a 0.5% evaporation rate. The APT results were reconstructed and analyzed using CAMECA's interactive visualization and analysis software (IVAS 3.8) [171].

5.3. Effects of Solutes on Coarsening Resistance of θ′

In this section, we report the outcome of phase field simulations of coarsening θ′ (Al_2Cu) particles in the presence of a ternary alloying element whose characteristics are associated with various stabilization mechanisms, as well as insights these simulations provide. In Section 5.3.1, we describe the virtual microstructure used in the simulations and the metric selected to evaluate coarsening resistance. In Section 5.3.2, we describe how the various stabilization mechanisms affect coarsening resistance in the virtual microstructure. In Section 5.3.3, we relate the

effectiveness of each mechanism to the solute segregation profile it causes, making direct comparison of the segregation profiles predicted by the simulation to experimentally observed segregation in an ACMZ alloy preconditioned at 300 °C from atom probe studies. In Section 5.3.4, we highlight the effects of temperature on the stabilization mechanisms.

5.3.1. *Defining Coarsening Resistance in the Virtual Microstructure*

To examine how a ternary alloying element might influence the coarsening rate of θ′, a simplified, symmetric virtual microstructure was constructed. As shown in Figure 39, this virtual microstructure consisted of four θ′ particles populating a two-dimensional, 100 nm x 100 nm mesh. In reality, θ′ particles are approximately disc shaped, with broad, coherent interfaces forming on the three mutually orthogonal {1 0 0 planes in the α-Al matrix, as shown in the micrograph in Figure 39. To simulate this microstructure in two dimensions, the particles are initially represented as rectangles (*i.e.* discs viewed edge-on) with two perpendicular orientations of their major axes. The particles were 2.8 nm thick, a typical value for precipitates in as-aged Al-Cu and Al-Si-Cu alloys [119]. The microstructure was designed such that the two larger particles (40 nm x 2.8 nm) coarsen at the expense of the two smaller particles (20 nm x 2.8 nm). Simulations were run at either 300 ˚C or 400 ˚C, and the time required for the smaller precipitates to be completely consumed by the coarsening process (see Figure 39) was recorded as the "duration of stability." By avoiding any asymmetry in the distribution of particles, this microstructure allowed the effect of each stabilization mechanism to be more clearly isolated. This strategy has been applied in prior phase field studies to analyze coarsening behavior [158]. Boundary conditions were periodic with respect to all variables. As a result, the geometry of the microstructure was the simplest that ensured each horizontal precipitate interacted with strain and concentration fields caused by

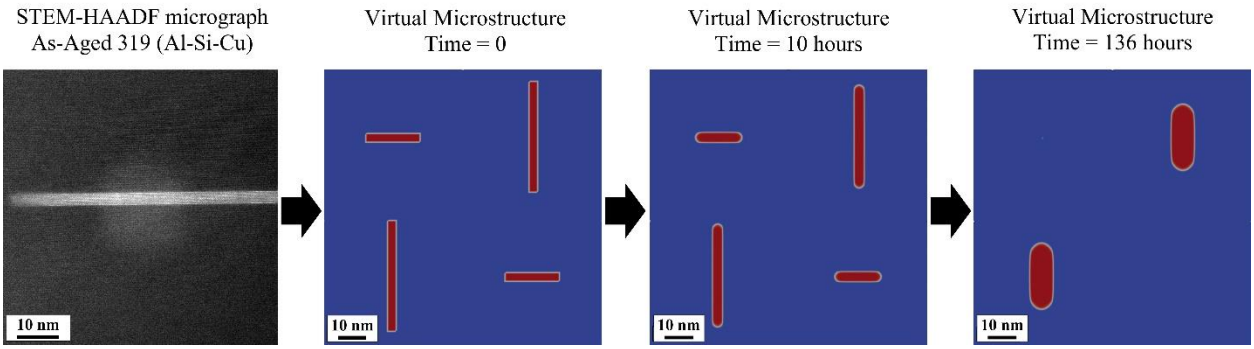

Figure 39. A scanning transmission electron high-angle annular dark field (HAADF) micrograph of an as-aged microstructure of 319 alloy compared to the virtual microstructure used in this study. A baseline Al-Cu simulated alloy evolving at 300 °C is shown. The initial condition is shown at time = 0. Precipitate shape evolution is apparent at time = 10 hours. The complete consumption of smaller particles as larger particles grow is shown at time = 136 hours. In this case, the duration of stability is defined as 136 hours.

adjacent vertical precipitates and vice versa.

5.3.2. *Effect of Individual and Combined Mechanisms on Coarsening Resistance of θ′*

Each of the four stabilization mechanisms studied (interfacial energy reduction, lattice strain modification, solute drag, and a diffusion barrier) change the coarsening resistance of the virtual microstructure. This study was designed to determine which mechanisms and combinations of mechanisms were most effective at improving coarsening resistance (*i.e.* increasing the duration of stability as described in Sections 2.2 and 3.1). Figure 40 compares the effectiveness of these mechanisms, acting individually and in concert. Specifically, the duration of stability added to the virtual microstructure is plotted (relative to a baseline simulation in which no stabilization mechanisms were activated). Each data point represents a simulated alloy in which one or more stabilization mechanisms were activated. Simply put, each data point represents a set of stabilization mechanisms being activated, with a greater y-coordinate value corresponding to greater improvement in coarsening resistance. The color (or colors) of each data point indicate what mechanism (or mechanisms) is (or are) active. For example, the least effective stabilization mechanism at 300 ˚C was solute drag acting in isolation, and the most effective was a combination of solute drag, a diffusion barrier, and interfacial energy reduction. The duration of stability for the baseline simulated alloy was 136 hours at 300 ˚C, and 59 hours at 400 ˚C.

Interfacial energy reduction is the most effective single mechanism at each temperature, adding ~30 hours of stability at 300 °C and ~9 hours at 400 °C. This mechanism has a particularly synergistic effect when combined with a solute drag mechanism: these two mechanisms combined lead to the largest duration of stability at 400 °C, and the second-largest at 300 °C. At 300 °C, these two mechanisms together provide a much higher duration of stability increase than the sum

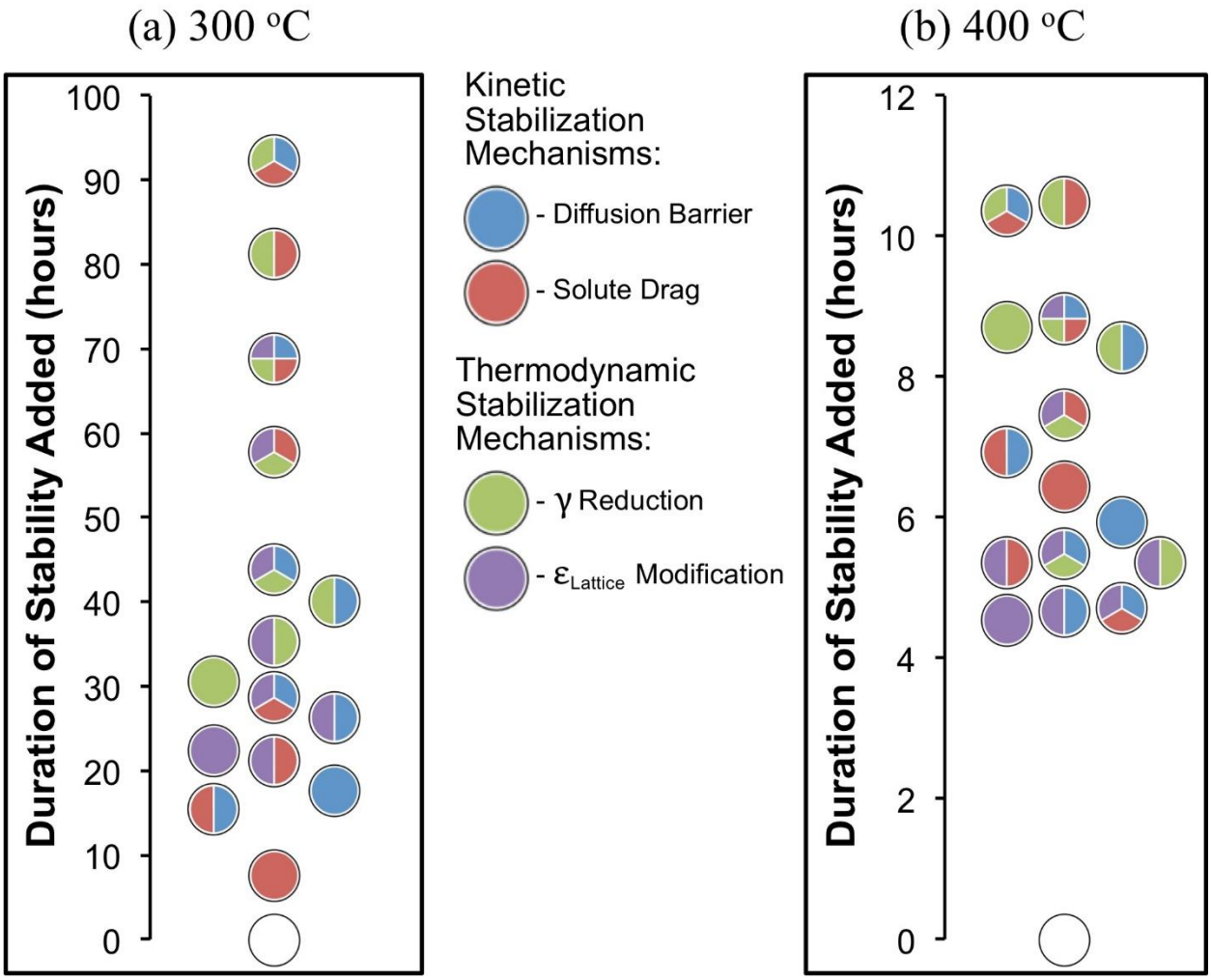

Figure 40. A scanning transmission electron high-angle annular dark field (HAADF) micrograph of an as-aged microstructure of 319 alloy compared to the virtual microstructure used in this study. A baseline Al-Cu simulated alloy evolving at 300 °C is shown. The initial condition is shown at time = 0. Precipitate shape evolution is apparent at time = 10 hours. The complete consumption of smaller particles as larger particles grow is shown at time = 136 hours. In this case, the duration of stability is defined as 136 hours.

of the two individual effects. The further addition of a diffusion barrier (reducing the mobility of Cu) has modest effects at both temperatures. This suggests that, in the presence of substantial solute drag, the diffusion of Cu is no longer a rate-limiting step, even when the diffusion rate of Cu is halved.

When the lattice strain modification mechanism is combined with other mechanisms, it often decreases their effectiveness (*e.g.* the 300 ˚C simulations indicate that a combination of all four stabilization mechanisms was actually ~25% less effective than a combination of all stabilization mechanisms *except for* lattice strain modification). The 400 ˚C results indicate that the effectiveness of the thermal stabilization mechanisms are generally reduced with increasing temperature, although different mechanisms are influenced in different ways. For instance, the effectiveness of the diffusion barrier, interfacial energy reduction, and lattice strain modification mechanisms all drop by more than 65% between 300 ˚C and 400 ˚C, while the effectiveness of the solute drag mechanism is essentially constant.

In order to facilitate interpretation of the multivariate data, a correlation coefficient was calculated for each mechanism. This metric indicates the strength and nature (positive or inverse) of the correlation between a set of independent and dependent variables [172]. In this case, it is a rough indication of how effective each mechanism was at improving the coarsening resistance of the virtual microstructure, both alone and when combined with other mechanisms. The correlation coefficient between the activation of each mechanism and the duration of stability added to the virtual microstructure is shown in Figure 41.

The data shown in Figure 41 indicate that interfacial energy reduction is the most broadly effective stabilization mechanism at both temperatures, and that the effectiveness of thermodynamic mechanisms (lattice strain modification and interfacial energy) increases with temperature relative

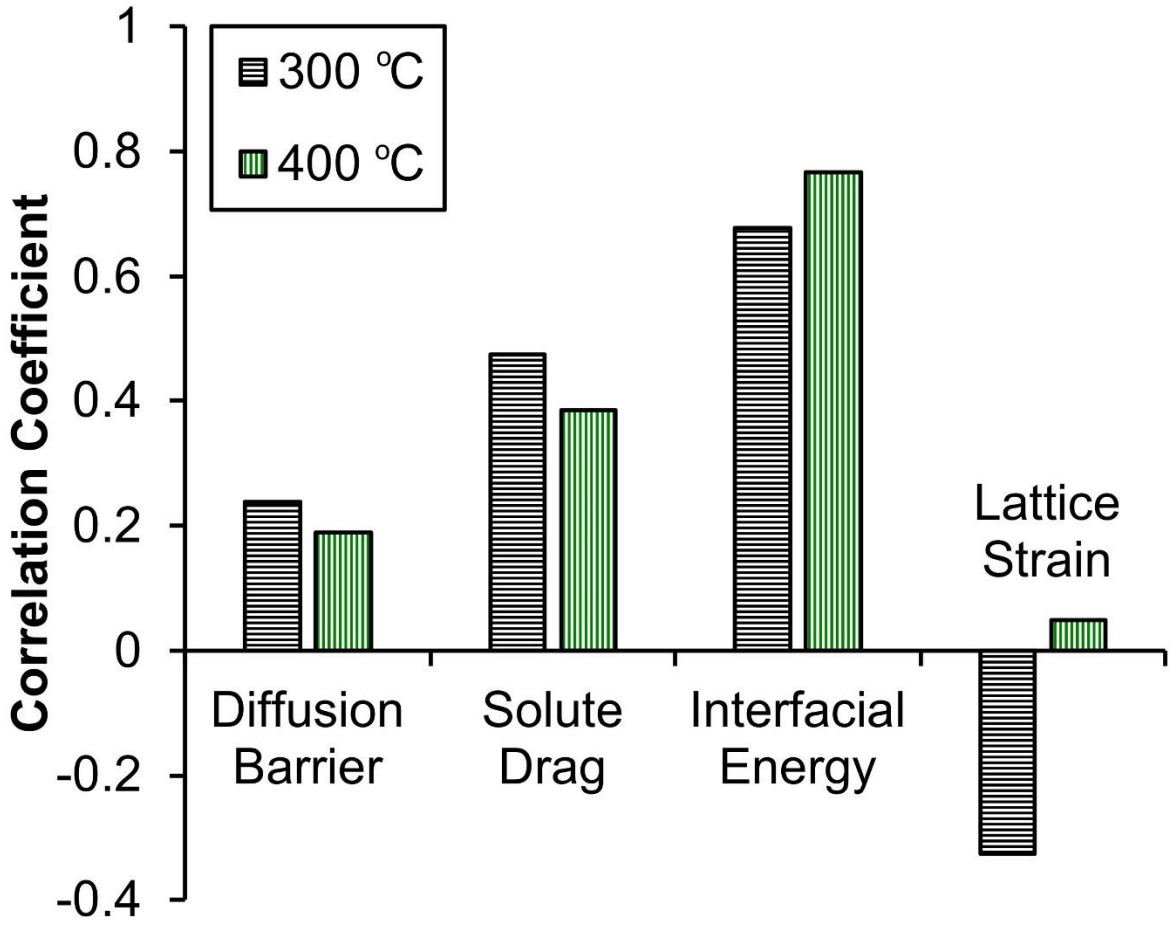

Figure 41. The correlation coefficient between the activation of each mechanism and the duration of stability added to the virtual microstructure. Specifically, the independent variable used was 0 if the mechanism was inactive and 1 in the mechanism was active. The dependent variable was the added duration of stability plotted in Figure 40.

to kinetic mechanisms (solute drag and a diffusion barrier). Note that this comparison corresponds specifically to the strength or extent of each mechanism incorporated in this work.

5.3.3. *Relating Coarsening Resistance to Solute Segregation Profiles*

As shown in Figures 40 and 41, phase field simulations predict that solute-driven stabilization mechanisms implemented using characteristics of Mn and Zr can effectively increase the coarsening resistance of θ′ precipitates at a temperature of 300 ˚C. Relative to a baseline alloy, these mechanisms were able to increase the duration of stability of the virtual microstructure by as much as 66%. The simulations also predict that no single mechanism can account for the full extent of this stabilization, and in fact the *interaction* between these mechanisms is likely vital in producing the stabilization that has been observed experimentally. This observation is relevant in the effort to design an alloy with even greater thermal stability than ACMZ alloys. When searching for beneficial alloying additions, it may be ineffective to screen for elements that cause the greatest reduction in interfacial energy, or the greatest reduction to Cu diffusivity, or perfectly offset the lattice misfit between phases. Rather, the entire behavior of the solute in the microstructure should be considered, and an alloying element with the optimal combination of properties will likely be more effective than an element screened to have the maximum impact *via* a single mechanism. The present simulation results provide insight on the interaction which occurs between the thermal stabilization mechanisms and how it might relate to experimental observations.

For example, at 300 ˚C, there is synergistic interaction observed between the interfacial energy reduction and solute drag mechanisms. As shown in Figure 40, their stabilization effect in concert is much greater than the sum of their individual stabilization effects. This interaction can be understood by considering the evolution of solute segregation profiles caused by each mechanism.

Figure 41 shows snapshots of θ′ particle evolution and concurrent solute segregation as they occur in three of the simulated alloys, one with the solute drag mechanism activated, one with the interfacial energy reduction mechanisms activated, and one with both (all at 300 °C). As shown in Table 18 and discussed in Section 5.2.3, when a simulation includes a solute drag mechanism, it simply means that the solute was assigned a mobility 0.1% that of Cu. Otherwise, the solute was assigned the same mobility as Cu. The interfacial energy reduction mechanism corresponds to a decrease in $f_{gradient}$ as a function of local solute concentration, defined by Eqs. 28 and 29. If a simulation did not include interfacial energy reduction, the terms in $f_{gradient}$ were independent of solute concentration.

In the simulations shown in Figure 42, the coherent (horizontal) interfaces of the θ′ particle expand outward into the matrix and the semi-coherent (vertical) interfaces retreat, as observed experimentally during overaging [37, 115, 168, 173]. The interaction of the virtual solutes with the moving interfaces leads to different segregation levels at each interface that evolve over time. This evolution is quantified in Figure 43, in the form of proximity histograms derived from the simulation conditions presented in Figure 42.

When a solute drag mechanism is activated in isolation, solute concentration builds primarily at the advancing coherent interface of the particle (upper left plot in Figure 43). As this segregation develops, the outward velocity of the coherent interface is decreased, reducing the coarsening rate and stabilizing the particle morphology. This process is analogous to snow build-up in front of an advancing plow. The result is the classic “bow wave” solute segregation profile which has been observed for solute drag in other alloy systems, both experimentally and in phase field simulations [158, 174]. Based on the present simulations, the effectiveness of solute drag can be enhanced when combined with other mechanisms.

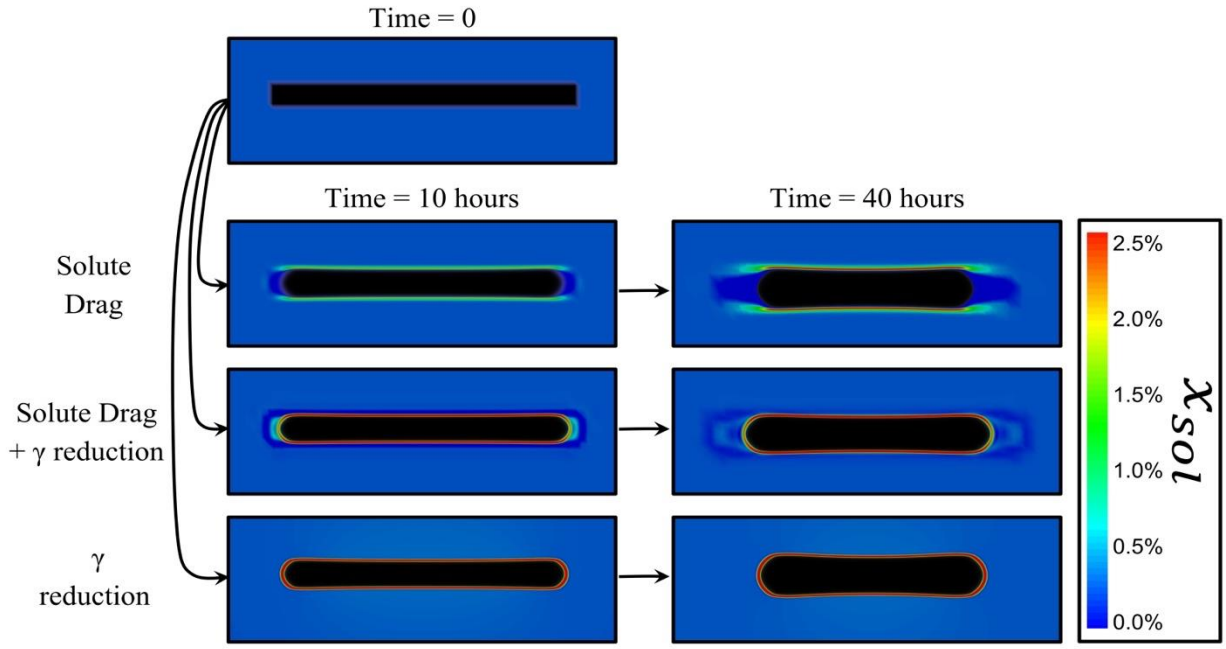

Figure 42. Evolution of solute segregation profiles as a result of solute drag and interfacial energy reduction. The θ′ precipitate is shaded black. The solute drag mechanism results in a classic "bow wave" segregation profile at the coherent interface. When interfacial energy reduction is activated in addition to solute drag, the extent of segregation is increased, particularly to the semi-coherent interface of the θ′ particle.

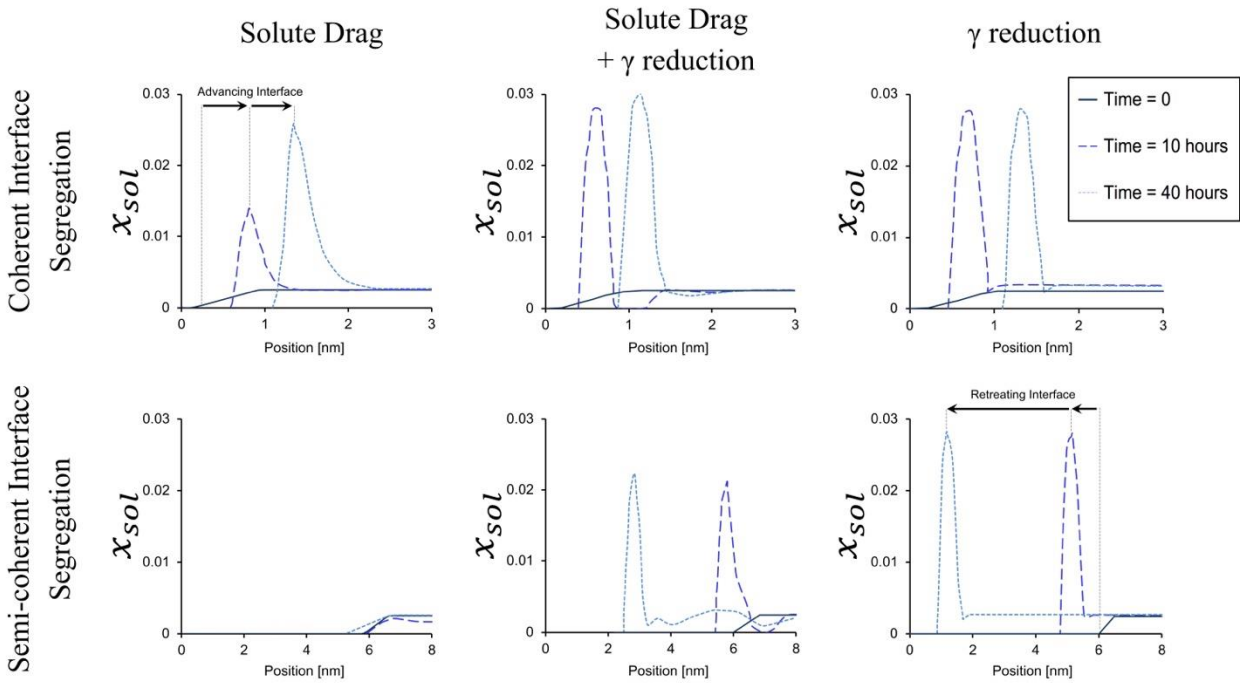

Figure 43. Evolution of the solute distribution that occurs at the coherent and semi-coherent interfaces of one of the larger θ′ particles (shown vertical in Figure 39, rotated 90° here) depending on the active stabilization mechanism(s). The data is shown as a series of proximity histograms, corresponding to the time steps shown in Figure 42. The "position" axis measures distance from an arbitrary location within the initial θ′ particle in a direction orthogonal to the particles coherent interface (top row) or semi-coherent interface (bottom row). Note that solute concentration builds at the advancing coherent interface for the solute drag mechanism, while the retreating semi-coherent interface has no apparent interaction with the solute.

When an interfacial energy reduction mechanism is activated *in addition to* solute drag (center plots in Figure 43), there is a thermodynamic driving force for interfacial segregation, and the extent of segregation is increased. Moreover, the reduced interfacial energy (which is the driving force for coarsening) results in a slower microstructural evolution, allowing more time for the solute to segregate to the (moving) interfaces. Essentially, the slower motion of the interfaces allows the solute more time to equilibrate, resulting in a solute distribution that is closer to what would be expected from equilibrium thermodynamics [175], and affected less by the kinetics of coarsening. This is especially true for the semi-coherent interface which was unaffected by pure solute drag (Figure 42). In the absence of favorable solute segregation to the semi-coherent interface (lower left plot in Figure 43), the coarsening causes the semi-coherent interface to retract from the solute-rich regions, particularly when the solute drag mechanism is active and therefore the kinetics of solute diffusion is slow. Thus, when the solute drag and interfacial energy reduction mechanisms act in concert, solute drag occurs at all interfaces of the θ′ particle and its stabilizing kinetic effects are compounded.

The solute segregation profile predicted for a combination of solute drag and interfacial energy reduction is similar to the segregation profile observed experimentally for Mn in RR350 using APT, as shown in Figure 44a. The corresponding simulated segregation profile is shown in Figure 44b. Given that the combination of interfacial energy reduction and solute drag reproduces both the solute segregation profile and the stabilizing effect that Mn exhibits in ACMZ alloys, these may be the critical characteristics of Mn that make it a beneficial alloying addition.

In contrast to the positive synergy that exists between the solute drag and interfacial energy reduction mechanisms, the present simulations predict that the lattice strain modification mechanism leads to other stabilization mechanisms becoming less effective, even though it

improves the duration of stability when acting in isolation. As mentioned in Section 5.3.2, a combination of all stabilization mechanisms was only 75% as effective as a combination of all the mechanisms *except* for lattice strain modification at 300 °C (Figure 40a). In fact, the detrimental effect of lattice strain modification on the potency of other stabilization mechanisms is so strong that it has an inverse correlation with duration of stability at 300 °C (Figure 41). Again, this interaction can be explained by the solute segregation profile that the lattice strain mechanism causes.

Because the solute element being modeled for the lattice strain mechanism was assigned the atomic radius of Zr, a larger atom than Al, it was rejected by the compressive stress field that exists in the α-Al matrix around the semi-coherent interface of θ′ (in this simulation). When only the lattice strain modification mechanism was activated, it resulted in the solute segregation profile shown in Figure 44d. In this case, solute segregated only to the coherent interface of θ′, especially favoring the outer edge near the junction of the coherent and semi-coherent interfaces. This type of solute segregation profile is observed experimentally for Zr in the ACMZ type alloy RR350 using APT, as shown in Figure 44c. When the lattice strain mechanism was activated in addition to other stabilization mechanisms, it reduced solute segregation to the semi-coherent interface of θ′. In simple energetic terms, the elastic energy resulting from the misfit strain complemented interfacial energy reduction at the coherent interface, but counteracted interfacial energy reduction at the semi-coherent interface. As a result, stabilization mechanisms that would otherwise be acting on the semi-coherent interface were inhibited. These simulations suggest that the solute segregation profile of Zr may be related to its interaction with the stress field around θ′ particles. Zr has a low atomic mobility in Al compared to the other alloying elements discussed here [165], so it likely leads to solute drag effects as well. However, because Zr does not segregate to the semi-coherent

interface of θ′ in ACMZ alloys, its effectiveness in stabilizing θ′ may rely on the co-presence of Mn, as experiments have suggested [14].

Note that the treatment of strain in this phase field simulation is a simplification, as stress fields around θ′ particles change with particle thickness and depend locally on the presence of dislocations [106, 110]. Moreover, the segregation energy and the effects of strain on the energy of segregation are not clearly separable [118]. However, this simplified simulation was able to replicate key features of experimental observations reported here and in prior work [14, 95, 106, 107, 110]. Furthermore, note that Mn and Zr have low diffusivities in Al at 300 °C, approximately 10^{-4} and 10^{-6} that of Cu, respectively [29]. In these simulations, the solute drag mechanism corresponds to a solute mobility 10^{-3} that of Cu. These are, therefore, not direct simulations of Mn or Zr. While the experimental solute segregation profiles shown in Figure 44 are observed after 200 hours at 300 °C, the simulated segregation profiles are achieved in less than 10 hours at 300 °C. The simulations capture the characteristics of Mn and Zr that are determinant in their segregation behavior, but they are not intended to precisely reproduce their kinetics.

As discussed above with reference to Mn, the simulations demonstrate that the interaction between solute drag and interfacial energy reduction greatly influences the solute's segregation behavior and stabilizing effect. If the interfacial energy reduction mechanism is retained, but solute drag mechanism is removed (meaning that the solute's mobility is increased to that of Cu), a distinct segregation profile emerges. Whereas a combination of these two mechanisms leads to non-uniform levels of segregation that increase with time (Figures 42 and 43), the interfacial energy reduction mechanism acting in isolation leads to rapid and uniform solute segregation to all θ′ interfaces.

Note that solute segregation levels resulting from the interfacial energy reduction acting alone

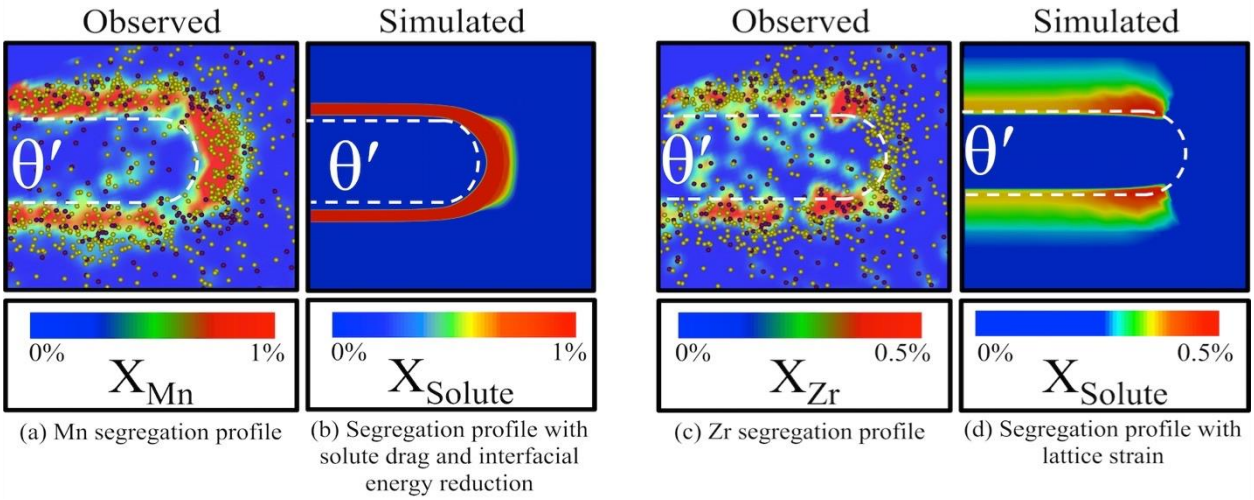

Figure 44. Solute segregation profiles predicted by phase field simulations compared to empirical segregation profiles observed with APT. (a) 2D contour plot of Mn near the θ′ precipitate, calculated from APT measurements with 1x1x30 nm bins. (b) The simulated segregation profile with both the solute drag and interfacial energy mechanisms activated. There is extensive solute segregation to both interfaces, similar to the segregation profile observed for Mn. (c) 2D contour plot of Zr near the θ′ precipitate, calculated from APT measurements with 1x1x30 nm bins. (d) The simulated solute segregation profile with only the lattice strain mechansim activated. The greatest segregation occurs at the junction of the coherent and semi-coherent interfaces, similar to the segregation profile observed for Zr. The purple and gold spheres shown in (a) and (c) are the Mn and Zr atoms, respectively. Note that the observed precipitate is approximately 8 nm thick and the simulated precipitates are approximately 3 nm thick.

reach a maximum value by time = 10 hours and remain constant (bottom images in Figure 42, righthand plots in Figure 43). This suggests that, when solutes can rapidly diffuse and no other mechanisms are present, the solute segregation will quickly saturate, and that subsequent precipitate evolution maintains this level. A similar segregation profile is observed for Ag in Al-Cu-Ag alloys [121]. Ag has characteristics which are consistent with the virtual solute being used to simulate the interfacial energy reduction mechanism. Ag diffuses rapidly in Al [29], and recent work by Shin *et al.* predicted that Ag atoms reduce interfacial energy with almost no misfit in the α-Al matrix [118]. Therefore, the consistency between these experimental and simulated outcomes supports a reasonable level of confidence in the model. Further experimental comparison could be made by performing APT on thermally stabilized α/θ′ microstructures (in alloy families such as ACMZ [4] and Al-Cu-Sc [19]) at multiple timesteps during the coarsening process. If the amount of solute segregation at the coherent or semi-coherent θ′ interface shows time dependence, it would provide additional evidence that solute diffusion kinetics are relevant to the thermal stabilization of these microstructures.

5.3.4. *Temperature Effects*

Results from both prior work and the current work suggest that thermodynamic stabilization mechanisms are more influential in determining the stability of the α/θ′ microstructure at 400 ˚C compared to 300 ˚C [119]. This trend is due to the fact that the thermodynamic terms used in these simulations (as well as thermodynamic stabilization mechanisms in reality [28, 30]) are relatively insensitive to temperature compared to the kinetic terms. For instance, the diffusion barrier mechanism is much less effective at 400 ˚C than 300 ˚C (Figure 40). This is because the diffusivity of Cu increases 80-fold between 300 ˚C and 400 ˚C [29], while the potential reduction in mobility

due to the simulated diffusion barrier mechanism is around 45% for both temperatures. A much more effective diffusion barrier would be required to maintain microstructural stability at 400 ˚C, because the diffusivity of Cu in Al increases exponentially with temperature.

In contrast to a diffusion barrier, solute drag is a relatively "passive" stabilization mechanism. Atoms causing solute drag can remain relatively stationary in the α-Al matrix until the moving interface reaches them. Thus, this mechanism is less affected by the 80-fold increase in Cu's mobility between 300 ˚C and 400 ˚C. Therefore, solute drag provides a better complement to thermodynamic stabilization mechanisms than does a diffusion barrier at 400 ˚C. As shown in Figure 40, the microstructure's duration of stability at 400 ˚C increased in each instance a diffusion barrier mechanism was replaced with a solute drag mechanism.

The primary limitation of solute drag at 400 ˚C is its interaction with the retreating semi-coherent θ′ interface. To interact effectively with the semi-coherent interface, the solute element must have an adequate mobility to reach the interface early in the overaging process. However, the more mobile the solute is, the less effective it will be at inhibiting coarsening kinetics once it reaches the interface. Thus, there is a limit to the optimized, maximum effectiveness of solute drag, which decreases with temperature. This limiting factor highlights the potential importance of multi-solute interaction in ACMZ alloys. Multi-solute interaction is observed in other systems such as Al-Sc-Zr-(Er, Yb) alloys [24, 176]. For these trialuminide precipitate forming alloying elements, solute drag caused by one element inhibits coarsening long enough for slower elements to reach the interface and provide further stability [26]. Since Zr diffuses more slowly than Mn in this system, it is possible than Mn segregation in ACMZ alloys stabilizes θ′ precipitates long enough for Zr to reach the θ′ interface and provide further coarsening resistance.

5.4. Implications for Alloy Design and Future Phase Field Simulation Work

Our results in Section 5.3 indicate that thermodynamic and kinetic effects of solutes at θ′ precipitate interfaces can have a dramatic effect on the coarsening of an Al-Cu microstructure, particularly when they operate together. Section 5.4.1 frames these results in the context of prior work. We then discuss the opportunities and limitations associated with the model in Section 5.4.2.

5.4.1. *Understanding Present Results in Light of Prior Work*

A prior parametric phase field study suggested that modified kinetics might provide the most likely explanation for the microstructural stability observed at 300 ˚C in ACMZ alloys such as RR350 [119]. The current results support a more nuanced conclusion. Although kinetic mechanisms (and particularly solute drag) can be extremely effective in stabilizing the Al-Cu microstructure, they require a thermodynamic "catalyst" (in the form of interfacial energy reduction) in order to exert their stabilizing influence. Prior theoretical analysis of one-dimensional grain boundary motion with solute drag suggests that interfacial velocity is proportional to the product of a driving force term and mobility [177], which is also reflected in the Allen-Cahn formula used here. This is consistent with our finding that the most effective stabilization against coarsening occurs when both kinetic and thermodynamic mechanisms are activated. In the two-dimensional, multi-particle system being studied, the constructive, synergetic interaction of interfacial energy reduction and solute drag may be *greater* than multiplicative. For instance, at 300 ˚C, solute drag acting in isolation has a nearly negligible impact on coarsening resistance, but its stabilizing effect increases by more than 1000% when it is paired with a reduction in interfacial energy, as shown in Figure 40a.

5.4.2. *Model Advancements and Limitations*

The development of a phase field model to evaluate various solute-driven thermal stabilization mechanisms reveals both the opportunities and limitations of such an approach. When performing experimental alloy development, it is often difficult to determine which characteristics of an alloying element are important to achieving certain desirable outcomes in a microstructure. This is because each alloying element has a unique combination of properties which typically are not all known: solubility, free volume, thermodynamic effects, electronegativity, vacancy binding energy, mobility, *etc.* As a result, the solute will have multiple layers of influence in a microstructure without a direct, clear connection to any single property of the element. In terms of testing scientific hypotheses, the phase field approach used here provides a means to alter the solute elemental properties one at a time and observe the effect it has on microstructure. However, there are aspects of the virtual microstructure presented in this work that sacrifice accuracy for utility.

For instance, the limited dimensions of the simulation and the particles themselves do not provide a full representation of experimental Al-Cu microstructures. Rather than producing the most accurate simulation of θ′ morphological evolution, the virtual microstructure utilized was the simplest that could be used to study particle coarsening behavior. The modest length and time scales, in addition, improved the computational efficiency of simulating a ternary alloy system, and made a high-throughput approach feasible. In reality, the processes of coarsening and shape evolution are concurrent and both contribute to the destabilization of the as-aged α/θ′ microstructure [3, 37]. Because the initial condition of the simulation does not fully reflect experimental microstructures (in which θ′ precipitates have increased interparticle spacing and a 3 – 15 times greater diameter [7, 37, 119]), they do not offer *quantitative* information about shape

evolution, even though they recreate the essential features of such evolution. Similarly, using a two-dimensional representation of a three-dimensional system is computationally efficient and has been shown to be accurate enough to aid in metallurgical study [95, 97, 119, 141, 143, 146, 148, 149, 174, 178-181]. However, it removes one degree of anisotropy and further reduces the length of diffusion pathways as compared to a physical microstructure.

In addition, it has been shown experimentally that ternary additions to Al-Cu alloys can have a significant impact on the morphology and distribution of θ′ precipitates under a given aging condition [139, 166, 182]. The simulations presented did not include the nucleation or growth of θ′ precipitates, which allowed for shorter simulations but removed them one step farther from reality. The fidelity of the model was also limited by the nature of phase field theory, which is incapable of capturing atomic-scale mechanisms important to the behavior of θ′ precipitates such as ledge nucleation/growth and solute-vacancy interactions. These limitations highlight the need for multi-scale modeling to accurately describe microstructural evolution. However, the ability of these simulations to replicate the solute segregation profiles and stabilizing effects of solutes in experimental ACMZ alloys suggest that their dimensional and physical limitations are not so great to negate the explanatory power of the phase field approach presented here (although predictive power is less certain). In sum, the outlined phase field approach lends itself most readily to high-throughput modeling to illustrate trends and relationships rather than precisely reproducing how complex microstructures evolve over time.

Now that a method for implementing the four stabilization mechanisms of interest has been established, the logical continuation of this work is to create a more complete picture of trends and relationships between these mechanisms. In the present work, each mechanism was either activated or deactivated *via* the assignment of one value or another to the relevant parameter. In

reality, there are a range of values that each parameter might have, depending on the ternary alloying element. To truly understand how solute characteristics influence segregation profiles and microstructural stability, it will be necessary to sample a larger, more representative value space for each parameter, as well as their combinations. This approach will allow for a more formal sensitivity analysis and point towards the types of alloying elements with the greatest potential for extending the thermal stability of Al-Cu microstructures.

5.5. Conclusions

The objective of this work was to study various physical mechanisms that could account for the improved coarsening resistance of strengthening precipitates observed in Al-Cu-Mn-Zr alloys. This is also likely relevant to effects of Sc in Al-Cu alloys, where Sc is also observed to promote a stable θ′ microstructure [126]. Phase field simulations of coarsening of an Al-Cu microstructure in the presence of a generic ternary alloying element were performed to evaluate the effectiveness of solute-driven thermal stabilization mechanisms including interfacial energy reduction, lattice strain modification, solute drag, and a diffusion barrier. These mechanisms were tested individually and in concert, and the results suggest two primary conclusions:

First, the interaction between individual stabilization mechanisms has a large influence on the coarsening resistance of the simulated Al-Cu microstructure.

- A combination of interfacial energy reduction and solute drag greatly increased the coarsening resistance of θ′ particles at 300 ˚C, as shown in Figure 40. Their combined effectiveness was much greater than the sum of their individual effects.
- A positive misfit strain hindered the ability of an alloying element to interact with and stabilize the semi-coherent interface of θ′. This reduced the effectiveness of other stabilization

mechanisms.

Second, each mechanism leads to a unique solute segregation profile for the ternary element being simulated, demonstrated in Figures 42 and 43. The solute segregation profile can help explain the effect of various elements when introduced to the Al-Cu system.

- Solute drag led to a classic "bow-wave" segregation profile at the coherent interface of θ′, as has been observed experimentally [158, 174].
- When a solute with a positive misfit was introduced to the microstructure, it segregated most heavily to the outer edge of the coherent interface of θ′, avoiding the semi-coherent interface. This type of segregation profile is observed for Zr, as shown in Figure 44.
- A combination of solute drag and interfacial energy reduction led to a continuous segregation profile around θ′ precipitates with an increased concentration at the semi-coherent interface. Mn segregates around θ′ precipitates in this manner, also shown in Figure 44.

This work provides connections between microalloying solute additions and the coarsening resistance of the intrinsically metastable θ′ phase at elevated temperature, particularly providing insights not only into individual mechanisms, but how these mechanisms interact, and how the mechanisms lead to solute-distribution "signatures" near the θ′ particles that may be revealed by atom probe or other techniques. These insights are of interest in alloy systems where solute segregation on heterophase interfaces is critical in determining properties.

5.6. Chapter 5 Appendix

Here, we calculating lattice strain due to solute atom radius mismatch.

From Meyers and Chawla [33]:

$$R_{solute} = R_{Al} \cdot (1 + \epsilon)$$

$$\Delta V_{solute\ atom} = \frac{4}{3} \cdot \pi \cdot R_{Al}^3 \cdot ((1 + \epsilon)^3 - 1\ )$$

Finding volumetric strain of cubic nanometer unit volume:

$$\Delta V = \#\ solute\ atoms \cdot\ \Delta V_{solute\ atom}$$

$$\Delta V\ (per\ nm^3) = x_{sol} \cdot \frac{\#\ Al\ atoms}{nm^3} \cdot\ \Delta V_{solute\ atom}$$

Taking the molar volume of aluminum from [30]:

$$\Delta V = x_{sol} \cdot \frac{6.022 \cdot 10^{23}\ [Al\ atoms]}{9.99 \cdot 10^{-6}[m^3] \cdot \frac{10^{27}[nm^3]}{[m^3]}} \cdot\ \Delta V_{solute\ atom}$$

$$\Delta V = x_{sol} \cdot 60.280 \frac{[Al\ atoms]}{[nm^3]} \cdot\ \Delta V_{solute\ atom}$$

Inserting the $\Delta V_{solute\ atom}$ equation from Myers and Chawla:

$$\Delta V = x_{sol} \cdot 60.280 \frac{[Al\ atoms]}{[nm^3]} \cdot \frac{4}{3} \cdot \pi \cdot R_{Al}^3 \cdot ((1 + \epsilon)^3 - 1\ )$$

Calculating the atomic radius of aluminum based on the lattice constant:

$$\Delta V = x_{sol} \cdot 60.280 \frac{[Al\ atoms]}{[nm^3]} \cdot \frac{4}{3} \cdot \pi \cdot (0.14317[nm])^3\ \cdot ((1 + \epsilon)^3 - 1\ )$$

$$\Delta V = x_{sol} \cdot 0.74100 \cdot ((1 + \epsilon)^3 - 1\ ) \frac{[nm^3]}{[nm^3]}$$

Calculating strain due to solute (assuming strain is isotropic):

$$V = V_o \cdot (1 + \Delta V)$$

$$L = \sqrt[3]{V_o \cdot (1 + \Delta V)}$$

$$L = L_o \cdot \sqrt[3]{(1 + \Delta V)}$$

$$\frac{L}{L_o} = \varepsilon_{xx}, \varepsilon_{yy} + 1 = \sqrt[3]{(1 + \Delta V)}$$

$$\varepsilon_{xx}, \varepsilon_{yy} = \sqrt[3]{(1 + \Delta V)} - 1$$

Inserting expression for ΔV from above:

$$\varepsilon_{xx}, \varepsilon_{yy} = \sqrt[3]{(1 + x_{sol} \cdot 0.74100 \cdot ((1 + \epsilon)^3 - 1\ ))} - 1$$

Chapter 6

The Effect of Si level on the Elevated Temperature microstructural stability of Al-Cu-Mn-Zr Alloys

This chapter is revised based on a drafted journal article with Patrick Shower as lead author:

P. Shower, J. Poplawsky, A. Shyam, The Effect of Si in Al-Cu-Mn-Zr Alloys, (In Review) (2019).

My primary contributions to this paper include (i) objectives and design of study (ii) microstructural characterization and analysis (iii) literature review (iv) most of the writing.

Abstract

Precipitate-strengthened Al-Cu-Mn-Zr alloys demonstrate improved microstructural stability compared to conventional Al-Cu alloys, but their performance varies substantially with Si content. Si is typically considered an impurity in these alloys, but a systematic analysis of Al-Cu-Mn-Zr alloys with a range of Si levels reveals that there is an optimum Si content for achieving high temperature microstructural stability. In this study, a combination of hardness testing and microstructural characterization is used to define the relationship between Si content and temperature dependent microstructural stability in Al-Cu-Mn-Zr alloys. It is shown that a Si level of 0.05 wt % to 0.1 wt % corresponds to a reduced as-aged hardness but a greater amount of hardness retained after thermal exposure to 350 °C for 200 hours. A mechanism is proposed in which optimum Si levels reduce the number density of nucleation sites for precipitates, resulting in larger precipitates that provide reduced as-aged strength but are more coarsening resistant. Work is ongoing, particularly in the area of analyzing Atom Probe Tomography results to identify the specific microstructural features where Si tends to segregate at different stages of heat treatment.

6.1. Introduction

Binary Al-Cu alloys strengthened by the θ′ precipitate phase lose much of their as-aged hardness after being exposed to temperatures greater than 200 °C {, 1992 #27}. With microalloying additions of Mn and Zr, however, these alloys have improved high temperature microstructural stability[14]. As a result, Al-Cu-Mn-Zr alloys (termed *ACMZ* alloys hereafter) retain a greater amount of their as-aged strength after thermal exposure[6]. This has led to ongoing alloy development efforts in the ACMZ system[16]. While ACMZ alloys consistently outperform conventional θ′-strengthened alloys in terms of thermal stability and elevated temperature mechanical properties, it has been observed that within the ACMZ system, there is variation in as-aged hardness and hardness after high temperature thermal exposure. It is desirable to identify the microstructural source of this variation in the high temperature behavior of ACMZ alloys, and any relationship it might have to alloy composition.

The role of Mn and Zr in ACMZ alloys has been studied. These elements diffuse slowly in Al, relative to Cu [29], and have a thermodynamic driving force to segregate to the interfaces of θ′ precipitates[118]. A combination of Atom Probe Tomography, Electron Energy Loss Spectroscopy, hardness testing of model alloys [14], and phase field simulations [183] suggest that when ACMZ alloys are held at elevated temperatures, Mn and Zr tend to segregate to the interfaces of θ′ where they improve the coarsening resistance of the microstructure by a combination of interfacial energy reduction and solute drag. Chemical analysis has identified the critical levels of Mn and Zr necessary to achieve this stabilizing effect. The chemical analysis has also revealed that Si content varies significantly between ACMZ alloys studied up to this point. This observation has prompted further study into the potential effects of Si in ACMZ alloys.

To this point, it is understood that Si is soluble in Al up to 1.65 wt % [1], diffuses more rapidly than Cu [29], and interacts favorably with vacancies[184]. Because of these traits, Si has a significant effect on the as-quenched and as-aged microstructure of Al-Cu alloys [136]. Prior TEM has shown that excess vacancies in solutionized Al and Al-Cu binary alloys tend to form dislocation loops and sometimes helices upon quenching [185-188]. Small Si additions have been shown to favor the formation of dislocation helices in a greater proportion to than dislocation loops[111, 189-191]. Whether in the form of loops or helices, edge-type dislocations act as nucleation sites for GP Zones at room temperature, or θ′ at higher aging temperatures [3, 162]. Furthermore, if a GP II zone contains Si, it is more likely to nucleate a θ′ particle [192]. Other effects have also been tied to Si content, including increased Cu mobility[193, 194] and the formation of Si clusters which can also act as nucleation sites for θ′ [136, 192]. Given the many potential effects of Si in this alloy system, it is unclear how Si interacts with the thermal stabilization mechanisms that operate in ACMZ alloys.

The objective of this study is to assess how Si affects the microstructure and hardness level of ACMZ alloys in the as-aged state and after high temperature thermal exposure. Six ACMZ alloys with varying Si content are analyzed. Microstructural analysis is carried out using Scanning Electron Microscopy (SEM) and Atom Probe Tomography (APT). Vickers hardness testing is used as a simple metric to evaluate how well the alloys retain their as-aged mechanical properties after high temperature thermal exposure. Using these results, we define relationships between these alloys' Si content, as-aged microstructure, microstructural stability, and mechanical properties. We conclude that an optimized Si content in ACMZ alloys leads to greater θ′ precipitate size and inter-particle spacing in the as-aged state, and that such an as-aged microstructure is more

effectively stabilized at elevated temperatures by the solute segregation mechanisms described in prior work [14, 119].

6.2. Materials and Methods

Six ACMZ alloys were studied. Their compositions were found using inductively coupled plasma optical emission spectroscopy and are listed in Table 19.

Each composition was cast in a vacuum arc melter, except for alloy D which was gravity die wedge cast in a sand mold. The alloys underwent solutionizing at 540 °C for 5 hours and aging at 240 °C for 5 hours. Additionally, a sample of each alloy was held at 350 °C for 200 hours after aging. Note that these alloys all had a Cu Content greater than 5.3 weight %, which is the solubility limit of Cu in Al at the solutionizing temperature. Therefore, they are expected to have the same degree of Cu supersaturation in their bulk microstructure upon quenching and form similar volume fractions of θ′ precipitates upon aging. The excess Cu above 5.26 weight % is expected to be captured by grain boundary intermetallics during solutionizing [34].

The microstructure of each alloy was examined in the as-aged state and after the 350 °C thermal exposure. Samples were polished and etched with Keller's reagent (by volume: 95% H_2O, 2.5% HNO_3, 1.5% HCl, 1% HF). Characterization was completed using a Hitachi S4800 Field Emission Gun - Scanning Electron Microscope (FEG-SEM) in secondary electron (SE) mode. HV5 hardness testing was also completed per ASTM E92 at room temperature for each alloy in the as-aged state and after the 350 °C – 200 hour thermal exposure. The average value and standard deviation of 10 hardness measurements were recorded for each alloy in each condition.

Finally, Atom Probe Tomography (APT) was carried out on alloys A, D, and F using the methods described in Section 5.2.4. Several atom probe specimens from each alloy were examined in the as-aged state. The Si content of each precipitate was found by dividing the count of Si atoms within

Table 19. Compositions of the Al-Cu-Mn-Zr-Si alloys used in this study. Fe is an impurity element that is typically partitions to primary intermetallics upon casting [7, 14].

Alloy	**Cu**	**Mn**	**Zr**	**Si**	**Fe**
A	7.49	0.2	0.09	0.03	0.11
B	6.43	0.42	0.12	0.041	0.047
C	7.38	0.42	0.12	0.041	0.049
D	6.403	0.189	0.134	0.049	0.096
E	5.49	0.4	0.18	0.11	0.091
F	7.93	0.44	0.24	0.24	Unknown

the precipitate by the total atom count within the precipitate. The volume of the precipitate was defined by a 10 atomic % Cu isoconcentration surface.

6.3. Results

6.3.1. *The Effects of Si Content on Microstructural Evolution and Hardness Values*

The Vickers hardness of each alloy in the as-aged state and after 200 hour, 350 °C thermal exposure is plotted in Figure 45 as a function of Si content. The as-aged hardness of these ACMZ alloys is minimized at intermediate Si levels (Alloys D and E), while the hardness after the 350 °C thermal exposure is maximized at intermediate Si levels. Thus, alloys with intermediate Si levels retain a larger percentage of their as-aged hardness after thermal exposure. Note that alloys B and C have the same Si content but different Cu contents and show almost identical behavior.

The distinct hardness response of these alloys shown in Figure 45 is reflected in their microstructural evolution. In the as-aged state, those alloys with a greater hardness value are characterized by finely dispersed θ′ precipitates in their bulk microstructures, while those alloys with a lower as-aged hardness exhibit increased θ′ precipitate size and interparticle spacing. Representative micrographs illustrating this trend are shown in Figure 46.

The alloys with low Si levels (Alloys A, B, and C) lost more than 33% of their hardness after thermal exposure. This corresponds to a degradation of their as-aged microstructures during the 350 °C thermal exposure. As shown in Figure 46, the θ′ precipitates in these alloys have coarsened and in some cases transformed into the detrimental θ phase. θ particles have a lower aspect ratio than θ′, making θ an ineffective strengthening phase. Once formed, θ particles tend to coarsen rapidly, decreasing the number density of strengthening particles in their vicinity. This type of

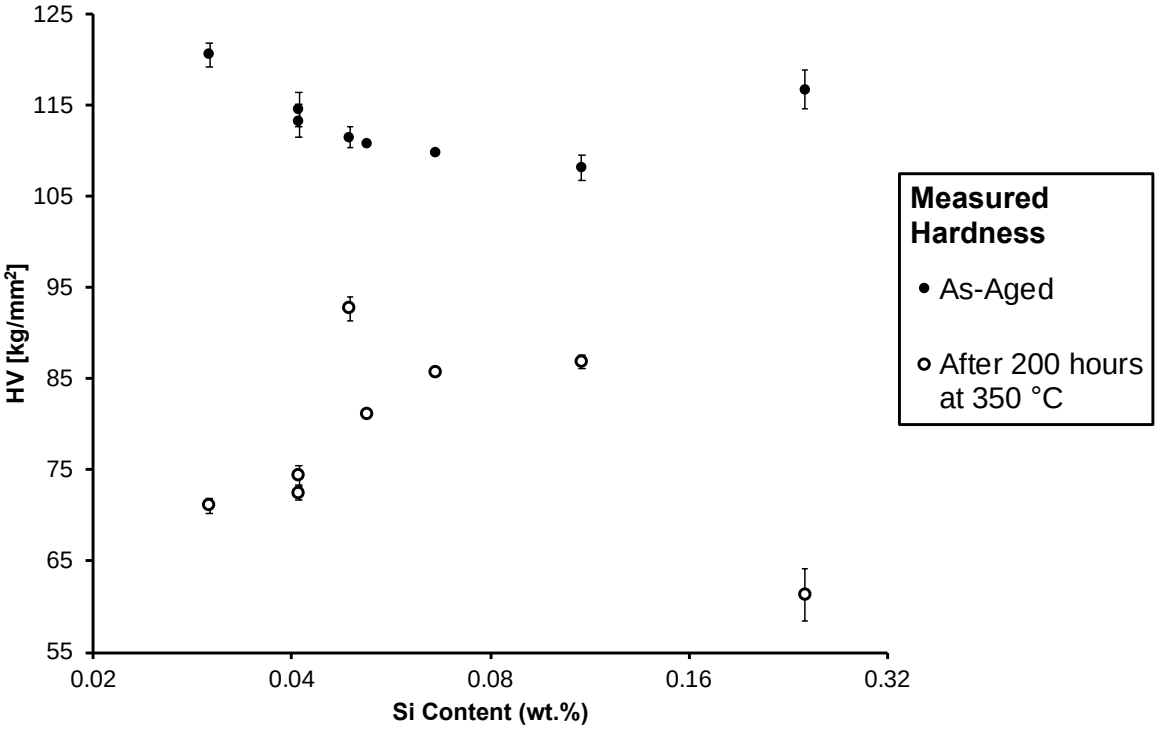

Figure 45. The mean values and standard error of Vickers hardness of each alloy in the as-aged state and after 200 hour, 350 °C exposure are plotted as a function of the alloys' Si content. Note that the x-axis is logarithmic.

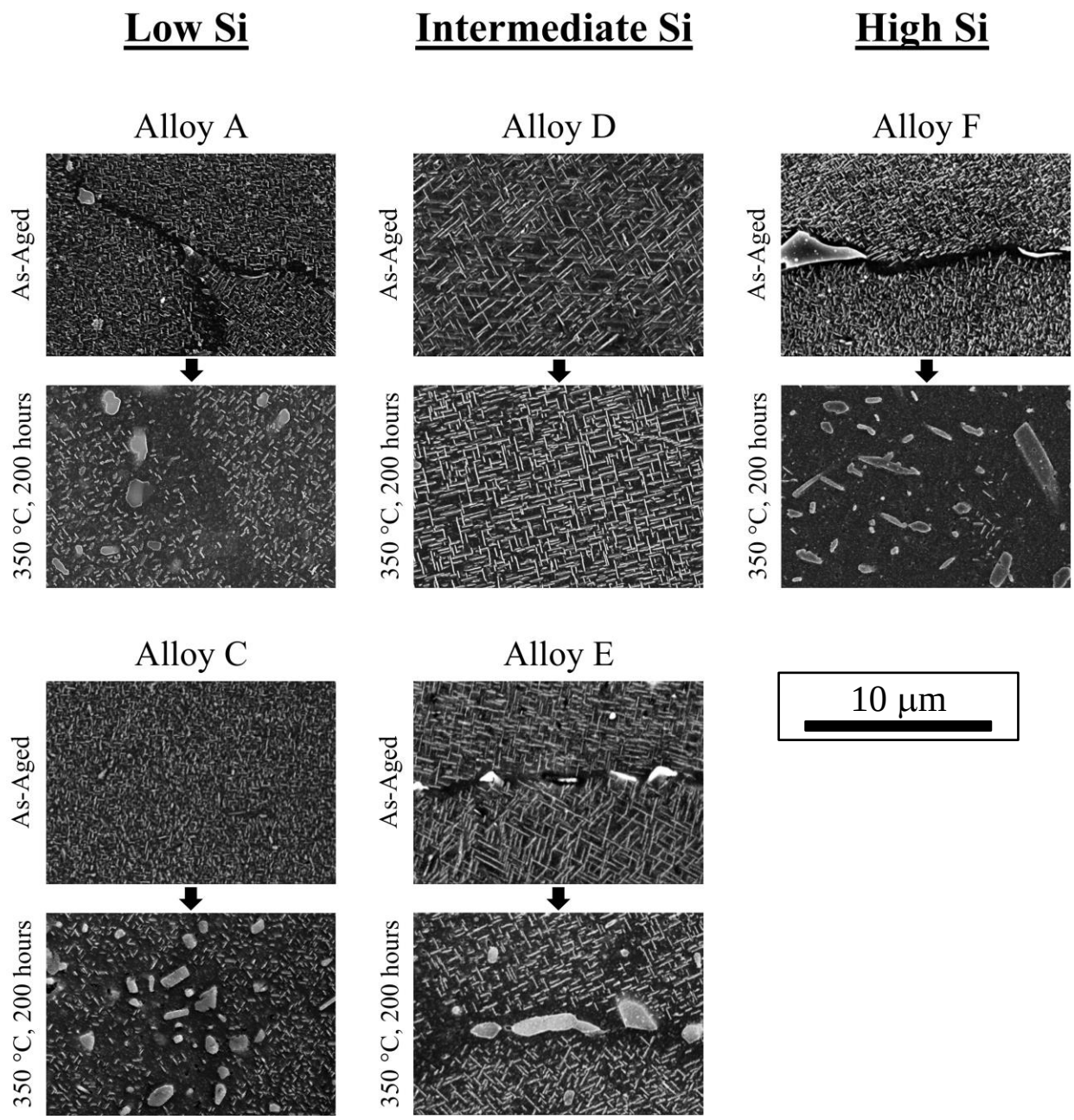

Figure 46. Alloy microstructures after aging and thermal exposure to 300 °C for 200 hours post-aging. The fine precipitate phases observed in all as-aged microstructures are strengthening, disk-shaped θ′, while the coarse, globular intermetallics are the detrimental θ phase. Alloys A and C (with low Si levels) exhibit very fine θ′ particles after aging with partial θ′ to θ transformation after thermal exposure. Alloys D and E (with intermediate Si levels) exhibit larger θ′ particles after aging and show almost no θ′ to θ transformation after thermal exposure. Alloy F (with high a Si level) exhibits fine θ′ particles after aging and extensive θ′ to θ transformation after thermal exposure.

microstructural degradation is also observed in Alloy F, which has a high Si content relative to the other compositions being tested. Alloy F lost 48% of its as-aged strength after the 350 °C thermal exposure.

In contrast, the alloys with intermediate Si levels (Alloys D and E) do not exhibit noticeable microstructural evolution after 200 hours at 350 °C. This is consistent with the thermal stability reported previously for ACMZ alloys [14, 34, 42, 119]. Because alloys D and E retain their as-aged microstructure after this thermal exposure, they largely retain their as-aged properties, losing less than 20% of their as-aged strength.

6.3.2. *Partitioning of Si After Aging*

Alloys A, D, and F fall into the low, intermediate, and high Si level regimes shown in Figure 46, respectively. These alloys are characterized by distinct as-aged microstructures. To evaluate whether Si partitioning or segregation may have influenced the aging process these alloys, the average Si content of θ′ precipitates in each alloy was calculated using APT data and is plotted in Figure 47. Average Mn and Zr content of each precipitate were also plotted.

These results suggest that the amount of Si present in the θ′ precipitates of alloys A and D after aging are similar, while the θ′ precipitates of alloy F are significantly more enriched. Thus, it is possible that Si plays a direct role in the nucleation or growth of θ′ precipitates in alloy F, but not in alloys A or D. Note that the Mn and Zr levels found in each alloy's θ′ precipitates after aging are approximately equal, and so are not likely to account for differentiation between each as-aged microstructure.

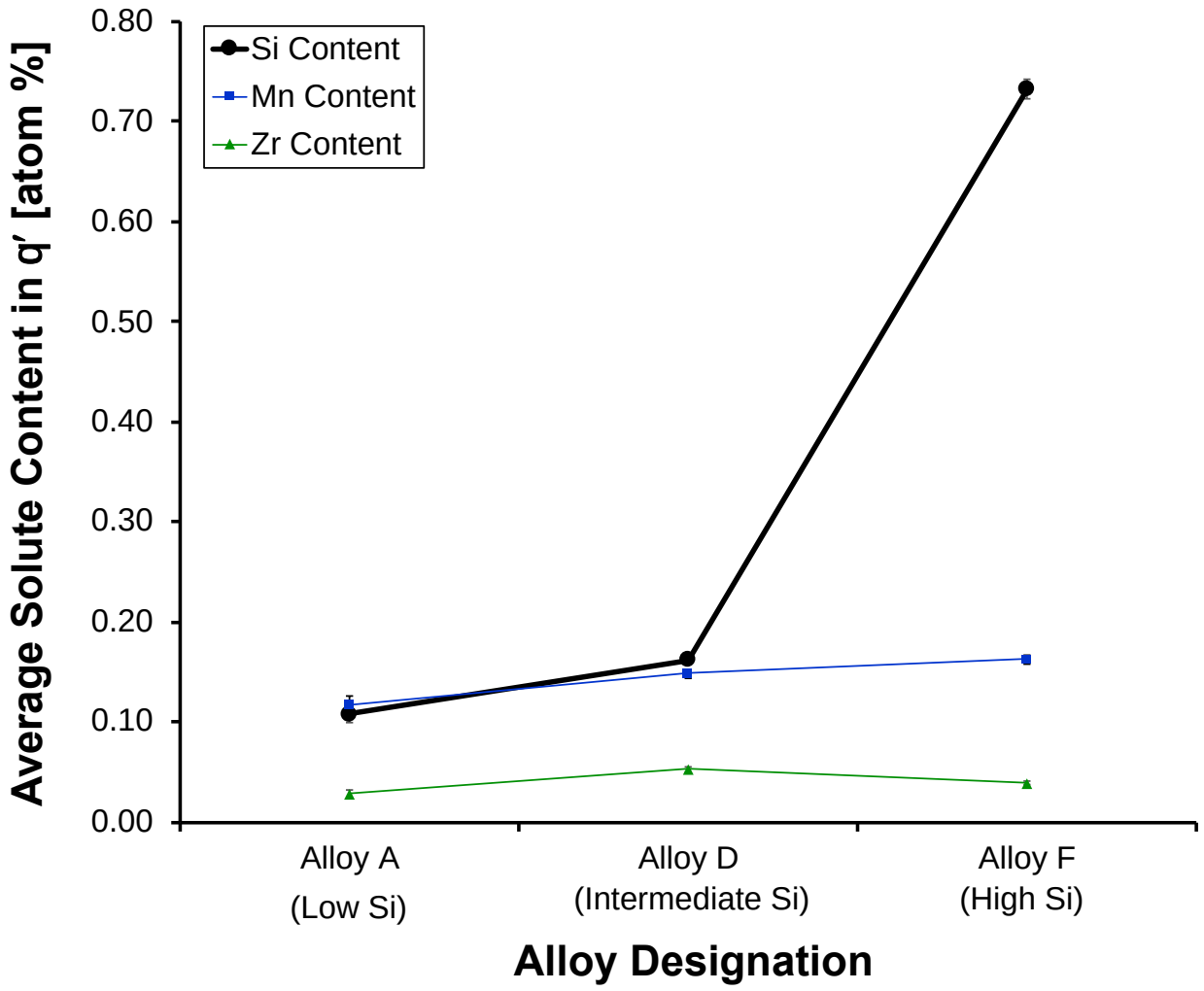

Figure 47. Average content of Si, Mn, and Zr present within θ′ precipitates after aging, by alloy. The increase in total alloy Si content between Alloy A and Alloy D did not greatly alter the level partitioning of Si to θ′ after aging, but Alloy F showed significantly increased Si content within θ′, likely indicating an interaction between Si clusters and the aging θ′ precipitates.

6.4. Discussion

As described in Section 6.3, the intermediate Si levels in Alloys D and E correspond to larger θ′ particles in the as-aged state and increased thermal stability as in terms of microstructural evolution and hardness measurements. In this discussion, we propose that the as-aged morphology of θ′ impacts the coarsening resistance of these particles at elevated temperature (Section 6.4.1), and that producing an optimum as-aged microstructure for coarsening resistance requires an optimum Si content in the ACMZ alloy (Section 6.4.2).

6.4.1. *Relating As-Aged θ′ Morphology to the Microstructural Stability*

The hardness measurements shown in Figure 45 illustrate a counterintuitive trend: ACMZ alloys with a lower as-aged hardness tend to have greater hardness after extended thermal exposure. To explain this trend, we propose a microstructure-properties relationship based on prior research in ACMZ alloys and a theoretical understanding of precipitate coarsening kinetics.

The connection between as-aged microstructure and as-aged hardness is straightforward. Based on the strengthening formula presented by Nie and Muddle [40] for shear-resistant plate shaped particles, the strengthening increment provided by a given volume fraction of θ′ precipitates depends on their diameter and thickness. Larger θ′ particles with a greater diameter and thickness will have a greater "effective interparticle spacing" [195] and therefore provide a lesser contribution to the critical resolved shear stress of the microstructure. As a result, larger θ′ particles (such as those Alloys D and E) are associated with reduced hardness in the as-aged state.

However, larger θ′ particles are also expected to more coarsening resistant. This is critical, because the coarsening of θ′ particles is detrimental for both mechanical properties [6, 7, 14, 34, 42] and the phase stability of θ′ [119, 196]. The two observable characteristics of coarsening θ′ particles

are Ostwald ripening and aspect ratio reduction [37, 113]. Both of these characteristics are affected by precipitate size. The analytical model for aspect ratio evolution of a plate shaped precipitate developed by Shiflet *et al.* [159] predicts that larger precipitates evolve towards their equilibrium aspect ratio at reduced rate compared to smaller precipitates. A larger particle size is also associated with a reduced rate of Ostwald ripening, as captured in the Langer-Schwartz-Wagner coarsening model modified to account for plate shaped precipitates by Boyd and Nicholson [101]:

$$\bar{d}^3 - \bar{d}_o{}^3 = \frac{128}{9} \cdot \frac{D \cdot \gamma_{semicoherent} \cdot c_o \cdot V_m^2}{\pi \cdot R \cdot T} \cdot (t - t_o) \tag{32}$$

where $\bar{d}$ is the mean precipitate diameter, $\bar{d}_o$ is the initial precipitate diameter, D is the diffusivity of Cu in Al, $\gamma_{semicoherent}$ is the excess energy associated with the semi-coherent interface of θ′, c_o is the equilibrium molar concentration of Cu in the matrix, V_m is the molar volume of θ′, R is the universal gas constant, T is absolute temperature, and $(t - t_o)$ is the duration of thermal exposure. Eq. 32 predicts that the mean θ′ particle diameter will increase over time during coarsening, but the kinetics of this process will be reduced if the initial mean diameter is increased. Thus, these analytical coarsening models predict that larger θ′ particles in the as-aged state, as observed for Alloys D and E in Figure 46, have a greater inherent coarsening resistance.

Along with the degree of inherent coarsening resistance, the particle size and spacing of θ′ will likely influence the interaction between θ′ precipitates and solute elements present in the matrix (in this case, Mn and Zr). Prior work suggests that the presence of Mn and Zr to the α/θ′ interface exerts a stabilizing effect on precipitate morphology [14, 118, 119]. In the as-aged state, Mn and Zr are in solid solution in the α-Al matrix. During thermal exposure at 350 °C, Mn and Zr segregate to the α/θ′ interface [14]. Mn and Zr diffuse very slowly in Al. At 350 °C, their diffusivities are

approximately 10^{-4} and 10^{-6} that of Cu in Al, respectively [29]. Therefore, their segregation to the α/θ′ interface is time dependent. If the kinetics of θ′ coarsening are reduced, these solute elements will have more time to reach the α/θ′ interface and exert their stabilizing effect. Larger θ′ particles also have a reduced number density and surface area to volume ratio than finer θ′ precipitates. This reduces the total interfacial area in the microstructure, meaning that more solute is available per unit area of α/θ′ interface. These factors suggest that in addition to the inherent coarsening resistance provided by larger θ′ particles, the interaction between the particles and stabilizing solute elements may be enhanced.

6.4.2. *Relating Si Content to As-Aged θ′ Morphology*

As discussed in Section 6.4.1, an ACMZ microstructure populated by large θ′ particles in the as-aged state is optimal to achieve high temperature coarsening resistance. The mechanisms that control the as-aged morphology of θ′ are less clear. Based on Figures 45 and 46, it appears that adding Si to an ACMZ alloy will increase the size of θ′ precipitates in the as-aged microstructure to a point, beyond which average precipitate size will decrease again. Without additional atomic-scale characterization aided by first principles calculations, it is impossible to determine how Si is interacting with the ACMZ microstructure during aging. Given that limitation, we examine the present results and prior work to propose mechanisms that may be able to explain the dependence of these alloys' as-aged microstructure on Si content.

Generally speaking, increased precipitate size in the as-aged state can be attributed to a reduced nucleation rate and/or an increased growth rate. Although most studies directly examining the effect of Si on the aging response of θ′ precipitates have been focused on Si levels greater than 1 wt. % or alloys that also contain Mg, there are some relevant insights for the aging of ACMZ alloys.

First, that the addition of Si to an Al-Cu alloy certainly has an effect on the types and number density of nucleation sites for θ′. Second, that Si might have additional effects such as increasing the mobility of Cu, increasing the solubility of Cu in Al, and occupying interfacial sites around θ′ particles that could otherwise by occupied by Mn or Zr.

Considering nucleation of θ′ precipitates in binary Al-Cu alloys, the initial formation of θ′ is determined primarily by heat treatment. In the case of low aging temperatures, or natural aging followed by artificial aging, θ′ will nucleate on existing θ′′ particles, which are more coherent with the matrix and have a reduced critical nucleus size. At aging temperatures above the θ′′ solvus (*e.g.* the aging temperature used in this study), θ′ will nucleate directly on edge-type dislocations [3, 91]. These dislocations in the solutionized matrix are a result of excess vacancies present after solutionizing and quenching. The free energy associated with excess vacancies is lowered as these vacancies cluster, and then collapse to form dislocation loops. In some cases, dislocations are able to climb in the as-quenched matrix and form a dislocation helix. These helices are several times larger than individual dislocation loops, and are able to absorb many more excess vacancies in their formation. As a result, the formation of dislocation helices results in a lower number density of defects in the solutionized and quenched microstructure. The prevalence of dislocation loops vs. helices is influential in aging, because these defects provide the nucleation site for precipitates. Whether a binary Al-Cu alloy is naturally or artificially aged, the presence of dislocation loops results in a fine initial distribution of precipitates.

The introduction of Si to an Al-Cu alloy has several potential effects on the defect structures that form after solutionizing and quenching, as observed in prior work. Generally speaking, these effects have been attributed to the favorable binding energy between Si atoms and vacancies in Al. Several studies have examined θ′-strengthened alloys with Si contents of 0.1 – 0.8 wt. % and found

that the presense of Si favors the formation of dislocation helices rather over dislocation loops [111, 190, 191]. The effect of these Si levels on the Al-Cu aging curve is unclear, however, because the alloys had significant Mg levels that also contributed to precipitation hardening. In a study comparing binary Al-2Cu to Al-2Cu-1Si, Mitlin *et al.* concluded that Si atoms (which diffuse more quickly than Cu in Al) rapidly form clusters in the Al matrix, which then act as nucleation sites for θ′ . This results in a decreased size and increased number density of θ′ particles [185-188].

In sum, as Si levels are increased, there is a transition from dislocation-controlled nucleation to solute cluster-controlled nucleation. What occurs at the threshold between these nucleation regimes is unclear. The Alloys A-F that we're studying have Si levels between 0.03 wt. % and 0.24 wt. %, and their microstructures are sensitive to small changes in Si content relative to the intervals in Si content that have been examined previously. Based on prior work, it seems that the present results may be spanning the nucleation regimes from binary Al-Cu to the "catalyzed" aging of θ′ in Al-Cu-Si alloys. This possibility is examined more closely below.

Considering Figures 45 and 46, the ACMZ alloys being analyzed appear to fall into three regimes. Alloys A, B, and C, with the lowest Si content; Alloys D and E with intermediate Si content; and Alloy F with the highest Si content.

We begin by considering the low-Si alloys A, B, and C. These are the most likely to behave like binary Al-Cu alloys during solutionizing, quenching, and aging. In binary Al-Cu alloys, solutionizing and quenching results in excess vacancies that can form dislocation loops or helices as described above. These dislocation structures act as a nucleation site for θ′ particles. A high number density of dislocation loops, in particular, is consistent with the finely distributed θ′ microstructure observed in these alloys as-aged.

Similarly, the finely distributed θ′ observed in Alloy F is consistent with Al-Cu-Si alloys that exhibit extensive heterogenous nucleation on Si clusters that form during quenching, such as the Al-2%Cu-1%Si (wt. %) studied by Mitlin *et al*. [136], a conclusion which is supported by the increased Si content of as-aged θ′ precipitates in Alloys F shown in Figure 47 [136]. It is possible that Alloy F has an adequate Si content to fall within the composition regime that has been most extensively studied: Si compositions greater than 0.2 wt. % generally leading to an accelerated and heightened hardening response during aging. However, the interaction of Si with θ′ in Alloy F could be indicative of other mechanisms acting to destabilize θ′ (such as a competition between Mn segregation and Si segregation), and further analysis will be required. If Si is indeed clustering in the as-quenched microstructure and providing heterogenous nucleation sites as reported previously [192], Alloy F could be considered "macro-alloyed" with Si.

Alloys D and E, however, clearly do not fall into this regime and might be considered to be "micro-alloyed" with Si. These alloys have "intermediate" Si levels relative to the other two regimes, 0.049 wt.% and 0.11 wt. %. These intermediate Si levels are associated with large θ′ precipitates in the as-aged microstructure and improved microstructural stability during 350 °C thermal exposure, relative to the other alloys. The decreased number density of θ′ particles in the as-aged state suggests a decreased number density of preferred nucleation sites. Based on what is known about binary Al-Cu alloys and macro-alloyed Al-Cu-Si alloys, there are two potential explanations that could account for this. One possibility is that θ′ particles in Alloys D and E are nucleating on dislocations, but the number density of dislocations is reduced. This may be because Si atoms bind to excess vacancies and leave fewer available to form defect structures in the as-quenched microstructure [136], or because the presence of Si has led to the formation of dislocation helices with a lower number density than the dislocation loops that would be required to absorb a given

number of excess vacancies [184]. Another possibility is that Si clusters have provided more favorable nucleation sites than dislocations, but the Si levels present are only adequate to form a low number density of clusters. Given that the APT data shown in Figure 47 does not show increased Si content in the θ′ precipitates of Alloy D, it seems more likely that θ′ precipitates are nucleating on dislocations rather than Si clusters. This would lead to the conclusion that the larger average θ′ size and inter-precipitate spacing in the intermediate Si alloys D and E result from a lower number density of quenched-in defects which act as nucleation sites. Again, however, further analysis is required to determine the precise interaction between Si and θ′ in these intermediate Si level alloys.

Note that the microstructural comparisons made in this chapter are aimed at isolating the effects of Si content on the aging of Al-Cu-Mn-Zr alloys. Factors such as aging temperature, quench rate, and deformation are also influential [185-188], in addition to the effects that other alloying elements may have.

6.5. Conclusions

The central conclusion of this work is that maximizing the thermal stability of ACMZ alloys depends on controlling their Si content. Six ACMZ alloys with varying Si levels were examined using SEM and hardness testing to assess their response to aging and a post-aging thermal exposure at a temperature of 350 °C. Two primary observations were made.

First, ACMZ alloys with a greater as-aged hardness tend to exhibit reduced high-temperature microstructural stability.

- Greater as-aged hardness was associated with a decreased size and increased number density of θ′ precipitates in the as-aged microstructure.

- Fine θ′ precipitates with a high number density are expected to have a reduced inherent coarsening resistance, given their reduced interparticle spacing and greater interface curvature.
- Fine θ′ precipitates also have a higher surface area to volume ratio, which means that less Mn and Zr is available per unit area of interface to segregate and stabilize the θ′ particles, as previously described [1]

Second, the Si content of ACMZ alloys influences the morphology of θ′ precipitates in the as-aged microstructure.

- Small amounts of Si (.05 wt % to .1 wt %) are associated with decrease the number density and increase their average size and spacing of θ′ particles after aging.
- Too much Si (greater than .2 wt %) can reverse this effect, resulting in finer, less thermally stable θ′ particles.
- The results suggest that the type and number density of nucleation sites changes depending on the level of Si present in the matrix.

Chapter 7

Conclusions

This work examined the chemistry-processing-structure-property relationships in Al-Cu-Mn-Zr alloys, and found that their impressive high-temperature properties rely on the thermal stability of their microstructure, which in turn relies on a combination of synergistic mechanisms, both kinetic and thermodynamic. These concepts are organized graphically in Figure 47 below.

The work presented in Chapter 2 concluded that the presence of thermally stable θ′ both dramatically improved the mechanical properties of an Al-Cu-Mn-Zr alloy when held and tested at 300 °C, relative to a conventional alloy whose as-aged microstructure was destabilized at 300 °C. The bulk microstructure of the conventional alloy exhibited extensive θ′ → θ transformation at 300 °C, resulting in less effective dislocation barriers and the softening of grains. Chapter 3 concluded that the onset of this detrimental θ′ → θ transformation is related to the coarsening of θ′ particles, and that θ′ particles that were more coarsening resistant will be stabilized against phase transformation. The following chapters explored the mechanisms that may account for the coarsening resistance of θ′ particles in Al-Cu-Mn-Zr alloys.

Chapter 4 evaluated the sensitivity of the α/θ′ microstructure to both thermodynamic and kinetic stabilization *via* a parametric study. It concluded that a combination of thermodynamic and kinetic stabilization could most readily account for the high temperature microstructural stability of Al-Cu-Mn-Zr alloys. Chapter 5 sought to test specific solute-driven mechanisms that may lead to thermodynamic or kinetic stabilization, including interfacial energy reduction, lattice strain modification, solute drag, and a diffusion barrier. Coarsening simulations suggest that a combination of solute drag and interfacial energy reduction act synergistically to provide significant coarsening resistance to θ′ particles, and are associated with solute segregation profiles similar to those observed experimentally in Al-Cu-Mn-Zr alloys. Finally, to determine the role of Si in the composition-processing-microstructure-properties relationship, six Al-Cu-Mn-Zr-Si

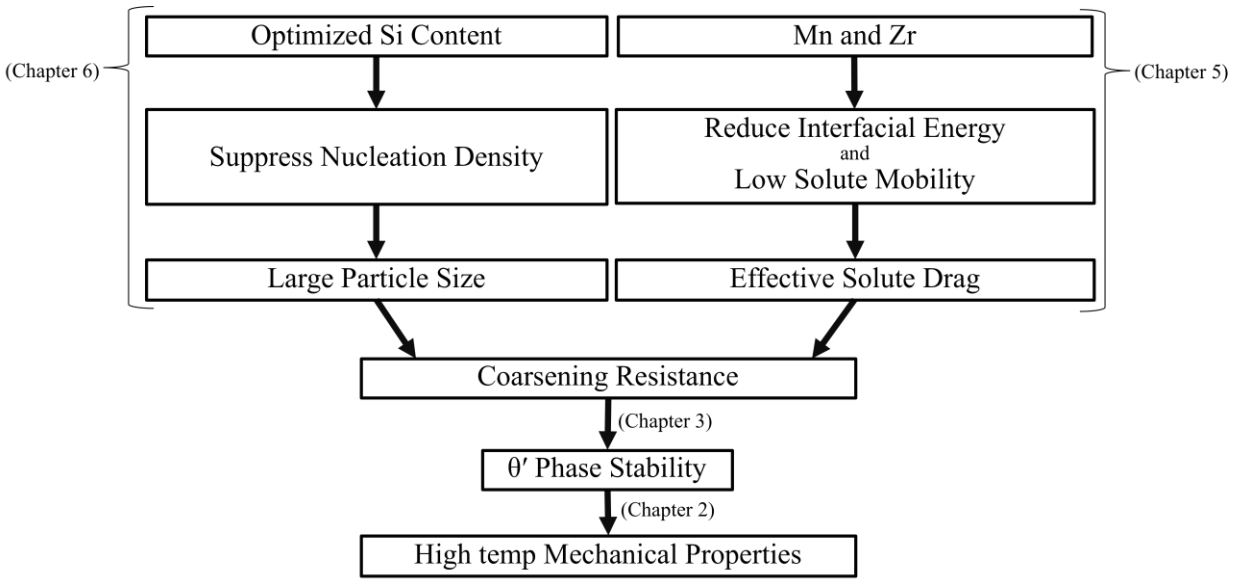

Figure 48. Concept map showing the required factors leading to the favorable high temperature mechanical properties that are characteristic of Al-Cu-Mn-Zr-Si alloys. The chapters in which the key relationships in the concept map are discussed are noted.

alloys with varying Si content were evaluated after aging and after a 200 hour thermal exposure at 350 °C. It was found that alloys with intermediate Si levels between approximately .05 wt % and .1 wt % had larger θ′ particles in the as-aged state, which provided reduced precipitate strengthening after aging but demonstrated greater phase stability and increased hardness levels after thermal exposure.

Chapter 8

Recommendations for Future Work

8.1. Experimental Work

The work presented here rationalizes the stability of microstructure and mechanical properties observed up to 350 °C for Al-Cu-Mn-Zr-Si alloys. Based on the mechanisms that appear to provide thermal stability to these alloys, there are alloy development strategies which may yield θ′-strengthened alloys with optimized properties at either lower or higher temperatures.

To achieve microstructural stability at temperatures greater than 350 °C using the mechanisms described here for Al-Cu-Mn-Zr-Si alloys, the central design requirement is obtaining more effective solute-driven stabilization per unit area of θ′ interface. One strategy is to reduce the total area of θ′ interface in the microstructure. This translates to a lower volume fraction and/or greater average size of θ′ particles. This may be achieved through reducing Cu levels or increasing aging temperature. Another strategy is to provide more Mn and Zr to the θ′ interface. Both Mn and Zr have limited solubility in Al, so increasing the Mn and Zr levels in the alloy will be beneficial only to a certain point. With these slow-diffusing elements, one of the major factors limiting their segregation to the θ′ interface may be their effective diffusion distance. If an Al-Cu-Mn-Zr alloy is held at 300 °C or 350 °C for an extended period of time after aging, perhaps the levels of Mn and Zr segregation to the interfaces of θ′ would increase towards their equilibrium value. And perhaps with greater levels of solute segregation in place, the θ′ precipitates would be able to retain their coarsening resistance to a higher temperature. A final strategy would be introducing additional elements that would behave at 375 °C or 400 °C as Mn and Zr behave at 250 °C to 350 °C. Elements with appropriate diffusivities [14, 118, 183], adequate solubility [165], and favorable interactions with the interfaces of θ′ [1] include Hf and Ti, which occupy Group IV on the periodic

table along with Zr. It may be worthwhile to investigate the microstructural response of alloys containing varying amounts of these additional alloying elements under various conditions.

Conversely, optimizing Al-Cu-Mn-Zr-Si alloys for lower temperature use (250 °C to 300 °C) would likely involve dialing back some of the stabilization mechanisms at play in the baseline alloys. Namely, there is an inverse relationship between as-aged hardness and hardness after thermal exposure to 350 °C for 200 hours. This is because the requirements for maximized thermal stability (larger θ′ precipitates with greater interparticle spacing) are counter to the requirements for high as-aged strength. However, if the required thermal stability is lowered (*i.e.* designing for a service temperature of 250 °C to 300 °C rather than 350 °C), then perhaps a greater as-aged strength could be targeted, leading to reduced but adequate thermal stability. Specifically, this targeting would include decreasing the size and increasing the number density of θ′ particles. As described in Chapter 6, this could be achieved through greater Si content in the alloy. Other possible processing routes to achieve a finer dispersion of precipitates include a decreased aging temperature or pre-aging deformation.

8.2. Theoretical Work

Several phase field simulation capabilities developed in this work could be further applied to better understand and predict the evolution of θ′ and θ particles. Possible investigations include the aging of θ′ particles, the effect of an applied external strain, more detailed analysis on how solutes and evolving precipitates interact, and simulating additional scenarios for θ′ vs θ phase competition.

As discussed in Chapter 5, the aging of Al-Cu-Mn-Zr alloys is influential on their high temperature microstructural stability. In all the simulations reported here, the initial condition included θ′ precipitates that were already formed in the microstructure, with an assigned size, aspect ratio, and

spatial distribution. In reality, the morphology of θ′ particles is determined by aging temperature, the nature and availability of heterogenous nucleation sites, and the presence of alloying elements which interact with growing θ′ precipitates. Given the importance of controlling the morphology of θ′ precipitates in the as-aged microstructure, it would be helpful to understand the relative influences of these factors. The primary challenge in simulating the aging of this system is the anisotropic growth kinetics of θ′ associated with advancing ledges. The capability to simulate this anisotropy was developed and tested over several iterations, but never perfected or used in a substantial study.

The role of strain in microstructural evolution of Al-Cu microstructures is interesting, but relatively unstudied in the current work. The equilibrium aspect ratio of θ′ results from a minimization of strain energy plus interfacial energy. The strain associated with nucleating incoherent θ particles is usually attributed to their large critical nucleus size. Tensor mechanics have been built into all the phase field simulations presented here. It would be relatively straightforward to apply various modes of strain to a virtual microstructure to observe how they affect the competition between θ′ and θ as well as the evolution of individual particles. This may yield information about preferred θ′ orientations under creep conditions, critical θ nucleus size as a function of strain, and the partition of stress between the α-Al matrix and the stiffer intermetallic phases.

In terms of solute-precipitate interaction, a relatively small value space for solute parameters was analyzed here, as described in Chapter 6. There are several research strategies that may offer valuable information on the relationship between solute elements and evolving Al-Cu microstructures. One would be extending the methodology presented in Chapter 6 to evaluate different parameter values for each mechanisms, such as various elemental mobilities, interfacial

energy reductions, and lattice misfits, followed by a formal sensitivity analysis to obtain clearer results about the interaction between different mechanisms. Another approach would be using the available data on elemental mobility [118], as well as misfit and segregation energy [29] to simulate specific solute elements. Important aspects of solute segregation not discussed in this work include the interaction of multiple solutes and solutes with anisotropic effects on the interfacial energy of θ′. Again, simulations capable of modeling these effects were developed as part of the present work but not brought to full fruition in a numerical experiment.

The competition between θ′ and θ phases is fundamental to the high-temperature-capability of Al-Cu-Mn-Zr alloys. Chapter 4 focused specifically on the competition between a single θ′ particle and a θ nucleus which had formed on its semi-coherent interface. In the evolution of an Al-Cu microstructure, many different morphologies and arrangements of the two phases might be present. It would be interesting to investigate the competition between large θ particles observed at the grain boundary and θ′ particles in their vicinity. This may yield information on the formation of precipitate-free zones and how changes to the interfacial energy of θ′ may affect the process. Similarly, one could evaluate how large a standalone θ particle in the matrix would have to be in order to coarsen at the expense of θ′ particles, and track that critical value as a function of modifications to θ′ size, spacing, and interfacial energy.

References

[1] Aluminum and Aluminum Alloys ASM Specialty Handbook, ASM International, Materials Park, OH, 2010.
[2] M. Javidani, D. Larouche, Application of cast Al–Si alloys in internal combustion engine components, International Materials Reviews 59(3) (2014) 132-158.
[3] E. Hornbogen, Hundred years of precipitation hardening, Journal of Light Metals 1(2) (2001) 127-132.
[4] Materials Selection Charts. http://www-materials.eng.cam.ac.uk/mpsite/interactive_charts/default.html, 2002).
[5] C. Johnson, Automotive Engine, 1 ed., Physics and Mechanics, 2003.
[6] S. Roy, L.F. Allard, A. Rodriguez, W.D. Porter, A. Shyam, Comparative Evaluation of Cast Aluminum Alloys for Automotive Cylinder Heads: Part II—Mechanical and Thermal Properties, Metall and Mat Trans A 48(5) (2017) 2543-2562.
[7] S. Roy, L.F. Allard, A. Rodriguez, T.R. Watkins, A. Shyam, Comparative Evaluation of Cast Aluminum Alloys for Automotive Cylinder Heads: Part I—Microstructure Evolution, Metall and Mat Trans A 48(5) (2017) 2529-2542.
[8] H. Gupta, Fundamentals of Internal Combustion Engines, 2 ed., PHI Learning Private Limited, Delhi, 2013.
[9] K. Stalk, Cut Through a DOHC cylinder head. https://en.wikipedia.org/wiki/Cylinder_head#/media/File:DOHC-Zylinderkopf-Schnitt.jpg , 2005).
[10] Q. Xin, 2 - Durability and reliability in diesel engine system design, in: Q. Xin (Ed.), Diesel Engine System Design, Woodhead Publishing2013, pp. 113-202.
[11] H. Yamagata, 2 - The cylinder, in: H. Yamagata (Ed.), The Science and Technology of Materials in Automotive Engines, Woodhead Publishing2005, pp. 10-52.
[12] H. Yamagata, 1 - Engines, in: H. Yamagata (Ed.), The Science and Technology of Materials in Automotive Engines, Woodhead Publishing2005, pp. 1-9.
[13] K.J. Buschow, R.W. Cahn, M.C. Flemings, B. Ilschner, E.J. Kramer, S. Mahajan, Encyclopedia of materials, Science and technology 1 (2001) 11.
[14] A. Shyam, S. Roy, D. Shin, J. Poplawsky, L. Allard, Y. Yamamoto, J. Morris, B. Mazumder, J. Idrobo, A. Rodriguez, T. Watkins, J. Haynes, Elevated temperature microstructural stability in cast AlCuMnZr alloys through solute segregation, In Review (2019).
[15] H. Yamagata, 11 - The turbocharger and the exhaust manifold, in: H. Yamagata (Ed.), The Science and Technology of Materials in Automotive Engines, Woodhead Publishing2005, pp. 248-260.
[16] A. Shyam, J.A. Haynes, G. Black, J. Talamantes, High Performance Cast Aluminum Alloys for Next Generation Passenger Vehicle Engines, Oak Ridge National Lab.(ORNL), Oak Ridge, TN (United States), 2018.
[17] J. Lee, Commercialization of NASA's High Strength Cast Aluminum Alloy for High Temperature Applications, 28th Annual Conference on Composites, Materials & Structures, Cape Canaveral, FL, 2004.
[18] S. Nutt, R. Carpenter, Non-equilibrium phase distribution in an Al-SiC composite, Materials Science and Engineering 75(1-2) (1985) 169-177.
[19] K.M. Shorowordi, T. Laoui, A. Haseeb, J.-P. Celis, L. Froyen, Microstructure and interface characteristics of B4C, SiC and Al2O3 reinforced Al matrix composites: a comparative study, Journal of Materials Processing Technology 142(3) (2003) 738-743.

[20] T. Christman, S. Suresh, Effects of SiC reinforcement and aging treatment on fatigue crack growth in an Al□ SiC composite, Materials Science and Engineering: A 102(2) (1988) 211-216.
[21] S. Nutt, J. Duva, A failure mechanism in Al□ SiC composites, Scripta Metallurgica 20(7) (1986) 1055-1058.
[22] D.N. Seidman, E.A. Marquis, D.C. Dunand, Precipitation strengthening at ambient and elevated temperatures of heat-treatable Al(Sc) alloys, Acta Materialia 50(16) (2002) 4021-4035.
[23] M.A. Kerkove, T.D. Wood, P.G. Sanders, S.L. Kampe, D. Swenson, The diffusion coefficient of scandium in dilute aluminum-scandium alloys, Metall and Mat Trans A 45(9) (2014) 3800-3805.
[24] R.A. Karnesky, D.C. Dunand, D.N. Seidman, Evolution of nanoscale precipitates in Al microalloyed with Sc and Er, Acta Materialia 57(14) (2009) 4022-4031.
[25] K.E. Knipling, R.A. Karnesky, C.P. Lee, D.C. Dunand, D.N. Seidman, Precipitation evolution in Al–0.1Sc, Al–0.1Zr and Al–0.1Sc–0.1Zr (at.%) alloys during isochronal aging, Acta Materialia 58(15) (2010) 5184-5195.
[26] C. Monachon, M.E. Krug, D.N. Seidman, D.C. Dunand, Chemistry and structure of core/double-shell nanoscale precipitates in Al–6.5Li–0.07Sc–0.02Yb (at.%), Acta Materialia 59(9) (2011) 3398-3409.
[27] Y.W. Riddle, T.H. Sanders, A study of coarsening, recrystallization, and morphology of microstructure in Al-Sc-(Zr)-(Mg) alloys, Metall and Mat Trans A 35(1) (2004) 341-350.
[28] J.P. Schaffer, The Science and Design of Engineering Materials, 2 ed., McGraw Hill1999.
[29] Smithells Metals Reference Book, 7 ed., Butterworth-Heinemann, Oxford, 1992.
[30] Porter, Easterling, Phase Transformations in Metals and Alloys, Permagon Press1981.
[31] P. Aloke, Solid-Solid Phase Transformations I. http://nptel.ac.in/courses/113101003/parts/partIV/module1/1.7.html , 2010 (accessed 2 February.2016).
[32] Strengthening Mechanisms of Metals: Part Two, Total Materia Database, 2008.
[33] M.A. Meyers, K.K. Chawla, Mechanical Behavior of Materials, Cambridge University Press2009.
[34] B. Milligan, A. Shyam, C. Hawkins, S. Roy, The effect of microstructural stability on the creep behavior of cast Al-Cu alloys at 300°C, In Review (2019).
[35] E. Rincon, H.F. Lopez, M.M. Cisneros, H. Mancha, Temperature effects on the tensile properties of cast and heat treated aluminum alloy A319, Materials Science and Engineering: A 519(1–2) (2009) 128-140.
[36] H. Sehitoglu, T. Smith, X. Qing, H. Maier, J.A. Allison, Stress-strain response of a cast 319-T6 aluminum under thermomechanical loading, Metall and Mat Trans A 31(1) (2000) 139-151.
[37] P. Merle, F. Fouquet, Coarsening of θ′ plates in al-cu alloys—I. experimental determination of mechanisms, Acta Metallurgica 29(12) (1981) 1919-1927.
[38] Z. Gao, X. Zhang, M.a. Chen, Influence of strain rate on the precipitate microstructure in impacted aluminum alloy, Scripta Materialia 59(9) (2008) 983-986.
[39] C. Laird, H. Aaronson, Mechanisms of formation of θ and dissolution of θ′ precipitates in an Al-4% Cu alloy, Acta Metallurgica 14(2) (1966) 171-185.
[40] J.F. Nie, B.C. Muddle, Microstructural design of high-strength aluminum alloys, Journal of Phase Equilibria 19(6) (1998) 543-551.
[41] V. Kokotin, U. Hecht, Molecular dynamics simulations of Al–Al 2 Cu phase boundaries, Computational Materials Science 86 (2014) 30-37.

[42] P. Shower, S. Roy, C.S. Hawkins, A. Shyam, The effects of microstructural stability on the compressive response of two cast aluminum alloys up to 300°C, Materials Science and Engineering: A 700 (2017) 519-529.
[43] H.R. Erfanian-Naziftoosi, E.J. Rincón, H.F. López, Creep Properties of the As-Cast Al-A319 Alloy: T4 and T7 Heat Treatment Effects, Metall and Mat Trans A 47(8) (2016) 4258-4267.
[44] C.C. Engler-Pinto Jr, H. Sehitoglu, H.J. Maier, T.J. Foglesong, Thermo-mechanical fatigue behavior of cast 319 aluminum alloys, in: L. Rémy, J. Petit (Eds.), European Structural Integrity Society, Elsevier2002, pp. 3-13.
[45] H. Ezatpour, M. Sabzevar, S. Jajjadi, Y. Huang, Investigation of work softening mechanisms and texture in a hot deformed 6061 aluminum alloy at high temperature, Materials Science & Engineering A 606 (2014) 240-247.
[46] D. Feng, X. Zhang, S. Liu, Y. Deng, Constitutive equation and hot deformation behavior of homogenized Al-7.68Zn-2.12Mg-1.98Cu-0.12Zr alloy during compression at elevated temperature, Materials Science & Engineering A 608 (2014) 63-72.
[47] B. Li, Q. Pan, Z. Yin, Characterization of hot deformation behavior of as-homogenized Al–Cu–Li–Sc–Zr alloy using processing maps, Materials Science & Engineering A 614 (2014) 199-206.
[48] S.K. Shaha, F. Czerwinski, W. Kasprzak, J. Friedman, D.L. Chen, Effect of solidification rate and loading mode on deformation behavior of cast Al–Si–Cu–Mg alloy with additions of transition metals, Materials Science and Engineering: A 636 (2015) 361-372.
[49] C. Shi, X. Chen, Effect of vanadium on hot deformation and microstructural evolution of 7150 aluminum alloy, Materials Science & Engineering A 613 (2014) 91-102.
[50] T. Kozmel, M. Vural, S. Tin, EBSD analysis of high strain rate application Al–Cu based alloys, Materials Science and Engineering: A 630 (2015) 99-106.
[51] C. Shi, J. Lai, X. Chen, Microstructural Evolution and Dynamic Softening Mechanisms of Al-Zn-Mg-Cu Alloy during Hot Compressive Deformation, Materials 7(1) (2014) 244.
[52] A.S.T.M. International, ASTM E112-13, Standard Test Methods for Determining Average Grain Size, West Conshohocken, PA, 2013.
[53] A.S.f. Testing, M.C.E.-o.M.T.S.E.o.U. Testing, A. International, Standard Test Methods of Compression Testing of Metallic Materials at Room Temperature, ASTM International2009.
[54] A.S.f. Testing, Materials, Annual Book of ASTM Standards 2007: General products, chemical specialties, and end use products. Section 15, ASTM International2007.
[55] G. Dieter, Mechanical Metallurgy, 3 ed., McGraw Hill Publishing Co.1986.
[56] C.M. Sellars, W.M. Tegart, Relationship between strength and structure in deformation at elevated temperatures, Mem Sci Rev Met 63(9) (1966).
[57] J.J. Jonas, C.M. Sellars, W.J.M. Tegart, Strength and structure under hot-working conditions, Metallurgical Reviews 14(1) (1969) 1-24.
[58] C. Zener, J.H. Hollomon, Effect of Strain Rate Upon Plastic Flow of Steel, Journal of Applied Physics 15(1) (1944) 22-32.
[59] S. Roy, S. Suwas, The influence of temperature and strain rate on the deformation response and microstructural evolution during hot compression of a titanium alloy Ti–6Al–4V–0.1 B, Journal of Alloys and Compounds 548 (2013) 110-125.
[60] D. Shepard, A two-dimensional interpolation function for irregularly-spaced data, Proceedings of the 1968 23rd ACM national conference, ACM, 1968, pp. 517-524.
[61] D. Yaney, W. Nix, Elevated Temperature Deformation Behavior of an Al-8.4 Wt Pct Fe-3.6 Wt Pct Ce Alloy, Metallurgical Transactions A 18A (1987) 893-902.

[62] J. da Costa Teixeira, L. Bourgeois, C.W. Sinclair, C.R. Hutchinson, The effect of shear-resistant, plate-shaped precipitates on the work hardening of Al alloys: Towards a prediction of the strength–elongation correlation, Acta Materialia 57(20) (2009) 6075-6089.
[63] K.G. Russell, M.F. Ashby, Slip in aluminum crystals containing strong, plate-like particles, Acta Metallurgica 18(8) (1970) 891-901.
[64] M. Caillard, J.L. Martin, Some aspects of cross-slip mechanisms in metals and alloys, J. Phys. France 50(18) (1989) 2455-2473.
[65] J. Bonneville, D. Caillard, M. Carrard, J.L. Martin, Rate controlling processes in creep of close packed metals at intermediate and high temperatures, Rev. Phys. Appl. 23(4) (1988) 461-473.
[66] D. Caillard, A model of creep at intermediate temperatures in aluminium, Philosophical Magazine A 51(1) (1985) 157-174.
[67] I. Charit, R.S. Mishra, Low temperature superplasticity in a friction-stir-processed ultrafine grained Al–Zn–Mg–Sc alloy, Acta Materialia 53(15) (2005) 4211-4223.
[68] G.Y. Chin, W. Hosford, W. Backofen, Ductile fracture of aluminum, Transactions of the Metallurgical Society of AIME 230(3) (1964).
[69] R. King, B. Chalmers, Crystal boundaries, Progress in Metal Physics 1 (1949) 127-162.
[70] G. Stechauner, E. Kozeschnik, Self-Diffusion in Grain Boundaries and Dislocation Pipes in Al, Fe, and Ni and Application to AlN Precipitation in Steel, Journal of Materials Engineering and Performance 23(5) (2014) 1576-1579.
[71] R. Raj, M.F. Ashby, On grain boundary sliding and diffusional creep, MT 2(4) (1971) 1113-1127.
[72] R.S. Gates, The role of grain boundary dislocations in grain boundary sliding, Acta Metallurgica 21(7) (1973) 855-864.
[73] R.C. Pond, D.A. Smith, P.W.J. Southerden, On the role of grain boundary dislocations in high temperature creep, Philosophical Magazine A 37(1) (1978) 27-40.
[74] H.J. Frost, M.F. Ashby, Deformation mechanism maps: the plasticity and creep of metals and ceramics, Pergamon Press, University of Michigan, 1982.
[75] J.A. Pask, A.G. Evans, Ceramic Microstructures '86: Role of Interfaces, Springer Science & Business Media2013.
[76] J. May, H.W. Höppel, M. Göken, Strain rate sensitivity of ultrafine-grained aluminium processed by severe plastic deformation, Scripta Materialia 53(2) (2005) 189-194.
[77] I. Martinez, Thermal Effects on Materials, 1 ed., Technical University of Madrid, Madrid, Spain, 2016.
[78] R. Le Hazif, J. Poirer, Cross-slip on {110} planes in aluminum single crystals compressed along 〈100〉 axis, Acta Metallurgica 23(7) (1975) 865-871.
[79] Z.S. Basinski, Thermally activated glide in face-centred cubic metals and its application to the theory of strain hardening, Philosophical Magazine 4(40) (1959) 393-432.
[80] M. Carrard, J.L. Martin, A study of (001) glide in [112] aluminium single crystals, Philosophical Magazine A 56(3) (1987) 391-405.
[81] S. Wang, L.G. Hou, J.R. Luo, J.S. Zhang, L.Z. Zhuang, Characterization of hot workability in AA 7050 aluminum alloy using activation energy and 3-D processing map, Journal of Materials Processing Technology 225 (2015) 110-121.
[82] M. Stoudt, L. Levine, A. Creuziger, J. Hubbard, The fundamental relationships between grain orientation, deformation-induced surface roughness and strain localization in an aluminum alloy, Materials Science and Engineering: A 530 (2011) 107-116.

[83] G. Taylor, Plastic Strain in Metals, Institute of Metals, 1938, pp. 307-324.
[84] A.K. Parimi, P.S. Robi, S.K. Dwivedy, Severe plastic deformation of copper and Al–Cu alloy using multiple channel-die compression, Materials & Design 32(4) (2011) 1948-1956.
[85] H.J. Liu, H.J. Zhang, L. Yu, Effect of welding speed on microstructures and mechanical properties of underwater friction stir welded 2219 aluminum alloy, Materials & Design 32(3) (2011) 1548-1553.
[86] M.J. Roy, D.M. Maijer, L. Dancoine, Constitutive behavior of as-cast A356, Materials Science and Engineering: A 548 (2012) 195-205.
[87] A. Biswas, D. Siegel, D. Seidman, Simultaneous Segregation at Coherent and Semicoherent Heterophase Interfaces, Physical Review Letters 105(076102) (2010) 1-4.
[88] S. Ringer, K. Hono, Microstructural evolution and age hardening in aluminium alloys: atom probe field-ion microscopy and transmission electron microscopy studies, Materials characterization 44(1-2) (2000) 101-131.
[89] H. Liu, I. Papadimitriou, F. Lin, J. LLorca, Precipitation during high temperature aging of Al− Cu alloys: a multiscale analysis based on first principles calculations, Acta Materialia (2019).
[90] C. Laird, H.I. Aaronson, Mechanisms of formation of θ and dissolution of θ′ precipitates in an Al-4% Cu alloy, Acta Metallurgica 14(2) (1966) 171-185.
[91] E. Hornbogen, Discussion of" Application of Heterogeneous Nucleation Theory to Precipitate Nucleation at G-P Zones"(and Authors') Reply, Metall. Trans. A 9(1) (1977) 134-138.
[92] C.S. Kaira, V. De Andrade, S.S. Singh, C. Kantzos, A. Kirubanandham, F. De Carlo, N. Chawla, Probing novel microstructural evolution mechanisms in aluminum alloys using 4D nanoscale characterization, Advanced Materials 29(41) (2017) 1703482.
[93] S. Mohseni, A. Phillion, D. Maijer, Modelling the constitutive behaviour of aluminum alloy B206 in the as-cast and artificially-aged states, Materials Science and Engineering A, 2015.
[94] I.N. Khan, M.J. Starink, J.L. Yan, A model for precipitation kinetics and strengthening in Al–Cu–Mg alloys, Materials Science and Engineering: A 472(1–2) (2008) 66-74.
[95] V. Vaithyanathan, C. Wolverton, L.Q. Chen, Multiscale modeling of θ′ precipitation in Al–Cu binary alloys, Acta Materialia 52(10) (2004) 2973-2987.
[96] P.E. Marth, H.I. Aaronson, G.W. Lorimer, T.L. Bartel, K.C. Russell, Application of heterogeneous nucleation theory to precipitate nucleation at GP zones, Metallurgical Transactions A 7(10) (1976) 1519-1528.
[97] D.Y. Li, L.Q. Chen, Computer simulation of stress-oriented nucleation and growth of θ′ precipitates inAl–Cu alloys, Acta Materialia 46(8) (1998) 2573-2585.
[98] J. Wang, C. Wolverton, S. Müller, Z.-K. Liu, L.-Q. Chen, First-principles growth kinetics and morphological evolution of Cu nanoscale particles in Al, Acta Materialia 53(9) (2005) 2759-2764.
[99] S.C. Weakley-Bollin, W. Donlon, W. Donlon, C. Wolverton, J.E. Allison, J.W. Jones, Modeling the age-hardening behavior of Al-Si-Cu alloys, Metall and Mat Trans A 35(8) (2004) 2407-2418.
[100] K. Kim, A. Roy, M. Gururajan, C. Wolverton, P. Voorhees, First-principles/Phase-field modeling of θ′ precipitation in Al-Cu alloys, Acta Materialia 140 (2017) 344-354.
[101] J.D. Boyd, R.B. Nicholson, The coarsening behaviour of θ″ and θ′ precipitates in two Al-Cu alloys, Acta Metallurgica 19(12) (1971) 1379-1391.
[102] U. Dahmen, K. Westmacott, Ledge structure and the mechanism of θ′ precipitate growth in Al□ Cu, Physica status solidi (a) 80(1) (1983) 249-262.

[103] F. Fouquet, P. Merle, M. Kohen, J. Merlin, P.F. Gobin, Variation du module d'young associee a la precipitation de la phase θ′ dans un alliage Al□Cu 4%, Acta Metallurgica 27(3) (1979) 315-326.
[104] J.M. Pelletier, G. Vigier, J. Merlin, P. Merle, F. Fouquet, R. Borrelly, Precipitation effects on thermopower in Al-Cu alloys, Acta Metallurgica 32(7) (1984) 1069-1078.
[105] S.P. Ringer, W. Yeung, B.C. Muddle, I.J. Polmear, Precipitate stability in Al□Cu□Mg□Ag alloys aged at high temperatures, Acta Metallurgica et Materialia 42(5) (1994) 1715-1725.
[106] S.Y. Hu, M.I. Baskes, M. Stan, L.Q. Chen, Atomistic calculations of interfacial energies, nucleus shape and size of θ′ precipitates in Al–Cu alloys, Acta Materialia 54(18) (2006) 4699-4707.
[107] Y. Ji, B. Ghaffari, M. Li, L.-Q. Chen, Phase-field modeling of θ′ precipitation kinetics in 319 aluminum alloys, Computational Materials Science 151 (2018) 84-94.
[108] G. Purdy, J. Hirth, Transformation defects on θ′ precipitates in Al–Cu alloys, Philosophical magazine letters 86(03) (2006) 147-154.
[109] L. Bourgeois, C. Dwyer, M. Weyland, J.-F. Nie, B.C. Muddle, The magic thicknesses of θ′ precipitates in Sn-microalloyed Al–Cu, Acta Materialia 60(2) (2012) 633-644.
[110] K. Kim, B.-C. Zhou, C. Wolverton, Interfacial stability of θ′/Al in Al-Cu alloys, Scripta Materialia 159 (2019) 99-103.
[111] C.R. Hutchinson, S.P. Ringer, Precipitation processes in Al-Cu-Mg alloys microalloyed with Si, Metall and Mat Trans A 31(11) (2000) 2721-2733.
[112] J.P. Lokker, N.M.v.d. Pers, A.H. Verbruggen, G.C.A.M. Janssen, J.F. Jongste, S. Radelaar, Localized stress near and the thermal expansion of Al2Cu precipitates in an Al thin film matrix, Journal of Applied Physics 87(2) (2000) 682-688.
[113] P. Merle, J. Merlin, Coarsening of θ′ plates in Al-Cu alloys—II. influence of ledge mechanism, Acta Metallurgica 29(12) (1981) 1929-1938.
[114] X.F.B. N. Han, Z.K. Li, Effect of Si on the Microstructure and Mechanical Properties of the Al-4.5%Cu Alloy, Acta Metallurgica Sinica(English letters) 19(6) (2006) 405-410.
[115] R. Sankaran, C. Laird, Kinetics of growth of platelike precipitates, Acta Metallurgica 22(8) (1974) 957-969.
[116] R. Sankaran, C. Laird, Effect of trace additions Cd, In and Sn on the interfacial structure and kinetics of growth of θ′ plates in Al-Cu alloy, Materials Science and Engineering 14(3) (1974) 271-279.
[117] D. Shin, S. Roy, T.R. Watkins, A. Shyam, Lattice mismatch modeling of aluminum alloys, Computational Materials Science 138 (2017) 149-159.
[118] D. Shin, A. Shyam, S. Lee, Y. Yamamoto, J.A. Haynes, Solute segregation at the Al/θ′-Al2Cu interface in Al-Cu alloys, Acta Materialia 141 (2017) 327-340.
[119] P. Shower, J. Morris, D. Shin, B. Radhakrishnan, L. Allard, A. Shyam, Temperature-dependent stability of θ′-Al2Cu precipitates investigated with Phase Field theory and experiments, Materiallia 5 (2019) 100185.
[120] Y. Chen, Z. Zhang, Z. Chen, A. Tsalanidis, M. Weyland, S. Findlay, L.J. Allen, J. Li, N.V. Medhekar, L. Bourgeois, The enhanced theta-prime (θ′) precipitation in an Al-Cu alloy with trace Au additions, Acta Materialia 125 (2017) 340-350.
[121] J.M. Rosalie, L. Bourgeois, Silver segregation to θ′ (Al2Cu)–Al interfaces in Al–Cu–Ag alloys, Acta Materialia 60(17) (2012) 6033-6041.
[122] J. Silcock, T. Heal, H. Hardy, Structural ageing characteristics of binary aluminium-copper alloys, J. Inst. Metals 82 (1954).

[123] C. Liu, S.K. Malladi, Q. Xu, J. Chen, F.D. Tichelaar, X. Zhuge, H.W. Zandbergen, In-situ STEM imaging of growth and phase change of individual CuAlX precipitates in Al alloy, Scientific reports 7 (2017).
[124] G.C. Weatherly, R.B. Nicholson, An electron microscope investigation of the interfacial structure of semi-coherent precipitates, The Philosophical Magazine: A Journal of Theoretical Experimental and Applied Physics 17(148) (1968) 801-831.
[125] C. Wolverton, V. Ozoliņš, Entropically favored ordering: the metallurgy of Al 2 Cu revisited, Physical review letters 86(24) (2001) 5518.
[126] C. Yang, J.Y. Zhang, L.F. Cao, G. Liu, J. Sun, E. Ma, Stabilizing nanoprecipitates in Al-Cu alloys for creep resistance at 300°C, Materials Research Letters 7(1) (2019) 18-25.
[127] J.K. Lee, D. Barnett, H. Aaronson, The elastic strain energy of coherent ellipsoidal precipitates in anisotropic crystalline solids, Metallurgical Transactions A 8(6) (1977) 963-970.
[128] J.D. Eshelby, The determination of the elastic field of an ellipsoidal inclusion, and related problems, Proceedings of the Royal Society of London. Series A. Mathematical and Physical Sciences 241(1226) (1957) 376-396.
[129] M. Kato, T. Fujii, S. Onaka, Elastic strain energies of sphere, plate and needle inclusions, Materials Science and Engineering: A 211(1-2) (1996) 95-103.
[130] S. Qin, H. Fan, T. Mura, The eigenstrain formulation for classical plates, International Journal of Solids and Structures 28(3) (1991) 363-372.
[131] F.R.N. Nabarro, The strains produced by precipitation in alloys, Proc. R. Soc. Lond. A 175(963) (1940) 519-538.
[132] D. Gerlich, E.S. Fisher, The high temperature elastic moduli of aluminum, Journal of Physics and Chemistry of Solids 30(5) (1969) 1197-1205.
[133] F.R. Eshelman, J.F. Smith, Single-crystal elastic constants of Al2Cu, Journal of Applied Physics 49(6) (1978) 3284-3288.
[134] H. Liu, I. Papadimitriou, F. Lin, J. LLorca, Precipitation during high temperature aging of Al− Cu alloys: A multiscale analysis based on first principles calculations, Acta Materialia 167 (2019) 121-135.
[135] J.D. Boyd, R.B. Nicholson, A calorimetric determination of precipitate interfacial energies in two Al□Cu alloys, Acta Metallurgica 19(10) (1971) 1101-1109.
[136] D. Mitlin, J. Morris, V. Radmilovic, Catalyzed Precipitation in Al-Cu-Si, Metall and Mat Trans A 31(11) (2000) 2697-2711.
[137] S.Y. Hu, J. Murray, H. Weiland, Z.K. Liu, L.Q. Chen, Thermodynamic description and growth kinetics of stoichiometric precipitates in the phase-field approach, Calphad 31(2) (2007) 303-312.
[138] M.R. Tonks, D. Gaston, P.C. Millett, D. Andrs, P. Talbot, An object-oriented finite element framework for multiphysics phase field simulations, Computational Materials Science 51(1) (2012) 20-29.
[139] B.A. Chen, G. Liu, R.H. Wang, J.Y. Zhang, L. Jiang, J.J. Song, J. Sun, Effect of interfacial solute segregation on ductile fracture of Al–Cu–Sc alloys, Acta Materialia 61(5) (2013) 1676-1690.
[140] M. Tonks, P. Millett, W. Cai, D. Wolf, Analysis of the elastic strain energy driving force for grain boundary migration using phase field simulation, Scripta Materialia 63(11) (2010) 1049-1052.
[141] M. Tonks, P. Millett, Phase field simulations of elastic deformation-driven grain growth in 2D copper polycrystals, Materials Science and Engineering: A 528(12) (2011) 4086-4091.

[142] R. Sankaran, C. Laird, Interfacial structure of platelike precipitates, The Philosophical Magazine: A Journal of Theoretical Experimental and Applied Physics 29(1) (1974) 179-215.
[143] L.-Q. Chen, Phase-field models for microstructure evolution, Annual review of materials research 32(1) (2002) 113-140.
[144] W.J. Boettinger, J.A. Warren, C. Beckermann, A. Karma, Phase-field simulation of solidification, Annual review of materials research 32(1) (2002) 163-194.
[145] M. Mamivand, M.A. Zaeem, H. El Kadiri, A review on phase field modeling of martensitic phase transformation, Computational Materials Science 77 (2013) 304-311.
[146] I. Steinbach, Phase-field models in materials science, Modelling and simulation in materials science and engineering 17(7) (2009) 073001.
[147] Y. Wang, J. Li, Phase field modeling of defects and deformation, Acta Materialia 58(4) (2010) 1212-1235.
[148] V. Fallah, J. Stolle, N. Ofori-Opoku, S. Esmaeili, N. Provatas, Phase-field crystal modeling of early stage clustering and precipitation in metal alloys, Physical Review B 86(13) (2012) 134112.
[149] V. Fallah, N. Ofori-Opoku, J. Stolle, N. Provatas, S. Esmaeili, Simulation of early-stage clustering in ternary metal alloys using the phase-field crystal method, Acta Materialia 61(10) (2013) 3653-3666.
[150] H. Liu, J. Nie, Phase field simulation of microstructures of Mg and Al alloys, Materials Science and Technology (2017) 1-14.
[151] H. Liu, B. Bellón, J. Llorca, Multiscale modelling of the morphology and spatial distribution of θ′ precipitates in Al-Cu alloys, Acta Materialia 132 (2017) 611-626.
[152] L. Chen, C. Wolverton, V. Vaithyanathan, Z. Liu, Modeling solid-state phase transformations and microstructure evolution, Mrs Bulletin 26(03) (2001) 197-202.
[153] J.W. Cahn, J.E. Hilliard, Free Energy of a Nonuniform System. I. Interfacial Free Energy, The Journal of Chemical Physics 28(2) (1958) 258-267.
[154] A. Artemev, Y. Wang, A.G. Khachaturyan, Three-dimensional phase field model and simulation of martensitic transformation in multilayer systems under applied stresses, Acta Materialia 48(10) (2000) 2503-2518.
[155] D. Schwen, M. Tonks, Developing Phase Field Models. http://mooseframework.org/wiki/PhysicsModules/PhaseField/DevelopingModels, 2016).
[156] Y. Li, G. Purdy, On the growth of Widmanstätten precipitates in an Al–Cu alloy, Acta Materialia 56(3) (2008) 364-368.
[157] G.R. Purdy, Edge-to-edge plane matching as a criterion for interphase boundaries of low energy, Metall and Mat Trans A 37(3) (2006) 857-863.
[158] L.T. Mushongera, M. Fleck, J. Kundin, Y. Wang, H. Emmerich, Effect of Re on directional -coarsening in commercial single crystal Ni-base superalloys: A phase field study, Acta Materialia 93 (2015) 60-72.
[159] G. Shiflet, H. Aaronson, T. Courtney, Kinetics of the approach to equilibrium shape of a disc-shaped precipitate, Scripta Metallurgica 11(8) (1977) 677-680.
[160] S.K. Son, M. Takeda, M. Mitome, Y. Bando, T. Endo, Precipitation behavior of an Al–Cu alloy during isothermal aging at low temperatures, Materials Letters 59(6) (2005) 629-632.
[161] C. Laird, R. Sankaran, The Structure Of Interphase Boundaries In Solids, Journal of Microscopy 116(1) (1979) 123-140.

[162] G. Thomas, M.J. Whelan, Observations of precipitation in thin foils of aluminium +4% copper alloy, The Philosophical Magazine: A Journal of Theoretical Experimental and Applied Physics 6(69) (1961) 1103-1114.
[163] E. Ozbakir, Development of Aluminum Alloys for Diesel-Engine Applications, Department of Mining and Materials Engineering, McGill University, Montreal, Canada, 2008, p. 98.
[164] M.E. van Dalen, R.A. Karnesky, J.R. Cabotaje, D.C. Dunand, D.N. Seidman, Erbium and ytterbium solubilities and diffusivities in aluminum as determined by nanoscale characterization of precipitates, Acta Materialia 57(14) (2009) 4081-4089.
[165] K.E. Knipling, D.C. Dunand, D.N. Seidman, Criteria for developing castable, creep-resistant aluminum-based alloys–A review, Zeitschrift für Metallkunde 97(3) (2006) 246-265.
[166] J. Silcock, H. Flower, Comments on a comparison of early and recent work on the effect of trace additions of Cd, In, or Sn on nucleation and growth of θ′ in Al–Cu alloys, Scripta Materialia 46(5) (2002) 389-394.
[167] J.M. Rosalie, L. Bourgeois, Silver segregation to θ′(Al 2 Cu)–Al interfaces in Al–Cu–Ag alloys, Acta Materialia 60(17) (2012) 6033-6041.
[168] B. Chen, G. Liu, R. Wang, J. Zhang, L. Jiang, J. Song, J. Sun, Effect of interfacial solute segregation on ductile fracture of Al–Cu–Sc alloys, Acta Materialia 61(5) (2013) 1676-1690.
[169] S.S. Batsanov, Van der Waals Radii of Elements, Inorganic Materials 37(9) (2001) 871-885.
[170] M.K. Miller, R.G. Forbes, Atom-probe tomography: the local electrode atom probe, (2014).
[171] D.J. Larson, T.J. Prosa, R.M. Ulfig, B.P. Geiser, T.F. Kelly, Local electrode atom probe tomography, NY: Springer, New York (2013).
[172] J. Lee Rodgers, W.A. Nicewander, Thirteen Ways to Look at the Correlation Coefficient, The American Statistician 42(1) (1988) 59-66.
[173] R. Sankaran, C. Laird, Effect of trace additions Cd, In and Sn on the interfacial structure and kinetics of growth of θ′ plates in Al□ Cu alloy, Materials Science and Engineering 14(3) (1974) 271-279.
[174] L.T. Mushongera, M. Fleck, J. Kundin, F. Querfurth, H. Emmerich, Phase-Field Study of Anisotropic γ′-Coarsening Kinetics in Ni-Base Superalloys with Varying Re and Ru Contents, Advanced Engineering Materials 17(8) (2015) 1149-1157.
[175] M. Yan, R. Cannon, H. Bowen, Space charge, elastic field, and dipole contributions to equilibrium solute segregation at interfaces, Journal of Applied Physics 54(2) (1983) 764-778.
[176] Y. Harada, D. Dunand, Microstructure of Al 3 Sc with ternary rare-earth additions, Intermetallics 17(1) (2009) 17-24.
[177] J.W. Cahn, The impurity-drag effect in grain boundary motion, Acta Metallurgica 10(9) (1962) 789-798.
[178] D.U. Furrer, Application of phase-field modeling to industrial materials and manufacturing processes, Current Opinion in Solid State and Materials Science 15(3) (2011) 134-140.
[179] Y.U. Wang, Y.M. Jin, A.G. Khachaturyan, Phase field microelasticity theory and modeling of elastically and structurally inhomogeneous solid, Journal of Applied Physics 92(3) (2002) 1351-1360.
[180] K. Grönhagen, J. Ågren, Grain-boundary segregation and dynamic solute drag theory—A phase-field approach, Acta Materialia 55(3) (2007) 955-960.
[181] M. Militzer, Phase field modeling of microstructure evolution in steels, Current opinion in solid state and materials science 15(3) (2011) 106-115.

[182] C. Yang, P. Zhang, D. Shao, R.H. Wang, L.F. Cao, J.Y. Zhang, G. Liu, B.A. Chen, J. Sun, The influence of Sc solute partitioning on the microalloying effect and mechanical properties of Al-Cu alloys with minor Sc addition, Acta Materialia 119 (2016) 68-79.
[183] P. Shower, J. Morris, D. Shin, B. Radhakrishnan, J. Poplawsky, A. Shyam, Mechanisms for stabilizing θ′(Al2Cu) precipitates at elevated temperatures investigated with Phase Field modeling, Materialia (2019) 100335.
[184] C. Wolverton, Solute–vacancy binding in aluminum, Acta Materialia 55(17) (2007) 5867-5872.
[185] S. Yoshida, M. Kiritani, Y. Shimomura, Dislocation loops with stacking fault in quenched aluminum, Journal of the Physical Society of Japan 18(2) (1963) 175-183.
[186] C.P. Harper, Effect of alumina particle additions on the aging kinetics of 2014-aluminum matrix composites, NAVAL POSTGRADUATE SCHOOL MONTEREY CA, 1991.
[187] G. Thomas, M.J. Whelan, Helical dislocations in quenched aluminium-4% copper alloys, The Philosophical Magazine: A Journal of Theoretical Experimental and Applied Physics 4(40) (1959) 511-527.
[188] G. Thomas, Quenching defects in binary aluminium alloys, The Philosophical Magazine: A Journal of Theoretical Experimental and Applied Physics 4(47) (1959) 1213-1228.
[189] D. Kent, G.B. Schaffer, J. Drennan, Age hardening of a sintered Al–Cu–Mg–Si–(Sn) alloy, Materials Science and Engineering: A 405(1) (2005) 65-73.
[190] W. Bonfield, P.K. Datta, Precipitation hardening in an Al-Cu-Si-Mg alloy at 130 to 220° C, Journal of Materials Science 11(9) (1976) 1661-1666.
[191] W. Bonfield, P.K. Datta, Zone formation during room temperature ageing of Al-4% Cu-0.8% Si-0.8% Mg, Journal of Materials Science 12(5) (1977) 1050-1052.
[192] A. Biswas, D.J. Siegel, C. Wolverton, D.N. Seidman, Precipitates in Al–Cu alloys revisited: Atom-probe tomographic experiments and first-principles calculations of compositional evolution and interfacial segregation, Acta Materialia 59(15) (2011) 6187-6204.
[193] D. Cao, Y. Liu, X. Su, J. Wang, H. Tu, J. Huang, Diffusion mobilities in the fcc_A1 Cu–Si, Al–Si and Al–Cu–Si alloys, Journal of Alloys and Compounds 551 (2013) 155-163.
[194] D. Zhang, J. Peng, T. Liu, The fast diffusion paths of copper atoms in Al–Cu–Si alloys, Materials Science and Engineering: A 425(1) (2006) 78-82.
[195] J.F. Nie, B.C. Muddle, I.J. Polmear, The effect of precipitate shape and orientation on dispersion strengthening in high strength aluminium alloys, Materials Science Forum, Trans Tech Publ, 1996, pp. 1257-1262.
[196] P. Shower, J. Morris, D. Shin, L. Allard, B. Radhakrishnan, A. Shyam, Onset of θ′ to θ Phase Transformation in Al-Cu alloys (In Review) (2019).

Vita

Patrick Shower graduated from Mason County High School in Kentucky in 2011. He earned a Bachelor of Science degree in Materials Science and Engineering from Georgia Institute of Technology in 2014. His experience as an undergraduate included internships with the Air Force Research Laboratory and Boeing Research and Technology, as well as undergraduate research under Dr. Kenneth Sandhage.

Patrick joined the Bredesen Center for Interdisciplinary Research and Graduate Education in 2014, taking courses at the University of Tennessee, Knoxville and contributing to alloy development research projects under Amit Shyam at Oak Ridge National Laboratory. In 2018 he was an intern at the General Electric Global Research Center, where he will return to begin full time employment after earning his Ph.D. in Energy Science and Engineering.